Design and Fabrication of Hydrogels for Tissue Engineering Applications

Hossein Ravanbakhsh

Department of Mechanical Engineering
McGill University
Montréal, Canada

June 2021

A thesis submitted to McGill University
in partial fulfillment of the requirements for the degree of
Doctor of Philosophy

To my wife, Hengameh,

To my parents, Helen & Ahmad,

To the victims of flight PS752, who will never be forgotten ···

Abstract

Many single-phase hydrogels offer limited cell-material interaction due to their lack of focal adhesion sites. Single-phase hydrogels generally cannot mimic the heterogeneous structure and composition of the extracellular matrix (ECM), resulting in an entirely different cell mechanobiological behavior in three-dimensional (3D) cell culture. Furthermore, single-phase hydrogels may lack sufficient mechanical properties to resemble the stiffness of the target organs. Composite hydrogels, which are made of a mixture of single-phase hydrogel and various additives, can address the above shortcomings. With this aim, the composition of single-phase glycol chitosan (GC) hydrogel was modified by introducing carbon nanotube (CNT) as an additive. The incorporation of CNTs results in a fibrous structure, which mimics many human tissues, such as vocal fold lamina propria. It was hypothesized that CNTs may affect the properties of the hydrogel scaffold and its interaction with the encapsulated cells. Specifically, as CNTs can provide focal adhesion sites for the cells, CNT-loaded hydrogels were postulated to promote cell recruitment and cell migration.

Bioprinting is a prevailing biofabrication method of hydrogel-based tissue constructs. One significant limitation of existing bioprinted tissues is their lack of shelf-availability caused by complications in both fabrication and storage. The conventional techniques of bioprinting hydrogel tissue constructs are not functional for clinical use since the products cannot be stored for on-demand applications. A unique strategy to overcome this problem is to simultaneously fabricate and store cell-laden volumetric tissue constructs through seamlessly combining bioprinting and cryopreservation. This unconventional biofabrication method was termed cryobioprinting.

Porous composite hydrogels were prepared using GC as the matrix, glyoxal as the chemical crosslinker, and CNTs as the additive. Both carboxylic acid-functionalized carbon nanotubes

(COOH-CNTs) and hydroxyl-functionalized carbon nanotubes (OH-CNTs) were used for fabricating composite hydrogels. The homogeneity of CNT dispersion was evaluated using scanning electron microscopy (SEM). Human vocal fold fibroblast (HVFF) cells were cultured and encapsulated in the composite hydrogels with different CNT concentrations to quantify cell viability. Rheological tests were performed to determine the gelation time and the storage modulus as a function of CNT concentration.

Ideally, an injectable hydrogel implant should promote the recruitment of cells from the surrounding native tissue and allow cells to migrate freely as they generate a new ECM network. Carbon nanotube glycol chitosan (CNT-GC) hydrogels were tested to investigate this phenomenon. Chemoattractant-induced cell migration was studied using a modified Boyden Chamber experiment. Migrated cells were counted using flow cytometry. Cell adhesion was inferred from the morphology of the cells via an image segmentation method. The results confirmed that CNTs significantly impact cell-material interaction in hydrogels by enhancing cell adhesion, cell migration, and cell recruitment.

The cryobioprinting performance was investigated by designing, fabricating, and storing cell-laden constructs made of cryoprotective bioinks using a freezing plate with precisely controllable temperature. The in situ freezing process further promoted the printability of cell-laden hydrogel bioinks to achieve freeform structures otherwise difficult to obtain with direct extrusion bioprinting. The effects of bioink components on printability and cell viability were evaluated. The functionality of the method was finally investigated using cell differentiation and chick ex ovo assays. The results demonstrated the feasibility and efficacy of cryobioprinting as a single-step method for concurrent hydrogel-based tissue biofabrication and storage.

The findings in this study showed that low concentrations of CNTs did not cause significant cytotoxicity in hydrogel scaffolds. In such concentrations, CNTs promoted cell migration and cell adhesion, as verified using modified Boyden Chamber experiments. Cryobioprinting, as an approach for enhancing the performance of hydrogels, was found to be an effective technique that synergistically exploits the advantages of bioprinting and cryopreservation methods. It was shown that storable tissue constructs can be fabricated using the cryobioprinting method. Overall, the novel concept presented in this dissertation holds promise for more practical application of hydrogels in tissue engineering (TE).

Résumé

La plupart des hydrogels monophasés ne permet que peu d'interaction cellule-matériau en raison de leur manque de sites d'adhésion focaux. Les hydrogels monophasés ne peuvent généralement pas imiter la structure hétérogène et la composition de la matrice extracellulaire (ECM), ce qui entraîne un comportement mécanobiologique cellulaire entièrement différent dans une culture cellulaire tridimensionnelle (3D). En outre, la rigidité des hydrogels monophasés et autres propriétés mécaniques ne reproduisent pas toujours bien celles des organes cibles. Les hydrogels composites, qui sont constitués d'un mélange d'hydrogel monophasé et de divers additifs, peuvent combler certaines de ces lacunes. Dans ce but, la composition de l'hydrogel de glycol chitosane (GC) monophasé a été modifiée en introduisant des nanotubes de carbone (CNT) comme additif. L'incorporation de NTC se traduit par une structure fibreuse, qui imite les tissus humains. On a émis l'hypothèse que les NTC peuvent affecter les propriétés de l'échafaudage d'hydrogel et son interaction avec les cellules encapsulées. Plus précisément, on a présumé que les hydrogels chargés de CNT favorisent le recrutement et la migration cellulaire.

La bio-impression est une méthode de biofabrication courante des constructions tissulaires à base d'hydrogel. Une limitation importante des tissus bio-imprimés existants est leur manque de disponibilité en stock causé par des complications à la fois dans la fabrication et le stockage. Les techniques conventionnelles de bio-impression de constructions tissulaires d'hydrogel ne sont pas fonctionnelles pour une utilisation clinique car les produits ne peuvent pas être stockés pour des applications sur demande. Une stratégie unique pour surmonter ce problème consiste à fabriquer et à stocker simultanément des constructions de tissus volumétriques chargés de cellules en combinant de manière transparente la bio-impression et la cryoconservation. Cette méthode de biofabrication non conventionnelle a été appelée la

crybioimpression.

Des hydrogels composites poreux ont été préparés en utilisant GC comme matrice, le glyoxal comme agent de réticulation chimique et les CNT comme additif. Des nanotubes de carbone carboxylique (COOH-CNT) et les nanotubes de carbone hydroxyliques (OH-CNT) ont été utilisés pour fabriquer des hydrogels composites. L'homogénéité de la dispersion des CNT ont été évaluées en utilisant la microscopie électronique à balayage (SEM). Des cellules de fibroblastes de cordes vocales humaines (HVFF) ont été cultivées et encapsulées dans les hydrogels composites avec différentes concentrations de CNT pour quantifier la viabilité cellulaire. Des tests rhéologiques ont été réalisés pour déterminer le temps de gélification et le module de stockage en fonction de la concentration en NTC.

Idéalement, un implant d'hydrogel injectable devrait favoriser le recrutement de cellules à partir du tissu natif environnant et permettre aux cellules de se déplacer librement au fur et à mesure qu'elles génèrent un nouveau réseau ECM. Des hydrogels de nanotubes de carbone glycol chitosane (CNT-GC) ont été testés pour étudier ce phénomène. La migration cellulaire induite par chimioattractant a été mesurée en utilisant une chambre Boyden modifiée. Les cellules migrées ont été comptées en utilisant la cytométrie en flux. L'adhésion cellulaire a été déduite de la morphologie des cellules via une méthode de segmentation d'image. Les résultats ont confirmé que les NTC ont un impact significatif sur l'interaction cellule-matériau dans les hydrogels et améliorent les propriétés mécaniques des hydrogels.

Les performances de la cryobioimpression ont été étudiées en concevant, en fabriquant et en stockant des constructions chargées de cellules faites de bioencres cryoprotectrices à l'aide d'une plaque de congélation avec une température contrôlable avec précision. Le processus de congélation in situ a en outre favorisé l'imprimabilité des bioencres d'hydrogel chargées de cellules pour obtenir des structures de forme libre difficiles à obtenir avec la bio-impression par extrusion directe. Les effets des composants sur l'imprimabilité et la viabilité cellulaire ont été évalués. La fonctionnalité de la méthode a finalement été étudiée en utilisant la différenciation cellulaire et des tests ex ovo sur poussin. Les résultats ont démontré la faisabilité et l'efficacité de la cryobiographie en tant que méthode en une seule étape pour la biofabrication et le stockage simultanés de tissus à base d'hydrogel.

Les résultats de cette étude ont montré que de faibles concentrations de NTC n'entraînaient pas de cytotoxicité significative dans les échafaudages d'hydrogel. Dans de telles

concentrations, les NTC ont favorisé la migration cellulaire et l'adhésion cellulaire, comme cela a été vérifié à l'aide d'expériences modifiées sur la chambre de Boyden. La cryobiographie, en tant qu'approche pour améliorer la fonctionnalité des hydrogels, s'est avérée être une technique efficace qui exploite en synergie les avantages des méthodes de bio-impression et de cryoconservation. Il a été montré que les constructions tissulaires stockables peuvent être fabriquées en utilisant la méthode de cryobioprinting. Dans l'ensemble, le nouveau concept présenté dans cette thèse est prometteur pour une application plus pratique des hydrogels en génie tissulaire (TE).

Contributions and Claims of Originality

In this section a list of journal articles and conference proceedings published by the author during his Ph.D. studies is presented in a chronological order.

- **Peer-reviewed journal articles**

  1. **Ravanbakhsh, H.**, Bao, G., Latifi, N., and Mongeau, L., "Carbon Nanotube Composite Hydrogels for Vocal Fold Tissue Engineering: Biocompatibility, Injectability, and Porosity", *Materials Science & Engineering C* 103 (2019) 109861.

     Contributions: This article reports on the first phase of the present dissertation. H. Ravanbakhsh conceived the idea, developed the outline, designed the experiments, conducted biological, mechanical, and physical experiments, analyzed the results, and drafted the manuscript.

  2. **Ravanbakhsh, H.**, Bao, G., and Mongeau, L., "Carbon Nanotubes Promote Cell Migration in Hydrogels", *Scientific Reports* 10 (2020) 1-10.

     Contributions: This article reports on the second phase of the present dissertation. H.Ravanbakhsh performed and analyzed most experiments. H. Ravanbakhh and G. Bao cultured fibroblasts, and designed cell recruitment and cell migration experiments. H.Ravanbakhsh performed flow cytometry, cell adhesion, and stress relaxation experiments, designed the figures, and wrote the manuscript.

  3. Bao, G., Jiang, T., **Ravanbakhsh, H.**, Reyes, A., Ma, Z., Strong, M., Wang, H., Kinsella, J., Li, J., Mongeau, L., "Triggered Micropore-forming Bioprinting of Porous Viscoelastic Hydrogels", *Materials Horizons* 7 (2020) 2336-2347.

Contributions: H. Ravanbakhsh helped in cell viability experiments, image processing, cell motility tests, printing resolution quantification, and rheology.

4. Zhang, X., Hou, C., Dun, B., Wei, R., **Ravanbakhsh, H.**, Li, P., Wang, Z., Wu, Y., Song, X., Zhao, H., and Li, Q., "Fatigue Behavior of Zr-based Metallic Glass Micropillars", *Materials Science & Engineering A* 787 (2020) 139503.

   Contributions: H.Ravanbakhsh contributed in reviewing and post processing the fatigue analysis results, writing and editing the manuscript.

5. **Ravanbakhsh, H.**, Bao, G., Luo, Z., Mongeau, L., Zhang, Y.S, "Composite Inks for Extrusion Printing of Biological and Biomedical Constructs", *ACS Biomaterials Science & Engineering* (2020).

   Contributions: H.Ravanbakhsh, G.Bao, and Z.Luo contributed equally to this work. H. Ravanbakhsh conceived the idea, developed the outline, wrote sections 1 to 3, prepared schematic figures, revised all the sections, and managed the communications between the authors.

6. Tang, G., Chen, L., Lian, L., Li, F., **Ravanbakhsh, H.**, Wang, M., Zhang, Y.S., Huang, C., "Designable Dual-Power Micromotors Fabricated from A Biocompatible Gas-Shearing Strategy at High-Throughput", *Chemical Engineering Journal* 407 (2021) 127187.

   Contributions: H. Ravanbakhsh helped in interpreting the dual-power micromotor results, writing and reviewing the manuscript.

7. Qu, Q., Zhang, J., Chen, X., **Ravanbakhsh, H.**, Tang, G., Xiong, R., Manshian, B., Seonen, S.J., Sauvage, F., Braeckmans, K., De Smedt, S.C., Huang, C., "Triggered Release from Cellulose Microparticles Inspired by Wood Degradation by Fungi", *ACS Sustainable Chemistry & Engineering* 9 (2021) 387−397.

   Contributions: H. Ravanbakhsh contributed in discussing the ROS-mediated delivery results, writing and reviewing the manuscript.

8. **Ravanbakhsh, H.**, Zhang, X., Luo, Z., Maharajan, S., Mirkarimi, H.S., Tang, G., Chávez-Madero, C., Mongeau, L., Zhang, Y.S., "Cryobioprinting for Shelf-ready Tissue Fabrication and Storage", *Matter* (Submitted).

Contributions: This article reports on the last phase of this dissertation. H. Ravanbakhsh, X. Zhang, and Z. Luo contributed equally to this work. H. Ravanbakhsh designed and performed cryopreservation, cell culture, cell viability, printability, and ice crystal formation experiments. H. Ravanbakhsh and H.S. Mirkarimi performed the numerical simulation. H.Ravanbakhsh, X. Zhang, and Z. Luo wrote G-codes and designed the schematic figures. H. Ravanbakhsh prepared the figures and wrote the draft.

9. **Ravanbakhsh, H.**, Karamzadeh, V., Bao, G., Mongeau, L., Juncker, D., Zhang, Y.S, "Emerging Technologies in Multimaterial Bioprinting", *Advanced Materials* (Submitted).

   Contributions: H. Ravanbakhsh, V. Karamzadeh, and G. Bao contributed equally to this work. H. Ravanbakhsh suggested the review topic, prepared the outline, wrote the introduction, extrusion bioprinting technologies, and most of the conclusions sections. H. Ravanbakhsh prepared the original schematic figures, and led the communications between the authors while working remotely.

- **Patents and disclosures**

1. **Ravanbakhsh, H.**, Mohammadi, S., Mongeau, L., Bao, G., Reyes, A., "Novel Method for the Fabrication of Hydrogel Microparticles using Microfluidics" (2020).
2. Bao, G., Mongeau, L., Li, J., Jiang, T., **Ravanbakhsh, H.**, Wang, H., Kinsella, J., "New Strategies for 3D Printing of Highly Porous Chitosan Scaffolds for Soft Tissue Engineering" (2018).

- **Peer-reviewed conference proceedings**

1. **Ravanbakhsh, H.**, Bao, G., and Mongeau, L., "Cell Migration in Carbon Nanotube-Glycol Chitosan Hydrogels for Vocal Fold Tissue Regeneration", TERMIS-AM Conference, Orlando, FL, Dec. 2019.
2. **Ravanbakhsh H.**, Bao, G., and Mongeau, L., "Stress Relaxation in Carbon Nanotube Composite Hydrogels for Vocal Fold Tissue Regeneration", The 13th

International Conference on Advances in Quantitative Laryngology (AQL), Voice & Speech Research, Montreal, Quebec, Canada, June 2019.

3. **Ravanbakhsh, H.**, Bao, G., Latifi, N., and Mongeau, L., "Swelling Behavior of Carbon Nanotube-based Composite Hydrogels Used as Injectable Biomaterial for Vocal Folds", 5th TERMIS World Congress, Kyoto, Japan, Sept. 2018.

4. Bao, G., Jiang, T., **Ravanbakhsh, H.**, Wang, H., Kazarine, A., Liu, H., Kinsella, J.M., and Mongeau, L., "Fabrication of Vocal Fold Scaffolds with Tissue-like Collagen Alignment Using 3D Bioprinting", 5th TERMIS World Congress, Kyoto, Japan, Sept. 2018.

5. **Ravanbakhsh, H.**, Bao, G., Latifi, N., and Mongeau, L., "The Rheological Properties of Carbon Nanotube-based Composite Hydrogels as an Injectable Biomaterial for Vocal Fold Tissue Engineering", 8th World Congress of Biomechanics (WCB 2018), Dublin, Ireland, July 2018.

6. Bao, G., Jiang, T., **Ravanbakhsh, H.**, Wang, H., Kinsella, J.M., and Mongeau, L., "Evaluation of Chitosan-based Hydrogel as a Bioprinting Material for Vocal Fold Tissue Engineering", The Society for Biomaterials Annual Meeting (SFB 2018), Atlanta, USA, Apr. 2018.

7. **Ravanbakhsh, H.**, Latifi, N., and Mongeau, L., "The Effect of Concentration of Carbon Nanotubes (CNTs) on the Viability of Human Vocal Fold Fibroblasts Encapsulated in Composite Chitosan Glycol-CNT Hydrogels", The 33rd Annual Conference of Canadian Biomaterials Society (CBS 2017), Winnipeg, Canada, May 2017.

8. **Ravanbakhsh, H.**, Mohammadi, S., Bao, G., Tang, G., Taheri, F., Reyes, A., and Mongeau, L., "Microfluidic-based Fabrication of Hydrogel Microspheres with a Controllable Size Using an Oil-free Approach", TERMIS World Conference, Maastricht, Netherlands, Nov. 2021 (Submitted).

Acknowledgements

Foremost, I would like to express my deep and sincere gratitude to my Ph.D. supervisor, Prof. Luc Mongeau, who provided me with the opportunity to do research in his laboratory. I am thankful for all the supports you have given me throughout my studies. I would like to highlight your unique and mature mentoring mindset that gave me the flexibility to follow my interests and find my research path. Apart from all the academic guidance and insights, you gave me opportunities to practice leadership and manage junior students, and I am indebted to you for such an invaluable experience.

I would also like to extend my special thanks to Prof. Shrike Zhang at Harvard Medical School, who hosted me in his research laboratory for six months. His passion for research and constant availability for consultation kept me motivated during the last two years of our collaboration. Working with him, I learned numerous skills in research and time management. I declare that all the experiments related to the cryobioprinting project were conducted in Prof. Shrike Zhang's research lab. The related manuscript is under consideration in *Matter* at the time of writing this dissertation. I also had the great pleasure of collaborating with Prof. David Juncker and benefiting from his valuable comments on our review paper, which is under consideration in *Advanced Materials*.

I value the super-friendly environment that I was surrounded with during the last five years. Special thanks to Guangyu Bao, whose company made the Ph.D. journey an enjoyable period of my life. Working with him has always been one of the most rewarding and delightful experiences I have ever had. I declare that the scanning electron microscopy and biodegradation experiments were conducted with the direct help of Guangyu Bao. I am grateful to my other labmates at McGill, including Huijie Wang, Neda Latifi, Zhengdong Lei, Mostafa Najafiyazdi, Rayane Ait Oubahou, Mehdi Shamshiri, Sepideh Mohammadi,

Sareh Taheri, Alicia Reyes, Qiman Gao, Christina Chen, Marius Muller, Haoqing Liu, Pooya Saberi, Anna Henley, Hana Mirvakili, Alda Profka, Zixin He, Mitchell Strong, and Abigail Vikstrom. I am also thankful for my labmates at Harvard, including Guosheng Tang, Zeyu Luo, Xiang Zhang, Wanlu Li, and Sushila Maharjan. I declare that the cell differentiation and angiogenesis experiments were conducted by Zeyu Luo at Harvard Medical School.

This research would not have been possible without the generous support of various funding agencies, including the National Institutes of Health (NIH), Natural Sciences and Engineering Research Council (NSERC), Fonds de recherche du Québec - Nature et technologies (FRQNT), Mitacs, McGill's Graduate and Postdoctoral Studies (GPS), McGill's Faculty of Engineering, and Centre interdisciplinaire de recherche en musique, médias et technologie (CIRMMT). The content is solely the responsibility of the authors and does not necessarily represent the official views of the National Institutes of Health.

Scanning electron microscopy and transmission electron microscopy images were obtained in the McGill University Facility for Electron Microscopy Research. The flow cytometry work was performed at the Flow Cytometry Core Facility and single-cell analysis at the Life Science Complex at McGill University, supported by funding from the Canadian Foundation for Innovation. Confocal images were collected and processed in the McGill University Life Sciences Complex Advanced BioImaging Facility (ABIF).

My deepest appreciation goes to my family. Hats off to my wife, Hengameh, who not only emotionally supported me but also gave scientific feedback on my works. I feel blessed to have such a great person in my life. I do not even have the words to thank you for all the sacrifices. Thanks to my parents, Helen and Ahmad, and my sister, Hajar, who remotely supported me and motivated me to progress in my studies. Lastly, I thank the "Lunch with Eshghi" group members, Mohsen, Amin, and Alireza, who made my lunches memorable but delayed my graduation for at least one semester!

The contents of this dissertation are either under consideration for publication or have been previously published in scientific journals. In the latter case, where the sections are verbatim of the author's publications, quotation marks are used.

Abbreviations

2D two-dimensional

3D three-dimensional

4D four-dimensional

AI artificial intelligence

BSA bovine serum albumin

BV blood vessel

CAM chorioallantoic membrane

CLSM confocal laser scanning microscopy

CNC cellulose nanocrystal

CNF cellulose nanofiber

CNT carbon nanotube

CNT-GC carbon nanotube glycol chitosan

COOH-CNTs carboxylic acid-functionalized carbon nanotubes

CPA cryoprotective agent

DMEM Dulbecco's Modified Eagle Medium

DMSO dimethylsulfoxide

DPBS Dulbecco's phosphate-buffered saline

ECM extracellular matrix

ER extensibility ratio

FBS fetal bovine serum

FD fractal dimension

FSC-A forward scattered area

GA-1000 gentamicin sulfate-amphotericin

GC glycol chitosan

GelMA gelatin methacryloyl

hEGF human epidermal growth factor

hMSCs human mesenchymal stem cells

HUVECs human umbilical vein endothelial cells

HVFF human vocal fold fibroblast

ID inner diameter

IGF-1 insulin-like growth factor 1

LIFT laser-induced forward transfer

MSC mesenchymal stem cell

MWCNTs multi-walled carbon nanotubes

OD outer diameter

OH-CNTs hydroxyl-functionalized carbon nanotubes

PBS phosphate-buffered saline

RT room temperature

SEM scanning electron microscopy

SMCs smooth muscle cells

SSC-A side scattered area

SWCNTs single-walled carbon nanotubes

TE tissue engineering

TEM transmission electron microscopy

trypsin-EDTA trypsin-ethylenediaminetetraacetic acid

UV ultraviolet

VEGF vascular endothelial growth factor

Contents

List of Figures

List of Tables

CHAPTER 1

Introduction

This chapter begins with a description of the thesis organization and the chapters arrangement. Then, the problem of interest is stated, and the previous relevant studies are reviewed. The current issues that hinders the application of hydrogels in tissue engineering (TE) is discussed, and the rationale for conducting this project to address the stated issues is highlighted. Later, the approach used to tackle the problem is identified and the objectives of the thesis are articulated. The sentences in quotations are verbatim of the author's publications (references [1–3]).

1.1 Thesis organization

The present thesis consists of five chapters, generally including introduction, methods, results and discussion, and conclusion. Chapter 1 starts with articulating the rational for studying the problem of interest, following a comprehensive overview on the available literature. The challenges in the field of biofabrication and TE are stated, and the proposed approaches to overcome those obstacles are explained. The literature survey section is divided into four major subsections. Firstly, composite hydrogels, their characteristics, and their importance for resembling the heterogeneous structure of the human native tissue are discussed by reviewing previous studies. The most common additives used for TE applications are then classified and discussed. Specifically, recent works on the interaction between living cells and carbon

nanotube (CNT)-based composite hydrogels are summarized. The last part of the literature survey provides an overview on the current three-dimensional (3D) bioprinting methods. Also, recent studies on the cryopreservative materials were discussed to establish the foundation for presenting the cryobioprinting method. Finally, the scope of the project is clarified by elaborating the thesis specific aims.

Chapter 2 mainly focuses on the experimental and numerical methods used throughout the thesis. The experimental part is divided into non-biological and biological methods depending on whether living cells were involved in the experiment. The non-biological experiments include scanning electron microscopy (SEM), transmission electron microscopy (TEM), hydrogel synthesis, rheometry and mechanical characterization, swelling tests, biodegradation assays, pore size measurement, and ice crystal imaging, while the biological experiments consist of cell culture, viability, adhesion, migration, differentiation, angiogenesis, chick chorioallantoic membrane (CAM) assay, immunostaining, and histology. The relevant details pertaining to heat transfer simulation and image processing methods are also expanded in this chapter.

In chapter 3, the results related to CNT composite hydrogels, their mechanical behaviour, physical characteristics, and biological interactions with living cells are presented. Initially, the physical characteristics of CNTs alone are studied and the methods to homogeneously disperse them in hydrogel is discussed. It is demonstrated that the incorporation of CNTs in low and medium concentrations does not significantly reduce cell viability, while the mechanical properties, gelation time, and pore size are enhanced. Furthermore, the effect of adding CNTs on promoting cell migration through introducing focal adhesion sites for the cells are elaborated.

Cryobioprinting results and the related discussions are presented in Chapter 4. Therein, cell viability results that were used for optimizing the cryoprotective bioinks are discussed. The capability of cryobioprinting method in fabricating free-standing and relatively complex tissue constructs are proven. Also, the experimental results are verified by heat transfer results drawn from COMSOL Multiphysics software. The feasibility and efficacy of the cryobioprinting method are further demonstrated through mesenchymal stem cell (MSC) differentiation into adipocytes, chondrocytes, or osteoblasts after being cryobioprinted and cryopreserved for certain periods of time. Also, the functionality of cryobioprinted human

umbilical vein endothelial cells (HUVECs) were assessed using angiogenesis experiments.

The last chapter is dedicated to summarizing the main conclusions and highlighting the outcomes of the thesis. The contributions to the knowledge in the field of biofabrication and TE is discussed, and a comprehensive discussion on the perspective and the future direction of the field of bioprinting is presented.

1.2 Problem

Hydrogels are a class of crosslinked polymeric materials with diverse mechanical and biological characteristics. Depending on the intrinsic properties of the primary monomers and the crosslinking mechanism of hydrogels, an extended range of mechanical properties, encompassing from soft (elastic modulus: $1 \sim 100$ pa) [4] to stiff (elastic modulus: 30 MPa) [5], may be achieved. Hydrogels' pore size falls in the range of nanometers to micrometers, making them a suitable option for creating hierarchically porous constructs [6, 7]. The physical response of hydrogels to environmental stimuli, such as temperature, moisture, and pH, is another important characteristic that has been used in designing shape-changing hydrogel constructs [8]. The 3D network of the hydrogels as well as their hydrophilicity and high water content (over 92%) make them an appropriate substrate for 3D cell culture [9]. As a result, numerous biomedical applications, such as TE, tissue model engineering, regenerative medicine, drug screening, and organoid culture, have been recently emerged for hydrogel-based systems [10–12] (Fig. 1.1). In such applications, the mechanobiology of the cells is highly affected based upon what hydrogel is used as the culture scaffold.

Different hydrogels, including natural and synthetic, have been so far developed for TE applications. Alginate, gelatin, chitosan, hyaluronic acid, and collagen are among the best-known natural hydrogels. Some of these hydrogels are suitable for cell culture in their original form, while others may need to be chemically functionalized with different moieties to achieve the desired characteristics. For example, gelatin is commonly functionalized with methacrylate groups to make gelatin methacryloyl (GelMA), a photo-crosslinkable hydrogel with superior rheological properties [14]. Another example of modified hydrogels is glycol chitosan (GC), which is a water-soluble polymer. When GC is crosslinked with glyoxal, an injectable hydrogel precursor with relatively controllable gelation kinetics is achieved.

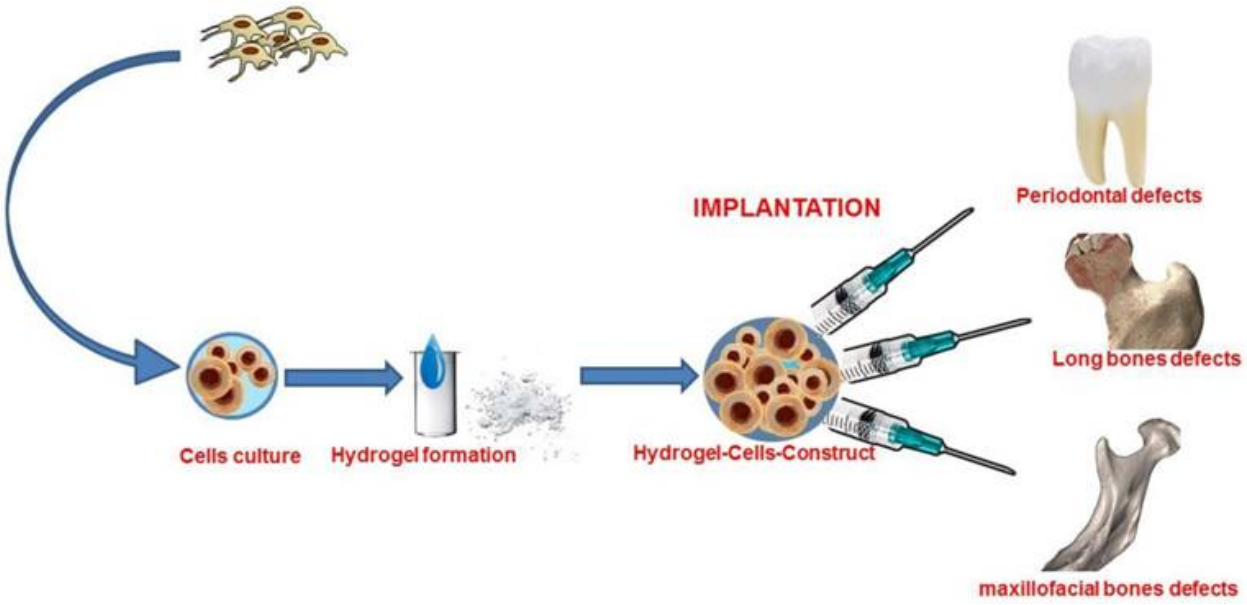

Fig. 1.1. Hydrogel implants for different TE applications. (Adapted from ref [13] under the terms of the CC BY-NC 4.0 license.)

Although this chemical modification improves some characteristics of chitosan hydrogels, it may introduce other challenges and even exacerbate other characteristics of the hydrogel. For example, the pore size in the resulting GC hydrogel is in the order of nanometers, which can impede cell motility and migration. In the first phase of this research, we investigate the methods of enhancing the properties of GC by exploiting additives, such as CNT.

Cell migration and cell adhesion are critical factors in TE. In general, when the hydrogel provides a substrate for the cells to adhere to, the cells' motility through mechanotaxis will increase, which results in promoted cell migration and cell recruitment in the hydrogel implant. A faster cell migration causes the implant to integrate faster with the native tissue and also leads to regeneration of the new engineered tissue. Building on such a premise, using additives, such as CNT to enhance the properties of hydrogels can potentially affect cell adhesion, cell migration, and cell recruitment within the hydrogel. Using mathematical methods to quantify cell migration and cell adhesion is a useful approach for investigating cell-material interaction [15, 16]. Developing a methodology to quantitatively compare these parameters is another problem that is tackled in the present thesis.

Apart from designing the hydrogel constituents and their effect on cell mechanobiology, the challenges in the methods of fabrication are also of paramount importance. 3D bioprinting is one of the biofabrication methods that have been employed in many TE applications in the last decade. The most common method of 3D bioprinting is extrusion bioprinting, in which a cell-encapsulated precursor, named as bioink, is deposited layer-by-layer to form the desired shape of the tissue construct upon proper crosslinking. The bioink's mechanical properties, mainly viscosity, are the crucial factors that determine whether a material is bioprintable or not. In general, there is a limited number of bioprintable hydrogels available on the market. A common strategy to solve this issue is tuning the bioink properties to make it compatible with extrusion bioprinting. The alternative is to modify the bioprinting method to expand the range of employable bioinks. For clinical translation, the bioprinted tissue constructs need to be shelf-ready. Currently, there is no biofabrication method available to create ready-to-use storable cell-laden hydrogel constructs. Developing such a biofabrication method to resolve both of these issues is the focus of the last phase of the present work. Therein, the invention and efficacy of a novel bioprinting method, cryobioprinting, is reported.

1.3 Literature survey

1.3.1 Composite hydrogels and inks

Composite materials are mixtures of two or more materials of different phases with significantly different properties [17]. In comparison with single-phase hydrogels, composite systems ideally have an improved/extended range of properties. Composite hydrogels offer increased versatility to attain the desired functions, such as enhancing biocompatibility, biological properties, porosity, mechanical characteristics, and physical performance [3]. "By incorporating at least one type of insoluble additive, such as fibers, nanotubes, or nanoparticles, into a single-phase matrix, composite hydrogels leverage the advantages of each individual component to achieve improved properties. The fibrous structure of several human native tissues, from soft tissues such as vocal fold lamina propria [18] to hard tissues such as musculoskeletal system [19, 20] motivates the use of composite hydrogels in the field of TE" [3].

Additive manufacturing has attracted tremendous attention due to its high versatility and

functionality. This technology rapidly found its place in several biological and biomedical applications, including but not limited to, inert implants and tissue-engineered implants [21–24], microfluidic devices and bioelectronics [25–27], organoid models and organon-a-chip platforms [28, 29], and other drug-screening systems [30]. A typical 3D printing instrument utilizes a printable material, termed the "ink", to fabricate prescribed constructs in a layer by-layer fashion. The incorporation of cells in the ink creates what is often called a "bioink," although this term is sometimes used for acellular materials in biomedical applications. The fabrication of cell-laden constructs is often denoted as bioprinting. Single-phase inks have been widely used for numerous applications in bioprinting and general printing. However, their uses have been long-bottlenecked by the limited choice of materials, low printability, insufficient mechanical performances, poor biomimicry, and lack of spatiotemporal controls [17]. The escalating need for printable materials with specific performances has spurred recent efforts on designing composite inks that are functional over a broader range of applications (Fig. 1.2).

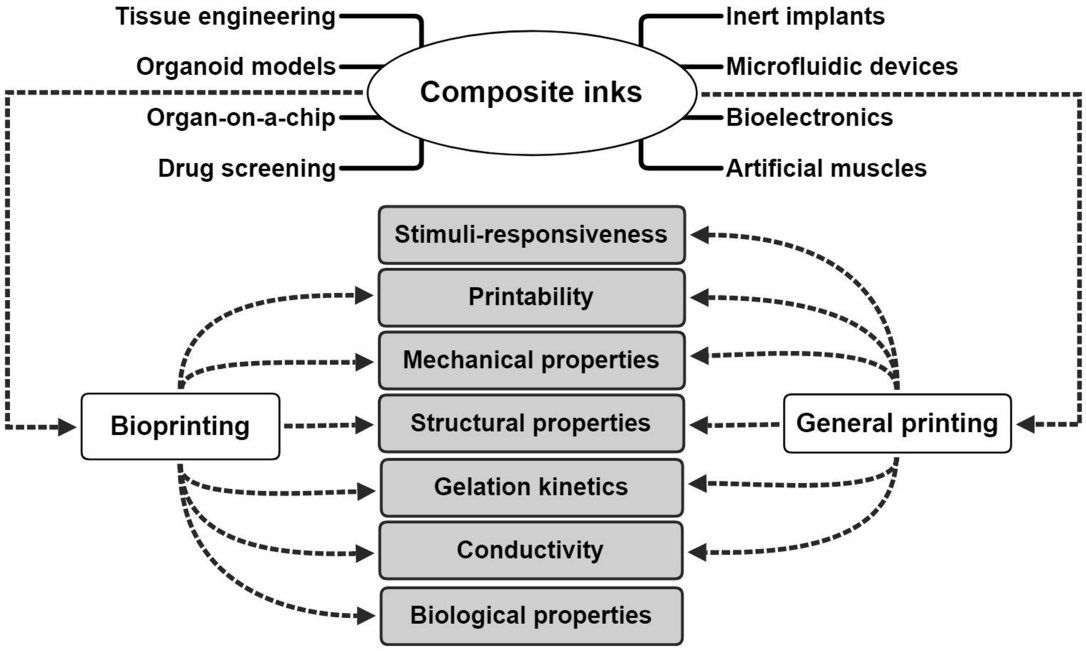

Fig. 1.2. Applications and performance targets of composite inks for extrusion (bio)printing. (Reprinted with permission from ref [3]. Copyright 2020 American Chemical Society.)

In general, composite inks outperform their single-phase counterpart in many aspects. For example, the addition of nanoclays can improve the printability of acrylamide and agarose hydrogels by enhancing their thixotropy [31]. Matrigel, a commercial composite hydrogel rich in fibrous proteins such as collagens and laminin, is a well-known bioink that is used in combination with other printable materials to achieve enhanced properties [32, 33]. For example, a Matrigel-agarose hydrogel can provide both proper printing fidelity and an excellent in vitro microenvironment for cell growth [34] due to the presence of agarose and fibrous proteins, such as collagen and laminin. With the aid of composite inks, the relatively new field of four-dimensional (4D) printing has been recently initiated via the addition of controllable shape-changing features to soft constructs [8, 35, 36].

1.3.2 Additives in composite hydrogels

Depending on the matrix and the additive, desirable enhancements in mechanical stability and printability of composite hydrogels may be obtained [37, 38]. As listed in Table 1.1, different types of fibers and nanotubes can be incorporated in soft hydrogel systems to fabricate composite hydrogels. In this section, the most common additives used in fabricating composite hydrogels and inks are briefly reviewed.

"**Collagen.** Collagen is the most abundant protein in the body. Over 30 different types of collagen can be distinguished, many of which comprise a long fibrous structure [53]. Collagen fibers are made of aggregations of fibrils, which have a triple-helix structure consisting of two alpha-1 and one alpha-2 polypeptide chains [39]. The most observable amino acid sequences in collagen are glycine-proline-X and glycine-X-hydroxyproline, where X can be any other type of amino acid [54]. Glycine, which has only one carboxylic group and one amine group without any side chains, is the main amino acid available in the chemical composition of collagen. Although collagen fibrils possess a larger stiffness than many other fibrous proteins (1∼2 GPa [55]), their mechanical properties deteriorate at temperatures above 40 °C [56]. Collagen is the main protein in the extracellular matrix (ECM). It is a biocompatible and biofunctional material, containing numerous cell-adhesion ligands [57]. Owing to these properties, collagen fibers have been extensively used in various composite hydrogels to enhance their intrinsic properties [58, 59]. For example, collagen/pluronic

Table 1.1. Characteristics of selected additives for fabrication of composite hydrogels.

Additive	Structure	Diameter	Young's modulus	Main advantage	Refs.
Collagen	Fiber	30∼300 nm	1∼2 GPa (Dry condition)	Abundant cell-binding ligands	[39, 40]
Fibrin	Fiber	40∼250 nm	1∼28 MPa	High extensibility (>330%)	[41–43]
cellulose nanocrystal (CNC)	Nanocrystal	2∼30 nm	20∼50 GPa	Tunable surface chemistry	[44–47]
cellulose nanofiber (CNF)	Fiber	10∼100 nm	20∼50 GPa	Shear-thinning properties	[45–50]
CNT	Nanotube	1∼2 nm (SWCNT) 5∼100 nm (MWCNT)	Up to 1.8 TPa	High stiffness, antimicrobial	[1, 51, 52]

composite hydrogels have a Young's modulus that is 3-9 times greater than that of the pure hydrogel [60]. Based on the rule of mixtures, this enhancement is due to the presence of the stiff collagen fibers in the matrix. It is also reported that cell proliferation and adhesion in agarose/collagen composites are significantly higher than in the corresponding single-phase hydrogel [61]. In some cases, rapid biodegradation is detrimental to tissue-engineering applications of collagen. A vapor-phase titanium-infiltration method has recently been reported to prolong the biodegradation of collagen fibers [62].

Fibrin. Fibrin, known as a natural fibrous coagulation protein, plays an important role in blood-clotting. It is obtained from the enzymatic transformation of fibrinogen. The physical and mechanical properties of the fibers, such as their density and Young's modulus, highly depend on their diameter [63]. The fibrin fiber diameter varies within the approximate range from 40 to 250 nm. Chloride ions can modulate the structure of fibrin fibers by inhibiting the formation of thicker fibers [64]. Thin fibrin fibers have a much greater Young's modulus than thick fibers, as the composition of protofibrils in the cross-section of thin fibers is denser.

As a result, thick fibrin fibers are easier to disperse [41] and are more suitable for preparing composite hydrogels. A unique characteristic of fibrin fiber is its outstanding extensibility, over 330% [65], which is attributed to the fact that the fiber becomes stiffer as mechanical strain is increased [42, 66]. The cytocompatibility and tunability of fibrin make it suitable for biological functions [67, 68],for example to promote cell adhesion [42, 69] or to induce angiogenesis [70].

Cellulose. Cellulose is the most abundant renewable organic polymer; it can be naturally produced or chemically synthesized. It is made of glucose units that form straight chains through hydrogen bonds [71]. The chemical composition of cellulose is $(C_6H_{10}O_5)_n$, where n denotes the degree of polymerization and, therefore, implies the number of glucose units. In contrast to pristine CNT (contact angle = 150∼160° [72]), cellulose is a hydrophilic material with a contact angle of 20∼30° [73]. The most popular derivative of cellulose for the fabrication of composite hydrogels is CNC. These tubular structures have a diameter in the range of 2∼20 nm [74]. The method of extraction leaves a sulfate half-ester group on the surface of CNCs [75] and makes it potent for surface-functionalization. As a result, functionalized CNCs are commonly utilized for enhancing cell−material interactions in composite hydrogels [76]. The hydrogen bonds within the chemical structure of CNCs increase their mechanical properties, including their tensile strength and their stiffness (Young's modulus of 167.5 GPa [77]). Consequently, CNCs are commonly used to mechanically reinforce hydrogels [78–80]. It has been reported that CNCs can also enhance the printability of alginate sulfate hydrogels [81]. Unique features of CNC-loaded composite hydrogels include temperature- and pH-dependent swelling [45, 82], which is helpful in fabricating stimuli-responsive composite hydrogels. Cellulose-based fibers, including CNC and CNF, are generally promising fiber additive for 3D-printing applications [83, 84].

CNT. Discovered in 1991 by Iijima [85], CNTs are known as one of the stiffest materials available, with Young's moduli of 1.8 TPa [86]. These nanomaterials are hollow tubes with high specific surface areas, solely composed of carbon atoms. Depending on the number of concentric tubes, CNTs are classified as single-walled carbon nanotubes (SWCNTs) and multi-walled carbon nanotubes (MWCNTs) (Fig. 1.3). The SWCNTs have diameters of approximately 1∼2 nm, while MWCNTs have a larger diameter of 5∼100 nm [87]. Both types of CNTs have been broadly used for reinforcing composite hydrogels [88–90]. For TE

applications, MWCNTs are more common as their dimensions are similar to those of fibrous proteins in the ECM [1, 91]. Unlike MWCNTs, SWCNTs easily penetrate the cell membrane and, therefore, are often used for drug delivery [92, 93]. In another classification, CNTs are divided into three major groups based on the orientation of the hexagonal arrangement of the sidewall; armchair, zigzag, and chiral [94]. The electrical properties of armchair CNTs are similar to those of metals, while zigzag and chiral CNTs behave as semiconductors [94]. These electrical characteristics have led to CNT usage for the fabrication of conductive 3D-printing inks [95–97].

Pristine CNTs are hydrophobic and aggregate into rope-shaped structures by means of weak van der Waals forces. The sidewall of a CNT consists of sp^2 carbons that can be hybridized by means of reactive double bonds. Hence, CNTs are very potent to be functionalized, either chemically or physically, with other moieties in a stable manner [98]. Functionalization with hydrophilic groups can increase the dispersibility of CNTs in aqueous media [99], which is essential in preparing CNT-based composite hydrogels. Surface-functionalization may remarkably enhance the electrical conductance of these nanomaterials [100]. The biocompatibility of CNTs has been controversial for several years, and there has been no consensus on it [101, 102]. This is one of the problems that is systematically studied in the present thesis. Since CNTs are synthetic materials, their biodegradation is of high importance, especially in TE applications. It has been reported that CNTs can be degraded by macrophages [103, 104], as well as different enzymes and chemical compounds, such as horseradish peroxidase [105, 106] and sodium hypochlorite [107]." In general, due to their simple structure the degradation mechanism of SWCNTs is faster than that of the MWCNTs.

1.3.3 Cell-material interaction in CNT composite hydrogels

Fiber additives in composite hydrogels can hypothetically mimic the structure of fibrous proteins in the ECM. Considering this resemblance, CNT composite hydrogels have been extensively studied for different in vitro applications, such as skin growth, osteoblastic cell differentiation and proliferation, and brain circuit stimulation [109]. "Much work has been done on the interactions between CNTs and various cell types, from neurons to osteoblast and stem cells [101, 109, 110]. The reported range of CNT concentration without

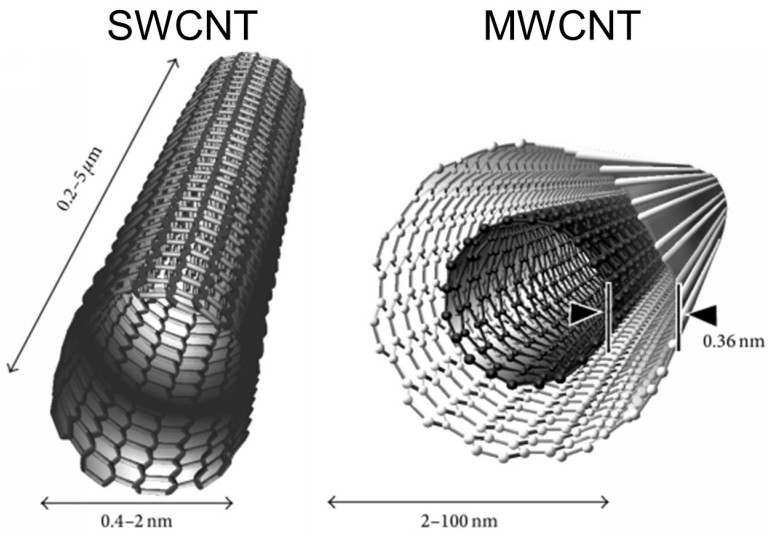

Fig. 1.3. Schematic illustration of SWCNTs and MWCNTs. (Adapted from ref [108] under the terms of the CC BY 3.0 license.)

significant cytotoxicity varies considerably, between only a few nanograms per ml [111] to several milligrams per ml [112]. These results indicate that CNTs' cytotoxicity varies with different cell types [113]," thereby necessitating further studies on this matter. Although the biocompatibility of CNTs is still a subject of research, "it is generally accepted that functionalized CNTs are more biocompatible than pristine CNTs [114–119]."

For TE applications, composite hydrogels should ideally allow sufficient cell adhesion and cell migration within their network. Such cell-biomaterial interaction is known to accelerate wound healing and tissue regeneration in the target region [120, 121]. "By studying the impacts of adding covalently grafted adhesion ligands and epidermal growth factor to polyethylene glycol hydrogels, Gobin and West demonstrated the importance of cell adhesion in promoting cell migration in hydrogels [122]. Latifi et al. qualitatively showed that adding collagen type III to GC hydrogel increases the fibroblasts attachment to the surface of the hydrogel [123]." Previous researchers have used cell morphology such as area, axial ratio, perimeter, major axis, and minor axis to quantify cell adhesion [124, 125]. Another parameter that affects cell adhesion in composite hydrogels is the stress relaxation time [126]. "The mechanical viscoelastic properties of the hydrogel are also an important factor for adhesion.

Van den Broeck et al. successfully modulated the mechanical properties of CNT/polyethylene glycol composite hydrogels by changing the concentration of MWCNTs, without jeopardizing the cytocompatibility of the biomaterial [127]." It is hypotheticized that MWCNTs, which due to their size are more practical for TE applications, can be used as focal adhesion sites to enhance cell adhesion for anchorage-dependent cells, such as fibroblasts [128, 129]. This may lead to an increased cell migration rate in CNT-loaded composite hydrogels. The larger diameter of MWCNTs with respect to SWCNTs approximates the physical characteristics of fibrous proteins, such as collagen and elastin, in the ECM. This idea is feasible based on recent findings, in which CNTs have been employed in hydrogel matrix to mimic the fibrous structure of the ECM [127, 129–131].

Several methods have been so far suggested to study cell migration. "Scratch assays, transwell assay systems, cell-exclusion zone assays, microfluidic-based assays, and radial cell migration protocols have been used to characterize cell migration in two-dimensional (2D) cell culture environments [132–136]. Most of these methods are focused on cells' behavior rather than on cell-biomaterial interactions. Fewer methods are available for 3D scaffolds, whereby migration is usually quantified based on the distance traveled by the cells or the number of migrated cells [137]. Li et al. used human hepatocyte growth factors and cell culture inserts to demonstrate the effects of growth factor-loaded nanoparticles on cell migration in hydrogels [138]. They used a confocal microscope to count the number of migrated cells in random zones in the hydrogel. Heris et al. also used confocal microscopy, but in time-lapse, to evaluate the average speed of cells that were homogenously encapsulated in hyaluronic acid/gelatin composite hydrogels [121]. In the absence of any directional constraints, however, the random motion of the cells tends to dominate motility statistics, which may be misleading. A method that leads cells across the scaffold boundary would help better characterize the ability of a priori acellular materials to recruit cells from their surrounding environment. The optimum design for cell migration experiment is, therefore, a configuration that can capture the total number of migrated cells and minimize the influence of the cells' random motion or possible biases due to hydrogel swelling over the duration of the experiment."

1.3.4 Bioprinting

The method of fabricating constructs from a digital 3D model in a layer-wise [139] or volumetric [140] programmed manner is called 3D printing. The flexibility, versatility, and functionality of 3D printing enable the fabrication of exquisite and intricate structures [8, 141, 142] with a resolution down to hundreds of nanometers [143]. One emerging branch of 3D printing is 3D bioprinting [144, 145], in which a combination of cells, growth factors, and biomaterials is used as the printing material, to create biological constructs. As an evolving field of biofabrication, 3D bioprinting is being extensively used in myriad applications including TE [146, 147], regenerative medicine [148], organ-specific tissues [149], patient-specific grafts [150], tissue model engineering [151], and drug screening [30], among others. Depending on the application and the bioink properties, various technologies including nozzle-based and laser/light-based techniques are being developed for 3D bioprinting. Extrusion [152] and inkjet [153] are the most common modalities of the nozzle-based bioprinting, while laser-induced forward transfer (LIFT) [154] and vat-polymerization [155] are the two categories of laser/light-based 3D bioprinting [156]. Fig. 1.4 schematically demonstrate the four major modalities of bioprinting methods. The second phase of this thesis focuses on extrusion bioprinting.

Extrusion bioprinting is based on fabricating constructs on a bioprinting platform using a viscoelastic bioink extruded from the nozzle(s) (Fig. 1.4A). The extrusion force can be applied by means of pneumatic actuation or mechanical impulses [157]. Different approaches are being used for crosslinking the bioprinted structures, including physical, chemical, and photocrosslinking [158]. Extrusion method is straightforward, convenient, and low-cost so that users have developed handheld and portable devices for this purpose [159–163]. However, the nature of extrusion, especially for viscous materials, necessarily entails a high level of shear stress, which can jeopardize cell viability [164]. Using small-diameter nozzles for the sake of enhancing the bioprinting resolution not only leads to excessive shear stress to the cells but also limits the bioprinting throughput, resulting in prolonged bioprinting time. Another challenge with the extrusion bioprinting method is the limited availability of printable shear-thinning biomaterials [165], in which the viscosity decreases under shear stress. Furthermore, the lack of stable in situ crosslinking methods for non-shear-thinning bioinks, the low printing

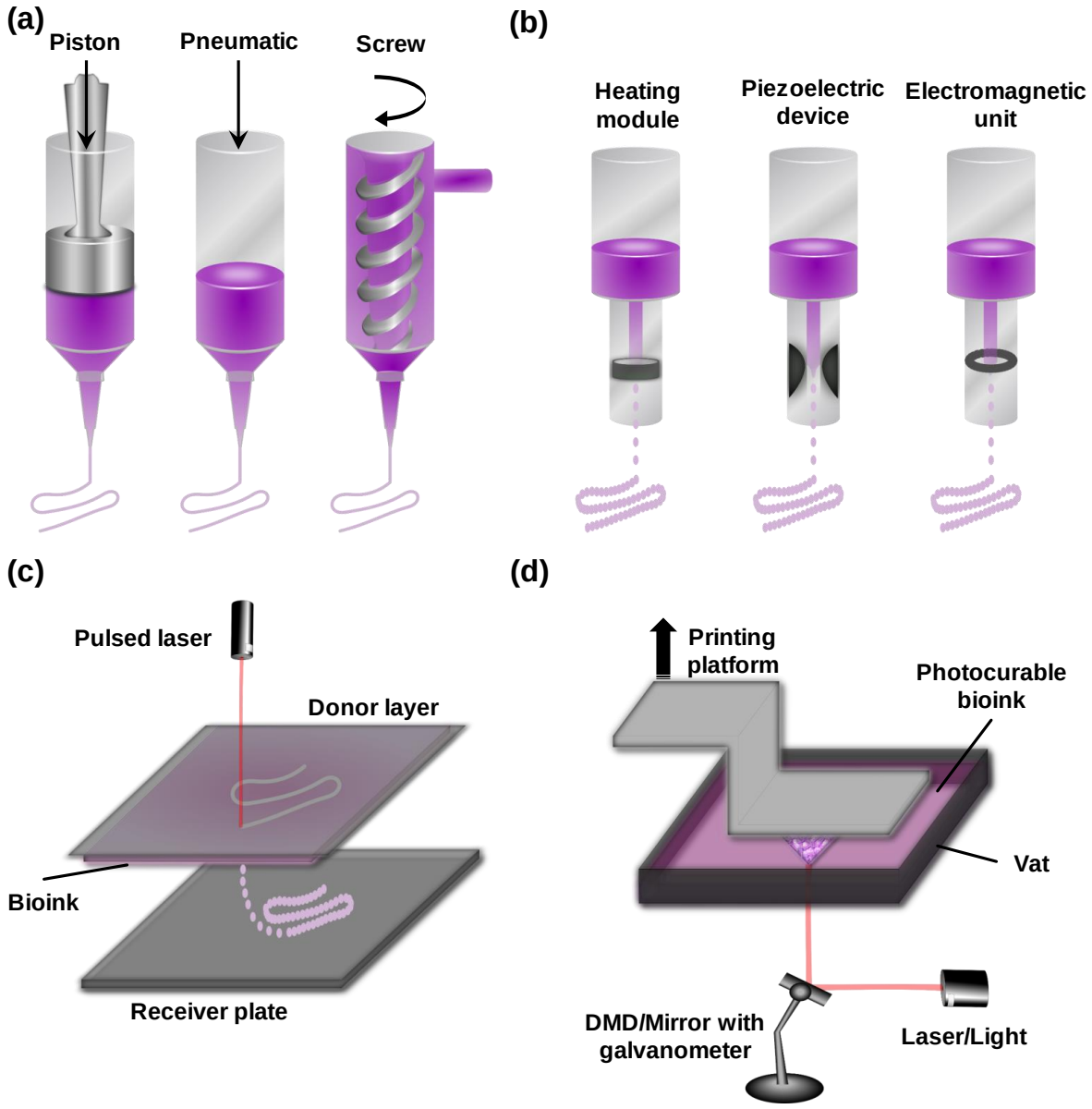

Fig. 1.4. Schematic showing the different bioprinting modalities. (a) Extrusion. (b) Inkjet. (c) LIFT. (d) Vat-polymerization.

resolution [166], and complications in fabricating free-standing constructs [167, 168] other limitations of extrusion bioprinting. These shortcomings have spurred the modification of the

conventional extrusion methods, leading to the development of new technologies, among which co-axial/core-shell bioprinting [169] and embedded bioprinting [170] are the most well-known alternatives.

A critical challenge associated with the current bioprinting modalities is the fabrication and storage of shelf-ready 3D-bioprinted tissue constructs. This issue is specifically important in clinical translation of this method, where surgeons prefer to access ready-to-use tissue constructs for implanting in the human body. Due to the intrinsic complexities of most bioprinting processes, using this method as an on-site fabrication technique can be cumbersome under a number of scenarios. Furthermore, the lack of a functional approach for long-term storage of cell-laden tissue constructs [171] precludes the shelf-availability of pre-made bioprinted products. A potential solution to address the obstacles mentioned above is combining the fabrication and storage methods, i.e., bioprinting and cryopreservation. As such, the bioprinted tissues can be fabricated in advance off-site, allowing direct storage in cryogenic conditions for later academic, industrial, or clinical demands. To this end, the bioink should be properly designed so that the cells are efficiently cryopreserved during bioprinting and the storage/resuscitation periods. Despite its complications in selecting effective cryoprotective agent (CPA)s, cryopreservation has been widely used in clinical and academic research [172, 173]. In recent years, new methods such as microfluidics [174], bulk droplet vitrification [175], and superflash freezing [176] have been proposed to preserve cell viability and biological functionality during cryopreservation. These methods are, unfortunately, incompatible with constructing cryopreserved bioprinted tissues. CPAs are believed to have a critical effect on precluding or minimizing ice crystal-formation [177]. In the absence of CPAs, the ice crystals grow within the bioprinted construct and may jeopardize cell viability by damaging the cell membranes during the freezing process [178]. dimethylsulfoxide (DMSO) is a traditional CPA widely used in cryopreservation [179–181]. Nevertheless, the potential cytotoxicity of DMSO at high concentrations has spurred more efforts to find CPAs with higher cell survival rates [182–184]. Among these CPAs, various disaccharides such as sucrose [185], trehalose [186], lactose [187], and maltose [188] together with trisaccharides such as raffinose [189] and melezitose [188] have shown promising cryoprotective effects.

1.4 Research objectives

The general framework of the present study was to suggest and validate methods of design and fabrication of hydrogels via using composite biomaterials and cryobioprinting method to enhance their compatibility for TE applications. To this end, hydrogels' composition as well as their fabrication process were engineered. Specifically, CNTs were used as additives to make composite hydrogels, which were postulated to enhance the properties of the target hydrogel. Furthermore, a novel biofabrication method, cryobioprinting, was developed to facilitate the clinical translation of the bioprinted hydrogel constructs. The feasibility and efficacy of the cryobioprinting method was assessed through a set of cell viability, cell differentiation, and angiogenesis experiments. We envision that the outcome of this project can take us one step closer to the clinical translation of cell-laden tissue implants. The specific aims of this project were defined as follows.

Specific aim 1: Investigating the effect of CNTs on the mechanical, biological, and physical properties of the composite hydrogels.

In the first phase of this project, the goal was to utilize the unique properties of CNTs in hydrogels for mimicking the fibrous network of proteins in the ECM. The electrical properties of the CNTs can be potentially used to fabricate actuated tissue constructs. The primary concern in using CNTs was their biocompatibility. Cell viability tests were employed to investigate this concern and quantify to what extent may the CNTs affect the cells. At the same time, the addition of CNTs could change the mechanical and physical properties of the composite hydrogel. These effects were quantified thru measuring the rheological properties, gelation time, swelling ratio, and the pore size of the composite hydrogels with different CNT concentrations.

Specific aim 2: Developing a quantification method to study cell adhesion and cell migration in 3D scaffolds.

The second phase of this study mainly focuses on quantification of cell-biomaterial interaction. After investigating the peripheral effect of adding CNT to composite hydrogels, the major parameters that directly influence tissue regeneration within the scaffold were evaluated. Cell adhesion and cell migration are the two main variables analyzed to capture their dependency on the CNT concentration. Image processing approaches and flow cytotmetry method were

exploited to quantitatively measure cell adhesion and cell migration. By implementing this method for composite hydrogels, it was demonstrated how CNTs promote cell migration and cell adhesion within the scaffolds' network.

Specific aim 3: Developing a novel biofabrication method, cryobioprinting, for fabricating shelf-ready storable tissue constructs.

In the third phase of this project, the fabrication method of hydrogel constructs was tuned to enhance the performance of the bioprinted products. The final aim is to turn bioprinted constructs into storable products with potential on-demand applications. To this end, a synergistic approach consisting of bioprinting and cryopreservation was proposed to create shelf-ready storable tissue constructs. Extrusion bioprinting was utilized to bioprint cell-laden tissue constructs on a freezing plate. The frozen structures could be readily stored for future on-demand clinical and educational applications. To ensure the feasibility of the method, cell viability experiments were conducted after reviving the samples. Furthermore, the functionality of the cryobioprinted cells were verified through cell differentiation and chicken ex ovo experiments.

CHAPTER 2

Materials and methods

This chapter covers the experimental and numerical methods used throughout the dissertation. The details related to materials selection, cell-related experiments, imaging methods, mechanical tests, physical characterization, and finite element analysis are elaborated. The chapter is divided into four main sections including non-biological experiments, biological experiments, statistical analysis, and numerical methods. Unless otherwise mentioned, all materials were purchased from Sigma-Aldrich. The sentences in quotations are verbatim of the author's publications (references [1, 2]).

2.1 Non-biological experiments

2.1.1 Hydrogel synthesis

Two types of hydrogels were synthesized for studying the effect of material constituents and fabrication process. Firstly, carbon nanotube glycol chitosan (CNT-GC) hydrogel was prepared as a composite hydrogel to investigate the effect of carbon nanotube (CNT) on the performance of the hydrogel in different aspects. Then, gelatin methacryloyl (GelMA) was synthesized from gelatin to be used as the bioink for cryobioprinting. The synthesis steps for both hydrogels are detailed in this section.

CNT-GC composite hydrogel. Carboxylic acid- and hydroxyl-functionalized multi-walled carbon nanotubes (MWCNTs) (purity> 95%, OD: 50–80 nm) were provided by US

Research Nanomaterials Inc. (Houston, TX, USA). CNTs were dispersed in water before incorporation into the hydrogel to prevent agglomeration. In cell viability experiments, the use of surfactants to facilitate CNT dispersion was avoided to merely study the impact of CNTs on cell viability. "A probe sonicator (Fisher Scientific, Sonic Dismembrator Model 100) was utilized to homogeneously disperse the functionalized CNTs. The probe sonicator delivered 12-15 W of acoustic power and was found to be more effective than a bath sonicator. A stock solution of CNTs in water was prepared and sonicated. The resulting suspension was then centrifuged for 5 min at 2500 rpm to deposit the undispersed agglomerates at the bottom of the test tube." The sonication-centrifuging process was repeated twice, followed by transmission electron microscopy (TEM) and scanning electron microscopy (SEM) of the sample, to verify the size and dispersion of the CNTs. The concentrations were then measured gravimetrically. The homogeneous suspension, which was stable for several weeks, was subsequently diluted to obtain the final desired concentration.

Glycol chitosan (GC) powder with a degree of polymerization of 2000 was purchased from Chemos GmbH, Germany. A concentration of 5% (w/v) glycol chitosan solution was prepared in phosphate-buffered saline (PBS) (Wisent Inc.) using a Fisher Scientific rotator for 24 h. CNT-GC composite hydrogel was prepared using 2% (w/v) GC solution as the matrix, different concentrations of CNT and 0.005% (w/w) glyoxal as the crosslinker. The aldehyde group of glyoxal reacts with the amine group of the GC to form a Schiff-base compound and crosslink the hydrogel. "For biological tests, a cell density of 2 million human vocal fold fibroblast (HVFF)s per ml was used for encapsulating in the hydrogel immediately before adding the crosslinker. All composite hydrogel constituents were autoclaved. All preparations were done under a cell culture hood in aseptic conditions to minimize the risks of contamination."

GelMA cryoprotective bioink. GelMA was prepared based on a previously developed protocol [190]. Briefly, porcine skin gelatin- type A was dissolved in PBS with a concentration of 10% (w/v) at 50 ℃. Methacrylic anhydride was then added drop-by-drop using a syringe pump until a concentration of 5% (v/v) was reached and the chemical reaction (Fig. 2.1) was initiated. The emulsion was mixed on a magnetic hot plate for 2 h at 50 °C to ensure homogeneity. GelMA was then diluted twice and dialyzed using distilled water at 40 °C for 5 days. The distilled water was changed every 12 h. The solution was filtered at 40 °C

using a 0.22-µm Stericup-GP Sterile Vacuum Filtration System (Millipore). The filtered solution was then aliquoted into 25-ml lots and stored at -80 °C for 24 h.The frozen GelMA was lyophilized for 5 days at 0.2 mbar and 24 °C in a FreeZone Labconco freeze dryer. The desired amount of lyophilized GelMA was then dissolved in a pre-mixed solution of PBS and 0.6% (v/v) 2-hydroxy-4-(2-hydroxyethoxy)-2-methylpropiophenone (Irgacure 2959) as photoinitiator. The resulting solution was used as the base bioink for cryobioprinting.

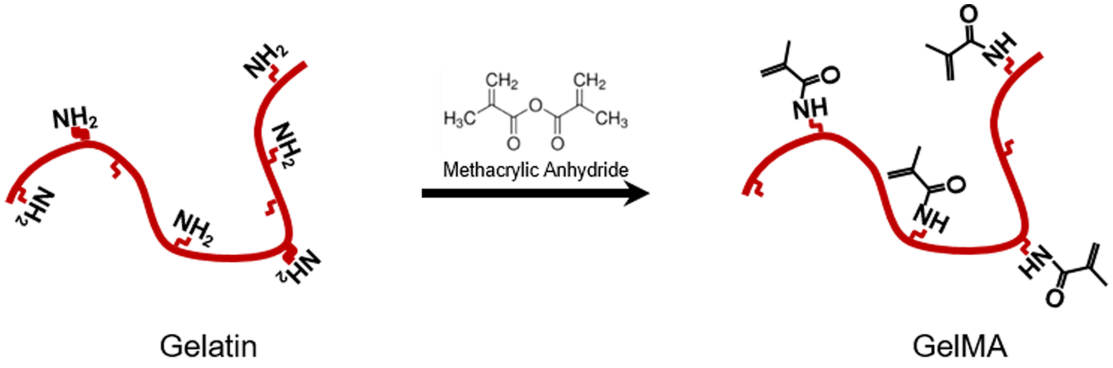

Fig. 2.1. Chemical reaction for synthesizing GelMA by introducing methacryloyl substitution group on the reactive amine and hydroxyl groups of the amino acid residues. (Adapted from ref [191] under the terms of the CC BY 4.0 license.)

GelMA at a final concentration of 5% (w/v) was used as the main constituent of the cryoprotective bioink. dimethylsulfoxide (DMSO), along with different saccharides, listed in Table 2.1, were added as the cryoprotective agent (CPA). D-(+)-trehalose dihydrate, D-lactose, sucrose ultrapure, D-(+) raffinose pentahydrate, and D-(+)-melezitose hydrate were purchased from Alfa Aesar. The saccharides' concentration (0%, 4%, 8%, 12% (w/v)) and the DMSO concentration (0%, 5%, 10%, 15% (v/v)) were systematically studied to identify the optimal values based on cell viability results.

2.1.2 Transmission electron microscopy

"The length, diameter, and wall structure of the CNTs were visualized using TEM images. A drop of 2 mg ml^{-1} CNT solution was imaged using a Philips CM200 TEM equipped with an AMT XR40B CCD camera and EDAX Genesis EDS. The images were collected with an

Table 2.1. The properties of the saccharides used in cryobioprinting.

Sugar	Molecular formula	Solubility at 20 °C (g ml^{-1})	Density (g cm^{-3})	Type
Trehalose	$C_{12}H_{22}O_{11}$	0.689	1.58	Disaccharide
Lactose	$C_{12}H_{22}O_{11}$	0.216	1.52	Disaccharide
Sucrose	$C_{12}H_{22}O_{11}$	2.100	1.59	Disaccharide
Raffinose	$C_{18}H_{32}O_{16}$	0.203	1.8	Trisaccharide
Melezitose	$C_{18}H_{32}O_{16}$	0.781	1.8	Trisaccharide
Maltose	$C_{12}H_{22}O_{11}$	1.080	1.54	Disaccharide

accelerating voltage of 200 kV. The length and diameter measurements were performed in ImageJ software (National Institute of Health)."

2.1.3 Scanning electron microscopy

Images obtained from SEM were employed for two purposes: (i) to check the dispersion of CNTs in the CNT solution, and (ii) to measure the pore size of the CNT-GC network. For the first aim, a droplet of the CNT solution with the concentration of 2 mg ml^{-1} CNT was imaged via the SEM machine, and the disperssion of the CNTs were visually investigated. For the second purpose, the CNT-GC hydrogel samples were frozen for 24 h after curing. "The frozen samples were lyophilized in a ModulyoD 5 L freeze dryer (Thermo Fisher Scientific) under 290 $\pm$ 10 μbar at room temperature for 24 h. An FEI F50 scanning electron microscope (Thermo Fisher Scientific) was then employed to image the network of the hydrogel groups. ImageJ software was used for analyzing the SEM images and determining the average pore size for each study group."

2.1.4 Rheological characterization

"A single head rotational rheometer (Discovery Hybrid HR-2, TA Instrument, DE) equipped with a 20 mm parallel plate was employed to determine the rheological properties of hydrogels with different CNT concentrations. Shear strain values below 5% were used to remain in the elastic region. Selected based on the cell viability results, CNT concentrations of 250, 500, and 750 μ g/ml along with a CNT-free control group were used for rheological

characterization." Triplicates were used for measuring the gelation time and mechanical properties of the samples.

Gelation time. "Time-sweep experiments were conducted with a rotational frequency of 1 Hz and a shear strain of 0.1% at the human body temperature, 37 °C. The rheometer was controlled with the Trios software (TA Instrument, DE). The gap size between the rheometer plates was adjusted to 1000 μm to provide a reproducible loading. Each sample was prepared in an Eppendorf vial and injected between the two plates to completely fill the gap. Time-sweep tests were performed immediately after injection over a period of 1 h, spanning the entire crosslinking period. A solvent trap (TA Instrument, DE) was used in order to avoid sample dehydration during the time-sweep tests. The storage and loss moduli (G' and G", respectively) were recorded during the crosslinking period to determine the gelation time.

Two methods are commonly used to measure the gelation time of hydrogels. In the first method, the gelation point is defined as the instant when the ratio between G' and G" becomes independent of the frequency. The other method is based on the intersection of G' and G" curves in a time-sweep test, indicating a transition from liquid phase to solid phase." In this dissertation, the second method was used.

Mechanical characterization. "After the time sweep tests, the sample was kept under a solvent trap for 14 h to ensure complete curing. Frequency-sweep (0.01 to 10 Hz) tests were then performed with a 0.1% of shear strain at 37 °C. The viscoelastic properties, such as the storage modulus, the loss modulus, and the complex viscosity (η) were measured and compared for different study groups."

Stress relaxation. The fully-crosslinked samples, which were kept under the rheometer plate for 14 h, underwent a constant torsional strain of 10%, and the corresponding stress in the hydrogel was recorded over a period of 3 h. "The recorded stress time history was used to quantify the stress relaxation rate for hydrogels with different CNT concentrations."

2.1.5 Swelling

To quantify the capacity of the hydrogel groups in water absorption, triplicate samples of CNT-GC hydrogel with different CNT concentrations were prepared in Eppendorf vials and crosslinked in a 37 °C incubator for 4 h, as previously mentioned in Section 2.1.1. "After curing, the samples' initial weight (W_i) was measured using a high-precision balance (Quintix, Sartorius, precision=1mg). PBS 1x was then added to the hydrogels, and the samples were exposed to agitation on an orbital shaker (VWR 3500, Radnor, PA, United States) at 75rpm. On days 0, 1, 3, 7, 14, and 30, PBS was removed, and the samples' weight was recorded as the swollen weight (W_s)." The swelling ratio (%SW) was calculated based on the sample weight increase percentage at the above-mentioned time points (Eq. (2.1)). After weight measurement, the samples were stored in −80 °C for further physical characterizations.

$$\%SW = \frac{W_s - W_i}{W_i} \times 100\,. \tag{2.1}$$

2.1.6 Enzymatic degradation

To examine the enzymatic biodegradation of the study groups, 1 ml of hydrogel samples with the pre-mentioned CNT concentrations was synthesized in 2 ml Eppendorf vials. After complete gelation at 37 °C, all samples were frozen in −80 °C, and then lyophilized in a ModulyoD 5 L freeze dryer (Thermo Fisher Scientific) at 290 ± 10 μbar and room temperature. Each of the freezing and lyophilizing steps lasted for 24 h. A high-precision balance (Quintix, Sartorius, precision = 1mg) was then used to measure the dry weight of the hydrogels, W_{di}.

The enzyme solution was prepared by dissolving lysozyme powder (Thermo Fisher Scientific, Approx. 20,000 units/mg dry weight) in PBS 1x. The concentration of lysozyme was 500 μg/ml, which is the same as that of the human airway and nasal fluid [192]. A volume of 1 ml of enzyme solution was added to the freeze-dried hydrogels, and the samples were agitated using the same orbital shaker employed in Section 2.1.5. Using triplicates, the biodegradation behavior of the four study groups (different concentrations of carboxylic acid-functionalized carbon nanotubes (COOH-CNTs)) was examined on days 0, 1, 3, 7, 14, and 30, for a total of 72 samples. The enzyme solution was refreshed every other day to

stabilize the enzymatic reaction. At each time step, the supernatant was removed from one set of samples, and stored in −80 °C. On day 31, when all the samples were frozen, they were lyophilized for a second time for 24 h. The final dry weight of the samples, W_{df}, was measured using the same balance. The samples' degradation was quantified as the percentage of remaining weight, %RW, shown in Eq. (2.2).

$$\%RW = \frac{W_{di} - W_{df}}{W_{di}} \times 100\,. \tag{2.2}$$

2.1.7 Measurement of the pH

"The pH values of CNT solutions and hydrogels were measured using an electronic SevenEasy pH meter (Mettler Toledo). The measurements were performed at room temperature."

2.1.8 Ice crystal imaging

The ice crystals' growth in cryobioprinting method was assessed for different cryoprotective bioinks. The hydrogel groups were cast on a freezing plate to study the effect of DMSO concentration on ice crystals formation. A volume of 25 μL of the precursor was deposited on the freezing plate. The freezing process was recorded using a brightfield microscope eyepiece camera (GXCAM-D800 - GT Vision Ltd) mounted on a Leica EZ4 stereomicroscope (Leica Camera AG). Different concentrations of DMSO and melezitose were used in the hydrogels. The ice crystal formation was quantified by processing the video frames using the GRABIT open-source code and a customized script in MATLAB (Mathworks).

2.2 Biological Characterization

2.2.1 Cell culture

HVFFs were cultured in Dulbecco's Modified Eagle Medium (DMEM) (Wisent Inc.) contained 10% (v/v) fetal bovine serum (FBS), 1% (v/v) penicillin-streptomycin, and 1% (v/v) non-essential amino acids at 37 °C, in a 5% CO_2 humidified incubator to conduct the cell-related

experiments in CNT-GC hydrogel groups. "The cells were cultured in treated T75 flasks with filter caps (Thermo Fisher Scientific). Cell culture media were replaced every other day. When the desired level of confluency was reached, the cells were washed in PBS, and the adherent cells were detached from the flask surface using a 0.25% trypsin-ethylenediaminetetraacetic acid (trypsin-EDTA) solution." The cells were then encapsulated in composite hydrogel groups to be cultured in a three-dimensional (3D) network. A Bright-Line hemocytometer (Sigma-Aldrich Corporate) was used to roughly count the number of cultured cells before the encapsulation in hydrogels.

For cryobioprinting, seven types of cells, including mouse embryonic fibroblast cell line (NIH/3T3), immortalized mouse myoblasts (C2C12), human liver cancer cell line (HepG2), human breast cancer cell line (MCF-7), human primary smooth muscle cells (SMCs), human umbilical vein endothelial cells (HUVECs), and human mesenchymal stem cells (hMSCs), were separately cultured. DMEM(Thermo Fisher Scientific) enriched with 10% (v/v) FBS (Thermo Fisher Scientific) was used for culturing NIH/3T3, C2C12, HepG2, and MCF-7 cells. SMC growth medium, which was supplemented with 5% (v/v) FBS, 0.1% (v/v) insulin, 0.2% (v/v) human fibroblastic growth factor-basic (hFGF-b), 0.1% (v/v) gentamicin sulfate-amphotericin (GA-1000), and 0.1% (v/v) human epidermal growth factor (hEGF) (Lonza Biologics), was used for culturing SMCs. HUVECs were cultured in endothelial cell growth medium supplemented with 2% (v/v) FBS, 0.04% (v/v) hydrocortisone, 0.4% (v/v) hFGF-b, 0.1% (v/v) vascular endothelial growth factor (VEGF), 0.1% R3 insulin-like growth factor 1 (IGF-1), 0.1% (v/v) ascorbic acid, 0.1% (v/v) hEGF, 0.1% (v/v) GA-1000, and 0.1% (v/v) heparin (Lonza Biologics). Mesenchymal stem cell growth medium supplemented with 0.1% (v/v) GA-1000, 2% (v/v) L-glutamine, and 10% (v/v) mesenchymal cell growth supplement (Lonza Biologics) was used to culture hMSCs. The media were changed every 3 days until confluency of approximately 80% was achieved. After removing the media and washing with Dulbecco's phosphate-buffered saline (DPBS) 1x (Alfa Aesar), the cells were dissociated using 0.05% (v/v) trypsin-EDTA (Thermo Fisher Scientific).

2.2.2 Cell viability

"As a preliminary study to assess the cytotoxicity of CNTs, small quantities of CNT powder were added to the cell culture media. The cells were observed under a brightfield microscope (Olympus CKX41) every day for two weeks. Since no differences were observed in terms of cells growth, a set of experiments was designed to quantify the biocompatibility of CNTs in contact with HVFFs. To this end, samples made of 250 ml hydrogel with different CNT concentrations were prepared in 8-well μ-slides (Ibidi, Martinsried, Germany) using the method described in Section 2.1.1." "Due to the very diverse and even conflicting reports on maximum CNT doses without compromising the biocompatibility, cell viability tests were initiated with a very low CNT concentration. Solutions with low (10, 20, 40, 80 μg/ml), medium (250, 500, 750 μg/ml) and high (2000, 4000, 8000 μg/ml) CNT concentrations were used to identify the maximum possible concentration without significant cytotoxicity. In each set of experiments, a CNT-free hydrogel was used as the negative control." "An estimated 2 million cells per ml of HVFFs were homogenously encapsulated in hydrogel groups. The samples were cured at 37 °C, in a 5% CO_2 humidified incubator for 1 h. Cell culture media was subsequently added on the samples. The media was changed every other day." "The cells were stained using a live/dead kit (Invitrogen, Carlsbad, CA) prior to imaging on days 0, 4, and 7. Green and red fluorescent lights were used in confocal laser scanning microscopy (CLSM) to image live and dead cells, respectively. The Z-stack feature of the CLSM (Zeiss LSM710, Oberkochen, Germany) was used for image acquisition using the Zen software (Zeiss, Oberkochen, Germany). The images were reconstructed and analyzed using the image processing software Imaris 8.3.1 (Bitplane, Switzerland) (see the Supplementary file). The viability rate was determined based on reconstructed images by calculating the ratio between the number of live cells and the total number of cells."

For cryobioprinting, cell viability was quantified within unthawed cell-encapsulated samples to identify the optimal combination of CPAs. Following the crosslinking and washing steps, the hydrogel samples were cultured for a definite period and then stained using calcein-AM and ethidium homodimer-1 (Thermo Fisher Scientific) per the provider's protocol. An inverted Eclipse-Ti fluorescence microscope (Nikon) was employed to image the live and dead cells in green and red channels, respectively. The ratio of live cells to the total captured cells

in random regions of the samples was determined through processing the fluorescent images using the ImageJ software (National Institutes of Health). Four replicates were used for each study group. The three groups of hydrogel/CPA with the highest relative cell viability values were selected for further experiments.

2.2.3 Cell recruitment

The study groups with different CNT concentrations used in Section 2.2.2, were studied to assess their capability in recruiting cells. Hydrogel samples were prepared in plastic vials, as described in Section 2.1.1. "Prior to gelation, 50 μl of the cell-free hydrogel was placed on the center point of each well in an 8-well μ-slide to form a semi-spherical shape (Fig. 2.2). The samples were then incubated for 45 min until they were fully crosslinked. The cells were passed and stained using Vybrant Dil cell-labeling solution (Invitrogen, Carlsbad, CA). A volume of 200 μl of the cell solution, with a concentration of 500,000 cells per ml, was added to each well to cover the hydrogel droplet. To ensure the stability of the cells and the hydrogel, the samples were incubated for 24 h prior to imaging. CLSM was used to record cells' movement over a period of 14 h. The acquisition and analysis of the time-lapse images were conducted using Zen 2.6 and Imaris 8.3.1, respectively.

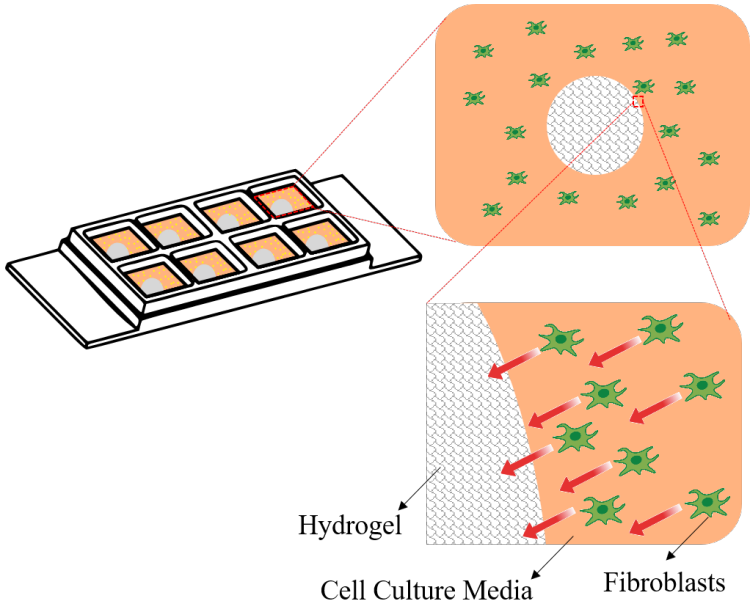

Fig. 2.2. "Schematic configuration of the cell recruitment experiment. Due to their anchorage-dependence, the fibroblasts move toward the hydrogel droplet and in some cases penetrate it." (Adapted from ref [2] under the terms of the CC BY 4.0 license.)

The regions of interest for imaging were the border edges of hydrogel droplets, where the cells may penetrate the hydrogel."

2.2.4 Chemoattractant-induced cell migration

Cell migration in CNT-GC composite hydrogels with different CNT concentrations was studied using a modified Boyden Chamber experiment (Fig. 2.3). "A gradient of chemoattractant media was employed to initiate cell mobility. Delta-treated polycarbonate cell culture inserts with a pore size of 8 μm in 12-well plates (Thermo Fisher) were used for 3D cell culture. The fibroblasts were passed, counted, and encapsulated in hydrogel. Since the overall migration rate was predicted to be small [193], we aimed for an initial population of 1-1.4 million fibroblasts in each insert to obtain enough migrated cells for comparison. Prior to gelation, 200 μl of the hydrogel was transferred from the vials to porous inserts. The samples were then incubated at 37 °C with 5% CO2 for 1 h to complete the gelation process and expose the cells to a serum starvation period, which can potentially accelerate migration. Afterwards, 200 μl of serum-free DMEM was added on the hydrogels' surface, and the inserts were suspended over the 12-well companion plate, which contained 400 μl of completed DMEM + 10% FBS." "The samples were incubated for one week. The completed DMEM + 10% FBS was regularly replaced with fresh media every other day to ensure the stability of the chemoattractant gradient. On day 7, the media was removed, and the inserts were gently washed with PBS 1x. The migrated cells were then dissociated from the bottom of the inserts by adding 200 μl of 0.25% (v/v) trypsin-EDTA and rocking the plate. After 2 min of incubation, 800 μl of fresh completed DMEM was added to the cell solution to avoid cell digestion. The migrated cells solution was then collected for cell counting via flow cytometry."

2.2.5 Flow cytometry

"A FACSCanto II flow cytometer (BD Biosciences, San Jose, CA) was employed to count the number of migrated cells in CNT-GC hydrogel. A volume of 50 μl of counting beads (Precision Count Beads, Biolegend, San Diego, CA) with a concentration of 1.03×10^6 particles/ml was added to 500 μl of the cell solution prior to flow cytometry. The size and the internal structural complexity of the beads are different from those of the fibroblasts. No

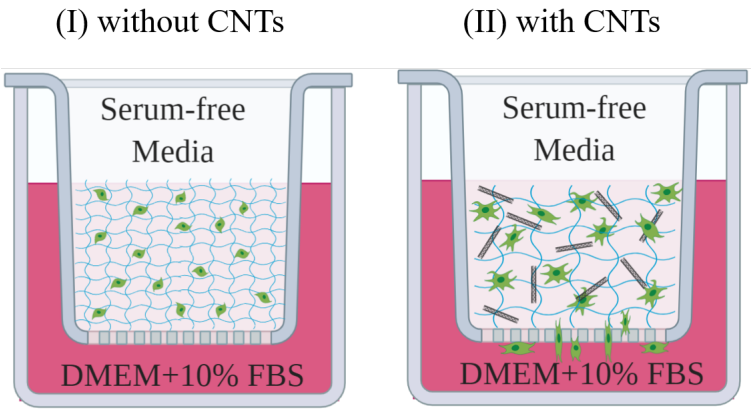

Fig. 2.3. "Schematic of chemoattractant-induced cell migration assay using a modifed Boyden Chamber experiment." (Adapted from ref [2] under the terms of the CC BY 4.0 license.)

staining was therefore needed to distinguish the beads from the cells. They were separated based on their forward scattered area (FSC-A) and side scattered area (SSC-A) signals, as schematically shown in Fig. 2.4. Flow cytometry-based cell counting highly depends on the precision of solution volumes. A reverse pipetting method was used when transferring solutions to minimize errors.

The FACSDIVA software, version 8 (BD Biosciences, San Jose, CA) was used for data acquisition. For each series, a volume of 550 μl of the cell solution was gently vortexed and loaded on the flow cytometer. The data was collected until 10^4 particles were recorded, or the sample was fully used, whichever occurred first. Data analysis was conducted using the FlowJo software, version 10.5.3 (BD Biosciences, San Jose, CA)." The number of counting beads and the number of migrated cells were determined by defining proper gates in FlowJo, as will be discussed in Chapter 3.

2.2.6 Cell adhesion

The hydrogels with encapsulated fibroblasts were prepared as mentioned in Section 2.1.1 and Section 2.2.1. "The cell density in the hydrogel was set to 4×10^5 cells per ml. A volume of 200 μl of hydrogel was added in each of the 8 wells of a μ-slide, and the samples

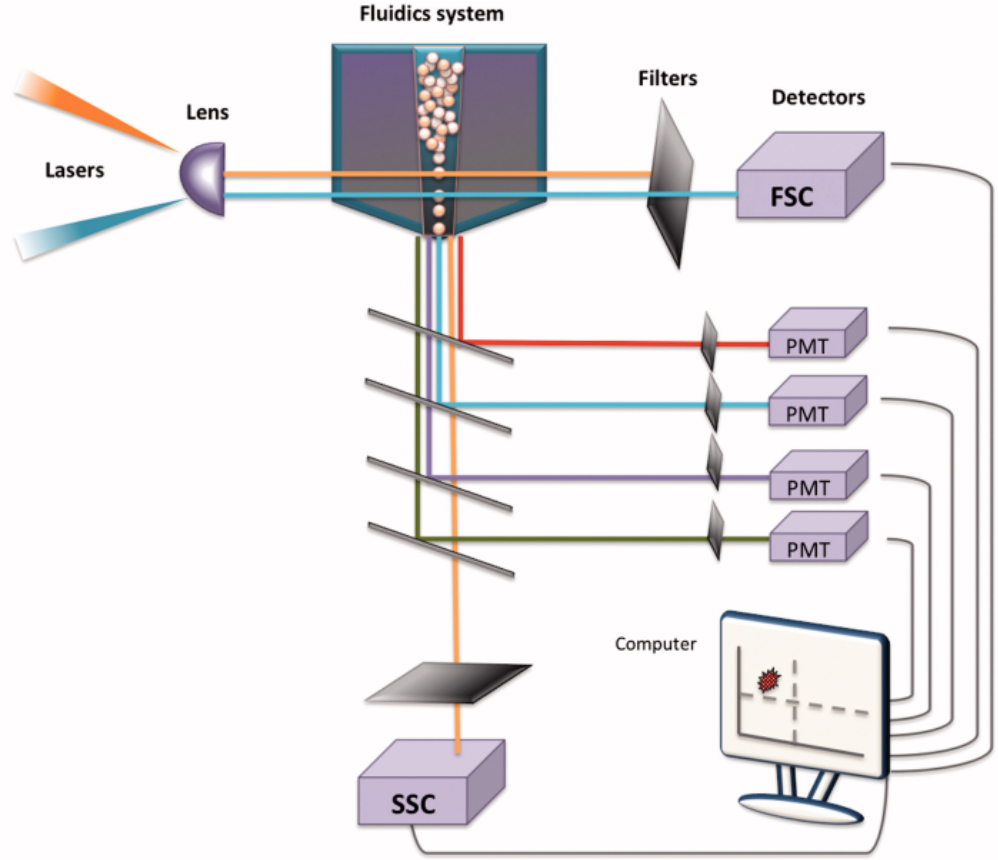

Fig. 2.4. Illustration of the flow cytometry-based cell counting approach using FSC-A and SSC-A signals. (Reprinted with permission from ref [194]. Copyright 2017 Taylor & Francis.)

were incubated over 1 h. A volume of 250 μl of cell culture media containing completed DMEM + 10% FBS was then added to the samples. The hydrogel samples were incubated for 72 h to allow enough time for the cells to adhere to the hydrogel network. On day 3, the cells were fixed using 3.7% (v/v) methanol-free formaldehyde (Acros Organics) and permeabilized with Triton X-100. The samples were immersed in 1% (w/v) bovine serum albumin (BSA) solution for 30 min to decrease possible background noise during imaging. Alexa Fluor 633 Phalloidin staining solution (Invitrogen, Carlsbad, CA, United States) was used to stain the F-actin filaments of the fibroblasts. The cells' nuclei were also stained using DAPI. The samples were washed with 37 °C prewarmed PBS, between each step. The CLSM images

were used to visualize the cells' F-actin filaments structure. Subsequently, the images were processed in MATLAB to quantify the extent of cell adhesion based on the morphology of the F-actin filaments."

2.2.7 Cryobioprinting

Fig. 2.5 depicts the cryobioprinting procedure. A continuous extrusion bioprinter, Allevi 2, was used for cryobioprinting. The Repetier-Host (Hot-World GmbH & Co. KG) and Cura (Ultimaker) software packages were employed to process the models and generate the corresponding G-codes. A self-designed and manually assembled freezing plate (Fig. 2.6) was used as the bioprinting substrate. The needle size, pressure, and printhead speed were selected based on the printability results (see Chapter 4). The cell-encapsulated GelMA/CPA was kept at 4 °C for 20 min before bioprinting to enhance the viscosity of the bioink. The samples were bioprinted on the freezing plate and stored in -80 °C or liquid nitrogen.

2.2.8 Cryopreservation

To identify the optimal CPA configuration, 96 groups of GelMA samples (four DMSO concentrations, four saccharide concentrations, and six types of saccharides) were studied. C2C12 cells were encapsulated in the GelMA/CPA precursor. A volume of 50 μL of the cell-laden precursor was directly cast on the freezing plate in aseptic conditions. The frozen samples were immediately stored at -80 °C or in liquid nitrogen (-196 °C) for cryopreservation. On day 3, the samples were removed from cryogenic storage and directly crosslinked via ultraviolet (UV) exposure. The samples were washed in DPBS to remove any excess CPAs in preparation for subsequent use.

2.2.9 Cell differentiation

The hMSCs were encapsulated in the selected groups of GelMA/CPA to be used as the bioink. The cryobioprinted samples were stored at -80 °C overnight and were then transferred to liquid nitrogen for cryopreservation. On day 14, the samples were UV-crosslinked and revived. After 3 days of culture, the three types of differentiation media, i.e. adipogenic,

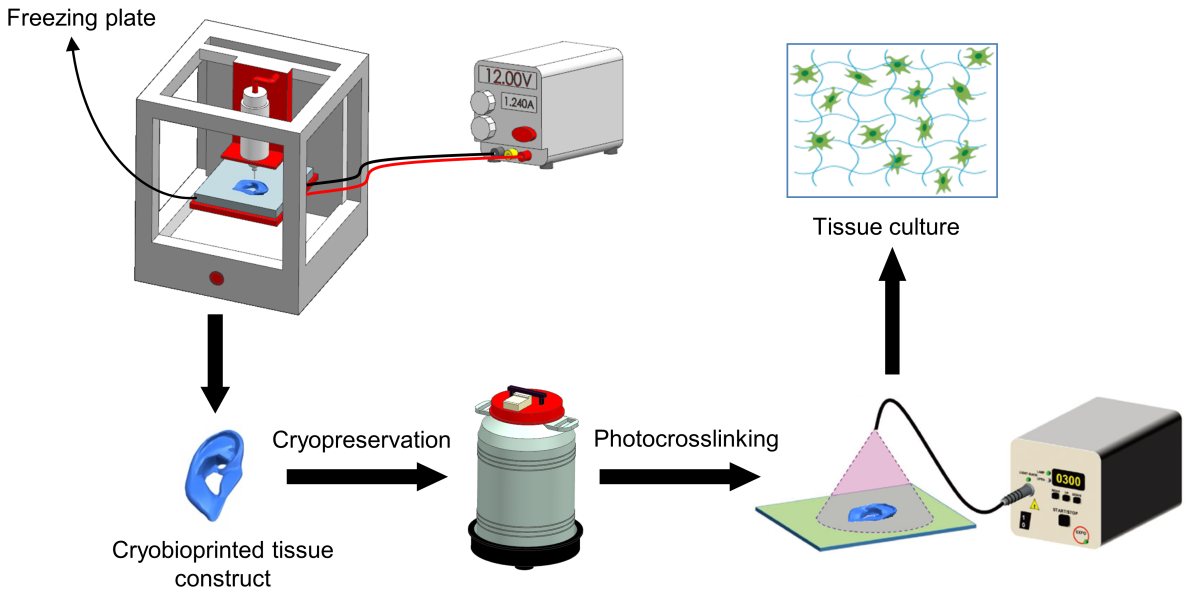

Fig. 2.5. Schematic illustration of cryobioprinting of tissue constructs for simultaneous cryopreservation. The cell-laden bioink is cryobioprinted on a freezing plate with tightly controlled temperature and kept in cryogenic conditions for long(er)-term preservation. The cryobioprinted structure can be then transferred, revived, and crosslinked immediately before subsequent culturing to achieve tissue formation at the desired usage site.

osteogenic, and chondrogenic, were separately added. The constructs were cultured in DMEM (4.5 g L^{-1} of D-glucose) supplemented with 1-μM dexamethasone, 5-μg mL^{-1} insulin, and 50-μM indomethacin [7] to induce adipogenesis. Osteogenesis was conducted by culturing the constructs in DMEM (1 g L^{-1} of D-glucose) supplemented with 10-mmol L^{-1} β-glycerophosphate, 300-µmol L^{-1} L-ascorbic acid, and 100-nmol L^{-1} dexamethasone [7]. For chondrogenic differentiation, the constructs were cultured in DMEM (4.5 g L^{-1} of D-glucose) supplemented with 50-μg L^{-1} ITS+ Premix Tissue Culture Supplement, 100-nmol L^{-1} dexamethasone, 1-μM ascorbate-2-phosphate, and 10-ng mL^{-1} transforming growth factor-β1 [195]. At certain timepoints, i.e. day 7, day 14, and day 21, Oil Red O, Alizarin Red S, and Alcian blue (all from ScienCell Research Laboratories) were used for staining the samples and characterizing adipogenesis, osteogenesis, or chondrogenesis.

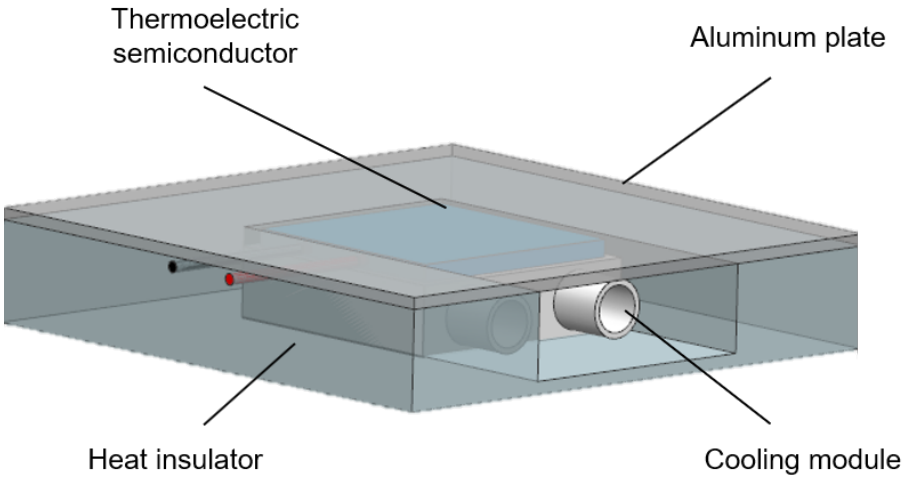

Fig. 2.6. Schematic of the freezing plate used as the substrate for cryobioprinting. The freezing plate was cooled using a pair of semiconductors, which were powered by a DC voltage generator. The surface temperature could be adjusted by changing the output voltage on the DC power. The semiconductors were cooled down via a water-based cooling module.

2.2.10 Immunostaining

For immunofluorescence staining, the anti-PPARγ, anti-RUNX2, anti-osteocalcin, or anti-SOX-9 antibodies (all from Abcam) were diluted in PBS to achieve a final concentration of 200 μg L^{-1} and incubated overnight at 4 °C for adipogenesis, osteogenesis, or chondrogenesis. The samples were washed with PBS and then stained with the corresponding secondary antibodies. The samples were washed again with PBS, and fluorescence micrographs were captured using an inverted fluorescence microscope.

2.2.11 Chorioallantoic membrane (CAM) assay

The ex ovo chick CAM culture was undertaken following the guidelines used in the previous studies [196, 197]. For preparing the VEGF group, the cryoprotective bioink was supplemented with 100 ng mL^{-1} of VEGF (PeproTech) [198]. The eggshells were carefully cracked to start the ex ovo culture 3 days after incubation. The cryobioprinted scaffolds were implanted in chick embryo CAM on day 7. The samples were then incubated for 7 days until they were

collected for imaging. We used 10% (v/v) formalin to fix the samples for inspecting the angiogenesis. An optical camera (Canon EOS 60D) was used for imaging. To quantify the extent of vascularization, the discernible blood vessel (BV) lengths on the cryobioprinted constructs were measured using the NeuronJ tracing toolbox of ImageJ [196].

2.2.12 Histology

The samples collected from the CAM assays were fixed in 10% (v/v) formalin for 24 h. The fixed samples were then dehydrated, embedded in paraffin wax, and then serially sectioned (5 μm in thickness). Goldner's trichrome staining involved the use of Weigert's hematoxylin, ponceau-fuchsin-azophloxin (erythrocytes), phosphomolybdic acid (cytoplasm), and light green (collagen) [199]. BV densities and ratios of BV-to-tissue areas in different groups were calculated to quantify the angiogenesis [200].

2.3 Statistical analysis

The quantitative results were reported in mean values ± standard deviations (n = 3 or greater). The built-in two-tailed paired and unpaired student's T-test function of MS Excel (Microsoft) was accordingly employed for statistical analysis. A P-value threshold of 0.05 was considered to distinguish between significantly different data sets.

2.4 Numerical simulation of heat transfer

Heat transfer simulation was used to better understand the mechanism of the deposited bioink on the freezing plate during the cryobioprinting process. To simulate a two-layer 8 × 8-mm^2 grid structure in COMSOL Multiphysics, each layer was generated by sweeping a 2-mm-thick rectangle over a defined bioprinting path. The simulation parameters are listed in Table 2.2. Heat transfer in the porous hydrogel was modeled by defining proper boundary conditions and using time-marching schemes. Each layer was divided into 45 sections. The computational domain was discretized using an unstructured grid of free tetrahedral meshes with a maximum size of 0.28 mm and a minimum size of 0.12 mm. The top and the side boundaries were

defined so that the convection heat transfer with the ambient medium was considered. The cryobioprinting procedure was simulated by imposing a step-function temperature increase on the bottom surface of the bioprinted section, which contacts the freezing plate. The bottom surface of successive sections was exposed to the low temperature, i.e., the freezing plate temperature, to simulate cryobioprinting deposition kinematics. Considering the printing speed, the sections were exposed to the low temperature every 0.16 s, one at a time. After the first layer was entirely deposited, the second layer was assembled section by section on top of the first layer. For the second layer, the continuity condition was applied to equate the temperature of the second layer's bottom surface with that of the first layer's top surface.

Table 2.2. Heat transfer simulation parameters.

Parameter	**Value**
Thermal conductivity (W m^{-1} K^{-1})	0.57
Density (kg m^{-3})	1,000
Heat capacity (J kg^{-1} K^{-1})	4,136
Ratio of specific heats	1.33
Bioink's initial temperature (°C)	15
Ambient temperature (°C)	20

CHAPTER 3

Carbon nanotube (CNT)-based composite hydrogels

In this chapter, the influence of carbon nanotube (CNT) additives on the performance of the glycol chitosan hydrogels are discussed. Different groups of injectable carbon nanotube glycol chitosan (CNT-GC) hydrogels are studied in series of physical, rheological, and biological tests. The effects of CNT concentration and functional groups on the viability rate of human vocal fold fibroblast (HVFF) cells are investigated. The maximum allowable CNT concentration based on the cell viability rates is determined, and all the other experiments are designed based on this limit. The mechanical properties, such as stiffness and stress relaxation time, and the gelation time of the study groups are evaluated via rheometry tests. Swelling assays are conducted to evaluate water absorption capacity. The pore size of the hydrogels are measured based on the scanning electron microscopy (SEM) images. Cell recruitment, migration, and adhesion in the three-dimensional (3D) network of the composite hydrogels are assessed. A new parameter, the extensibility ratio, is introduced and used to compare cell adhesion in different samples. The biodegradation of the hydrogels with different CNT concentrations is also determined over time. The results support the plausibility of using CNT-based composite hydrogels as a synthetic scaffold for tissue engineering (TE) applications. The sentences in quotations are verbatim of the author's publications (references [1, 2]).

3.1 Characterization of CNTs

3.1.1 Dimensions

Transmission electron microscopy (TEM) images were used to determine the inner diameter (ID), outer diameter (OD), length, and structure of the CNTs. In Fig. 3.1 two TEM images with different levels of magnification are presented. It is apparent that the actual OD of the CNTs following 20 min of sonication is 45 ± 5 nm, which is roughly 30% less than the nominal diameter reported by the provider. An excessive sonication power/time can cause breakage and shortening of the nanotubes as well as unzipping of the CNTs' exterior walls. As a result, the sonication time/power should be carefully selected so that while the CNTs are dispersed, minimal defect is introduced to the CNTs.

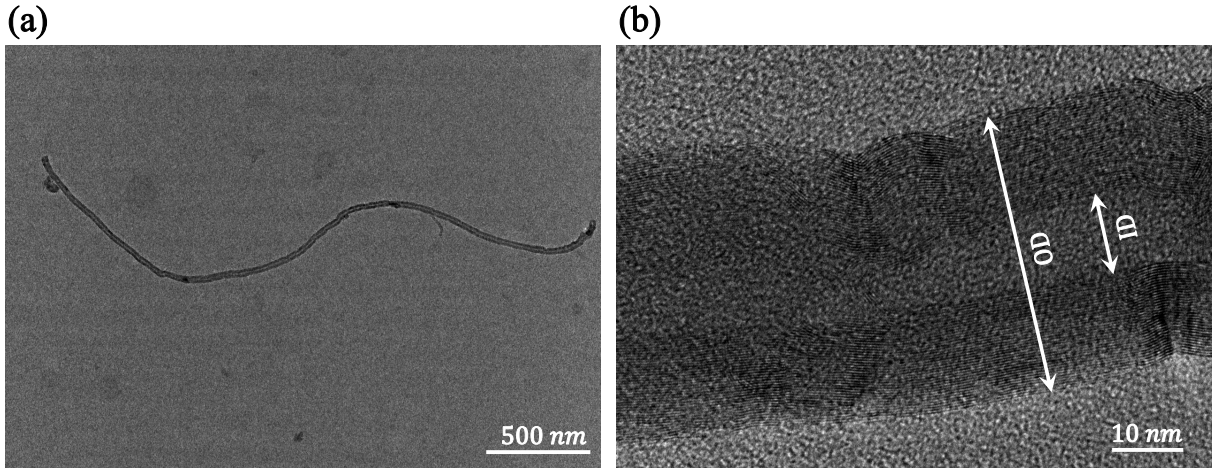

Fig. 3.1. Representative TEM images of MWCNTs for estimating **(a)** the length and **(b)** the diameter of CNTs. (Reprinted with permission from ref [1]. Copyright 2019 Elsevier.)

3.1.2 Dispersion

The quality of CNT dispersion can be visually checked using SEM images. Fig. 3.2 depicts a well-dispersed CNT solution with a concentration of 2 mg ml^{-1}, where the CNTs were homogeneously distributed in the solution. The SEM images are also helpful in assessing

the extent of defects in CNTs. Damaged CNTs are indicated by white arrows in Fig. 3.2. The majority of the CNTs were however intact (shown by black arrows). "Insufficient sonication energy may imperfectly debond the agglomerations. After a few iterations, the proper sonicator output power and sonication time was determined so that minimum damage to the nanotubes was introduced while the CNTs were being dispersed. For carboxylic acid-functionalized carbon nanotubes (COOH-CNTs) and hydroxyl-functionalized carbon nanotubes (OH-CNTs), the optimum duration of sonication with an acoustic power of 12 − 15 W was found to be 12–18 min and 15–23 min, respectively." Considering the shorter required sonication time, it was deduced that the COOH-CNTs were more hydrophilic and dispersible in water comparing to OH-CNTs.

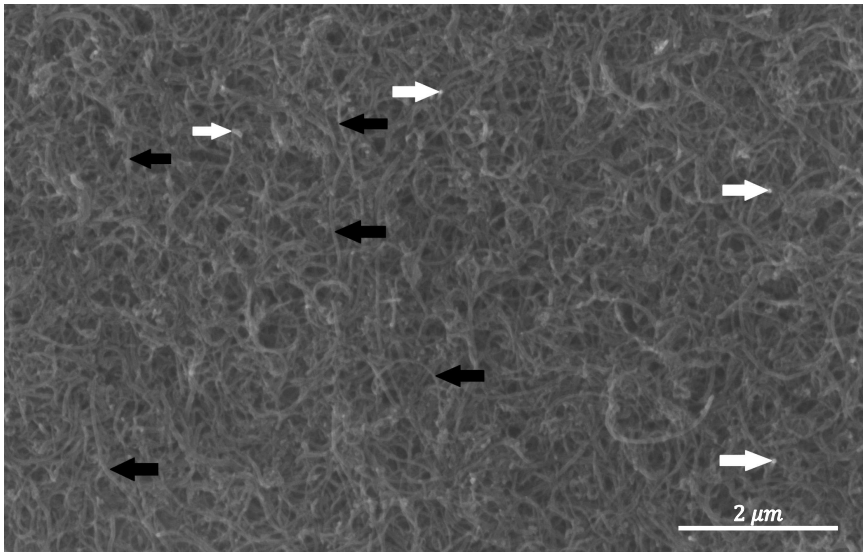

Fig. 3.2. Representative SEM images of a well-dispersed lot of COOH-CNTs suspension. The bright points indicated with the white arrows are CNTs' breakage points. The black arrows point to the long intact CNTs without visible damage. (Reprinted with permission from ref [1]. Copyright 2019 Elsevier.)

3.2 Physical characterization

The primary effect of adding CNTs to hydrogels is changing the physical properties. Swelling and pore size are the two physical parameters that are evaluated for the study groups in this section. Different groups of composite hydrogels are denoted based on their CNT concentration. For example, CNTxxx represents a CNT-GC composite hydrogel group with a concentration of xxx μg ml^{-1} of CNTs.

3.2.1 Swelling behavior

"Fig. 3.3 shows the effect of COOH-CNTs concentration on the composite hydrogel swelling ratio over a period of one month. On day 30, the swelling ratio for samples with CNT concentrations of 0, 250, 500, and 750 μg ml^{-1} were 24%, 27.5%, 28%, and 29%, respectively. This observation shows that water permeability increased by 5% in the first month following the addition of COOH-CNTs. The samples with COOH-CNTs reached their maximum swelling ratio more rapidly than the control sample. This phenomenon shows that CNT-loaded composite hydrogels may stabilize faster in the body." The addition of OH-CNTs did not visibly affect the swelling behavior of the hydrogels, and the swelling ratio for all the samples, including the control sample (glycol chitosan (GC) without CNT), was measured to be 4% after 30 days.

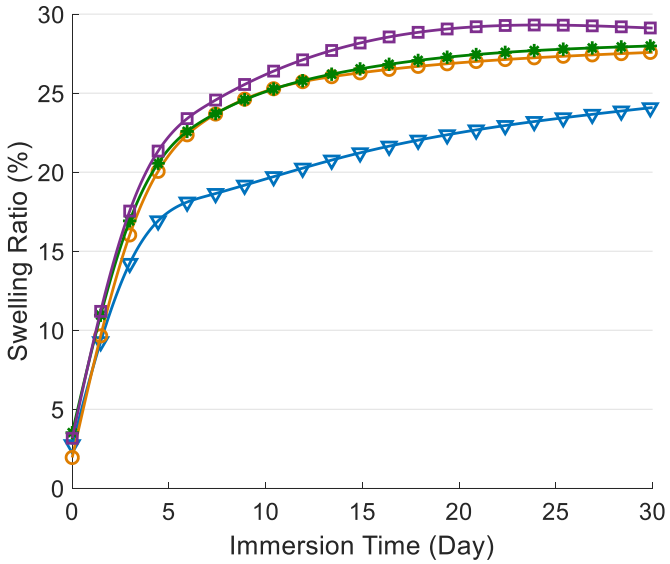

Fig. 3.3. Swelling ratio for different COOH-CNTs groups during the first month of immersion in PBS (Triangle: Control, Circle: CNT250, Asterisk: CNT500, Square: CNT750). (Reprinted with permission from ref [1]. Copyright 2019 Elsevier.)

3.2.2 Enzymatic biodegradation

The biodegradation of the CNT-GC composite hydrogels over a time period of 30 days was evaluated. Since the target organ in this study is human vocal folds, lysozyme, a native enzyme that is abundant in human secretions such as saliva and nasal fluids, was used to study the biodegradation process. Lysozyme can degrade the GC hydrogel groups to glucosamine, which is nontoxic to cells [201]. "Fig. 3.4 shows the decrease in samples' weights while they were exposed to lysozyme. The samples were degraded to about one-half of their initial weight over the one month period. The biodegradation rate during the first week was greater than that over the following weeks. On day 7, the control and the CNT250 samples were degraded to 70% of their initial weight. The two study groups with higher CNT concentration, i.e., CNT500 and CNT750, were degraded to about 60%. Starting from day 14, the degradation rate for all the samples decreased and reached a plateau. In general, the addition of CNTs did not significantly affect the long-term biodegradability of the CNT-GC composite hydrogels." The degradation of the CNTs is previously studied, and it was demonstrated that CNTs can be degraded by macrophages and other native enzymes, such as horseradish peroxidase [104, 105].

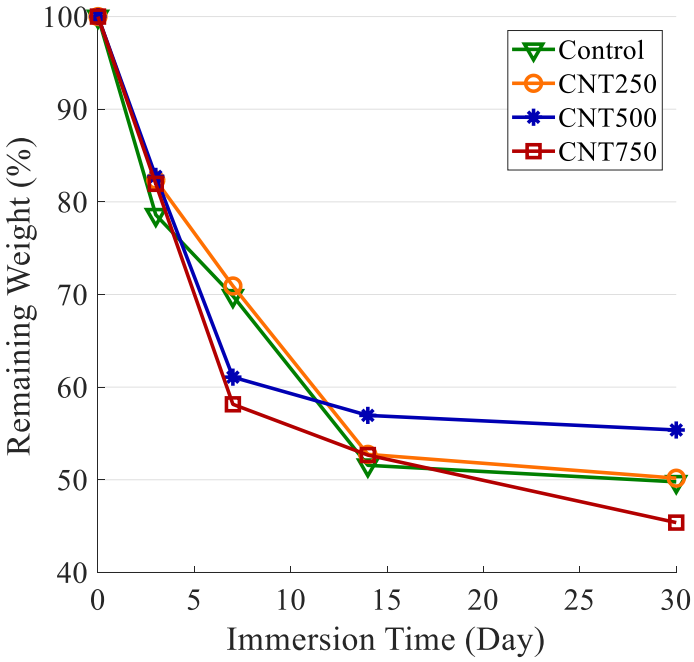

Fig. 3.4. The biodegradability of the CNT-based composite hydrogels based on weight loss when immersed in lysozyme solution (Triangle: Control, Circle: CNT250, Asterisk: CNT500, Square: CNT750). (Adapted from ref [2] under the terms of the CC BY 4.0 license.)

3.2.3 Pore size

Fig. 3.5 shows representative snapshots of the SEM images taken from the hydrogels network. As it is visually apparent, the addition of CNTs led to the enlargement of composite hydrogels' pore size. The SEM images were analyzed using the ImageJ software to quantify the influence of the CNT concentration on the pore size. "Fig. 3.6 depicts the distribution of the measured pore size in each sample. The average pore size of the hydrogels with 250, 500, 750 μg ml^{-1} of COOH-CNTs was increased by 33%, 73%, and 120%, respectively based on the control sample." Interestingly, the addition of OH-CNTs did not cause any significant increase in the pore size.

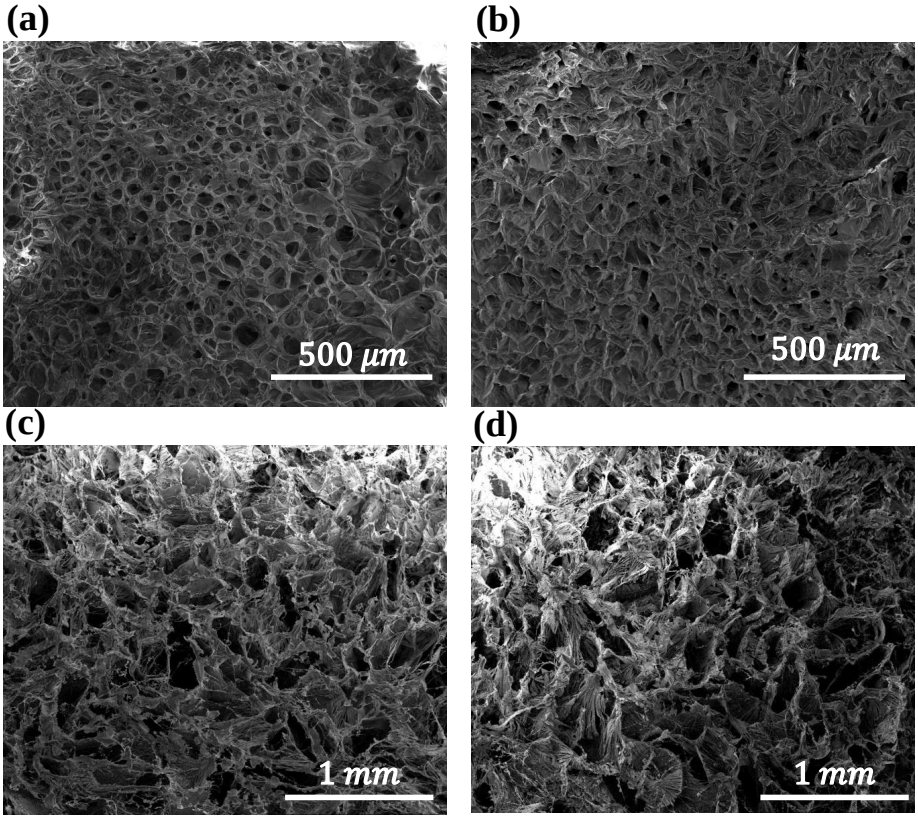

Fig. 3.5. Representative SEM images taken from the hydrogel surfaces to measure the average pore size for different COOH-CNT concentrations; **(a)** Control, **(b)** CNT250, **(c)** CNT500, **(d)** CNT750. (Reprinted with permission from ref [1]. Copyright 2019 Elsevier.)

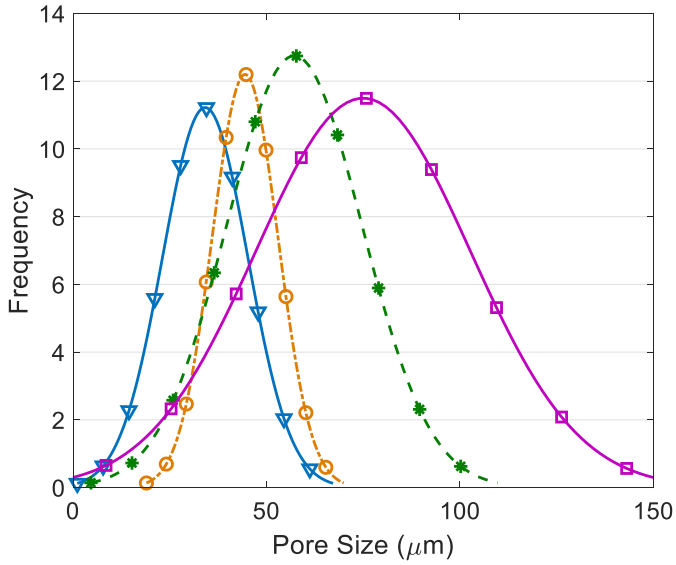

Fig. 3.6. The pore size distribution for the COOH-CNTs composite hydrogels (Triangle: Control, Circle: CNT250, Asterisk: CNT500, Square: CNT750). (Reprinted with permission from ref [1]. Copyright 2019 Elsevier.)

3.3 Rheological characterization

3.3.1 Gelation time

Rheology experiments were conducted to investigate composite hydrogels' viscoelastic properties, which are vital in developing an injectable biomaterial. Time sweep tests revealed that both the storage and shear moduli increased during the crosslinking period. As mentioned in Section 2.1.4 and depicted in Fig. 3.7, the intersection of storage modulus and shear modulus curves is considered as the gelation point. In Fig. 3.8-a, b, the gelation time of samples with different CNT concentrations and different functional groups are compared. It is demonstrated that the addition of CNTs up to the concentration of 250 μg ml^{-1} caused faster gelation process. "Increased CNT concentration tended to postpone gelation. In the case of OH-CNTs hydrogels, increasing the CNT concentration to values higher than 750 μg ml^{-1}, which is still in the biocompatible range, did not highly affect the gelation time (Fig. 3.8-b)."

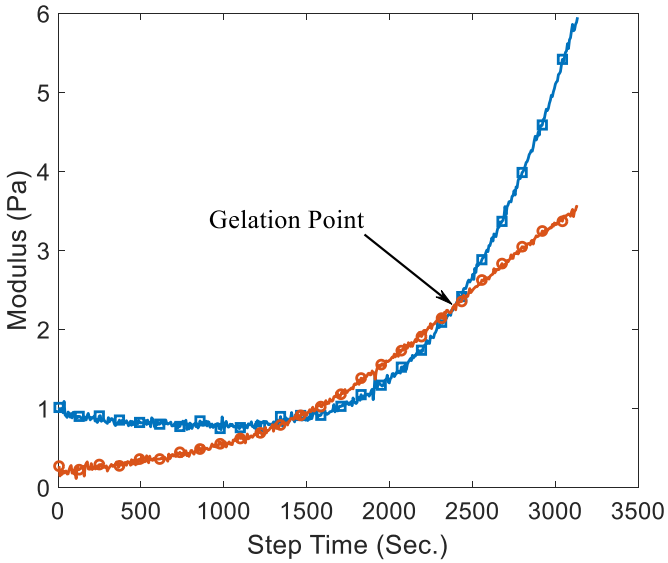

Fig. 3.7. "Gelation point for the control sample in time-sweep rheometry results (Circle: Loss modulus, Square: Storage Modulus)." (Reprinted with permission from ref [1]. Copyright 2019 Elsevier.)

3.3.2 Stiffness

"Frequency-sweep rheology tests were employed after hydrogel crosslinking to analyze the effects of COOH-CNTs and OH-CNTs on the storage modulus (Fig. 3.8-c, d). Regardless of the CNT type, the storage modulus highly depends on the CNT concentration, but not on the frequency. The maximum storage modulus for both types of CNTs belonged to the sample with 250 μg ml^{-1} CNT concentration. Increasing the CNT concentration to 750 μg ml^{-1} gradually decreased the storage modulus. In OH-CNTs hydrogels, 1000 μg ml^{-1} and 1250 μg ml^{-1} concentrations yielded a greater storage modulus in comparison with the 750 μg ml^{-1} sample.

A comparison between the values in Fig. 3.8 indicates that the storage modulus of the OH-CNTs samples is greater than that of the COOH-CNTs samples, and the gelation time of the OH-CNTs hydrogels is shorter than that of the COOH-CNTs groups. These differences are due to the unequal crosslinker concentrations used for the two groups of CNTs. Using a tilted tube test, it was found that the OH-CNTs hydrogels do not crosslink when 0.005%

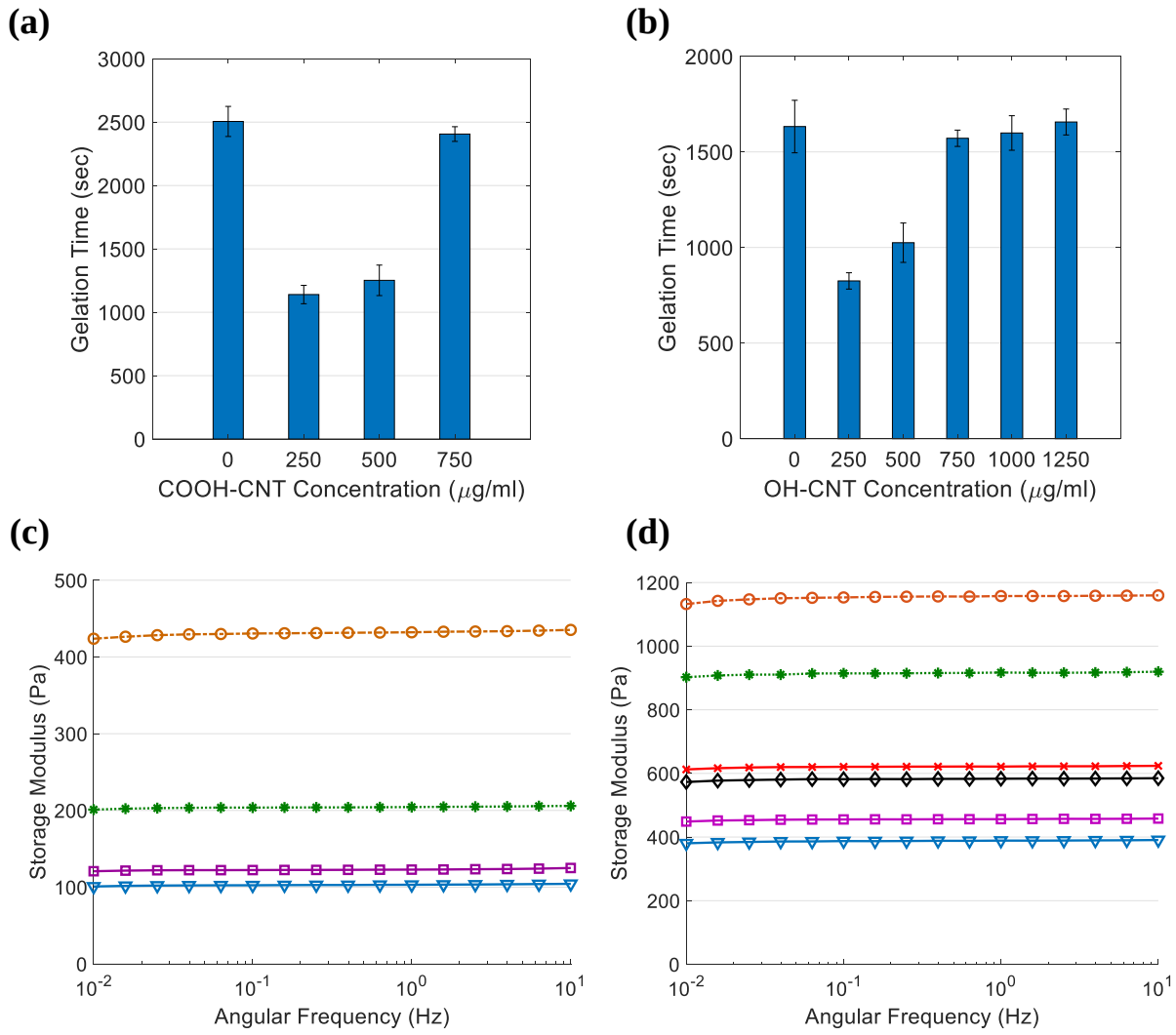

Fig. 3.8. Gelation time for the composite hydrogels as a function of CNT concentration for different types of CNTs; **(a)** COOH-CNTs, **(b)** OH-CNTs groups. The effect of CNT concentration on the storage modulus of composite hydrogels; **(c)** COOH-CNT groups **(d)** OH-CNT groups (Triangle: Control, Circle: CNT250, Asterisk: CNT500, Square: CNT750, Diamond: CNT1000, Cross: CNT1250). (Reprinted with permission from ref [1]. Copyright 2019 Elsevier.)

glyoxal is used. Therefore, the concentration of glyoxal used for OH-CNTs samples was increased to 0.00625%. Increasing the concentration of the crosslinker accelerated gelation

and increased stiffness. The necessity of using higher concentrations of the crosslinker for the OH-CNTs groups may cause cytotoxicity. For this reason, the biological experiments except for the cell viability studies were conducted using the COOH-CNTs groups only. Apart from the crosslinker concentration, the OH-CNTs samples followed the same trends as those of the COOH-CNTs hydrogels."

3.3.3 Stress relaxation

A constant shear stress was applied to samples of composite hydrogels to analyze the stress relaxation behavior of the different groups. "The time history of the shear stress recorded during the stress relaxation experiment is shown in Fig. 3.9. As expected, the stress level decayed over time due to the relaxation of the hydrogel network. The relaxation rate generally increased for higher concentrations of CNTs. The relaxation timescale (τ^*) was defined as the time required for the stress level to be relaxed to one-half of its initial value. Based on the definition of τ^*, the samples with a COOH-CNTs concentration of 750 μg ml^{-1} had a 15% lower relaxation time than the control samples, which were CNT-free. The results show that the relaxation time of the GC hydrogel can be slightly modulated by applying different concentrations of COOH-CNTs."

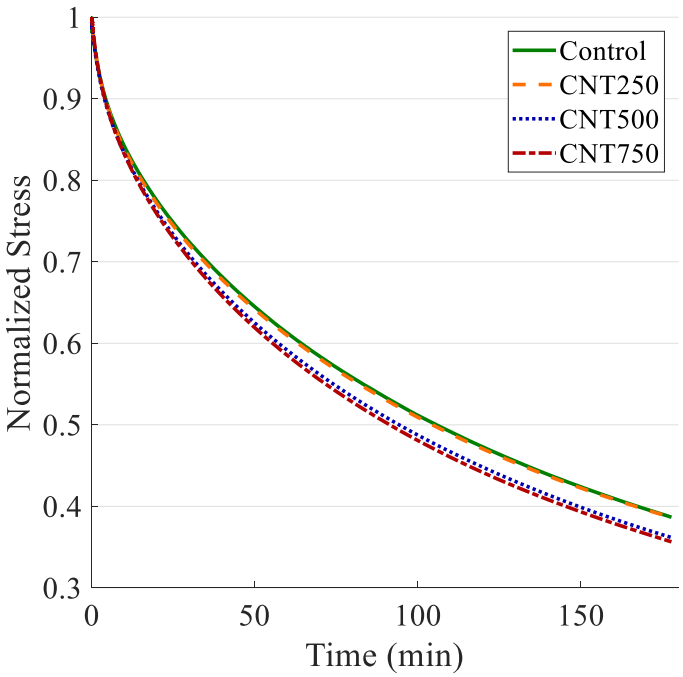

Fig. 3.9. "The decay of shear stress over time for the COOH-CNT hydrogel groups in stress relaxation experiment." (Adapted from ref [2] under the terms of the CC BY 4.0 license.)

3.4 Biological characterization

3.4.1 Cell viability

"Three parameters were found to significantly affect the biocompatibility of CNT-based hydrogels: i) the exposure time; ii) the CNT concentration; and iii) the functionalization type. Fig. 3.10-a shows the cell viability rate for different low-range COOH-CNTs concentrations over a period of one week. For the low concentration tests, all samples maintained a cell viability of over 90%. Since the COOH-CNTs low concentration groups did not show any cytotoxic effect, the concentration was increased 100-fold. It was then observed that the viability rates remarkably decreased when higher concentrations of CNT were incorporated, as shown in Fig. 3.10-b. For samples with concentrations of over 1000 μg ml^{-1}, the cell viability rate decreased to about 60%, which indicates the noticeable effect of the CNT concentration on the cytotoxicity. At this point, the upper limit for the feasible COOH-CNTs concentration was determined, and the results of the medium concentration experiment confirmed the maximum allowable amount of COOH-CNTs in the composite hydrogel."

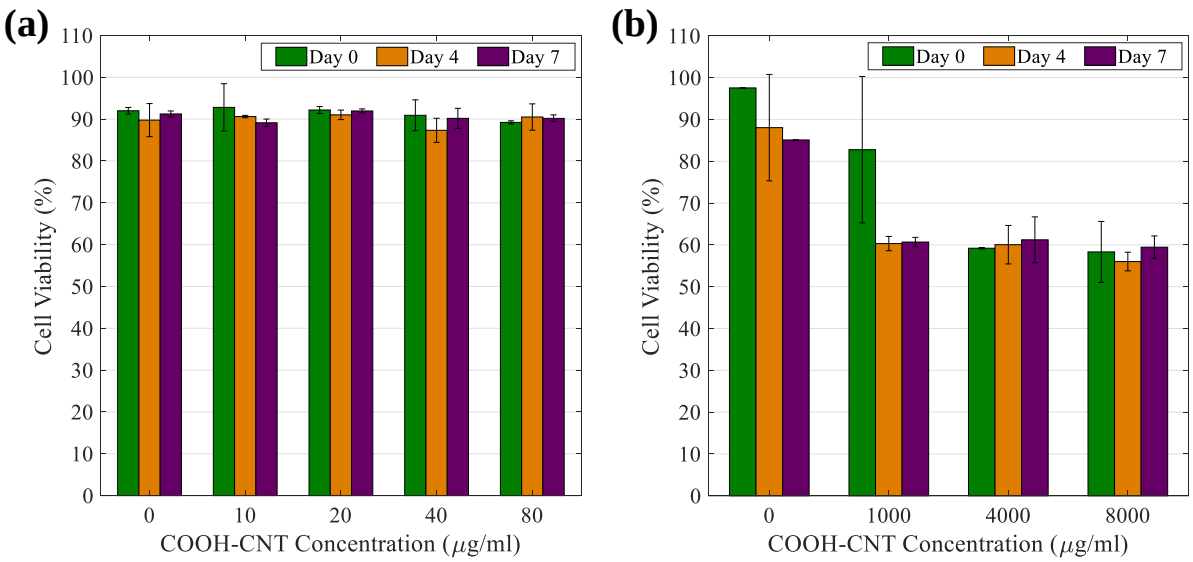

Fig. 3.10. "Cell viability for **(a)** low and **(b)** high concentrations of COOH-CNTs in the first week of exposure." (Reprinted with permission from ref [1]. Copyright 2019 Elsevier.)

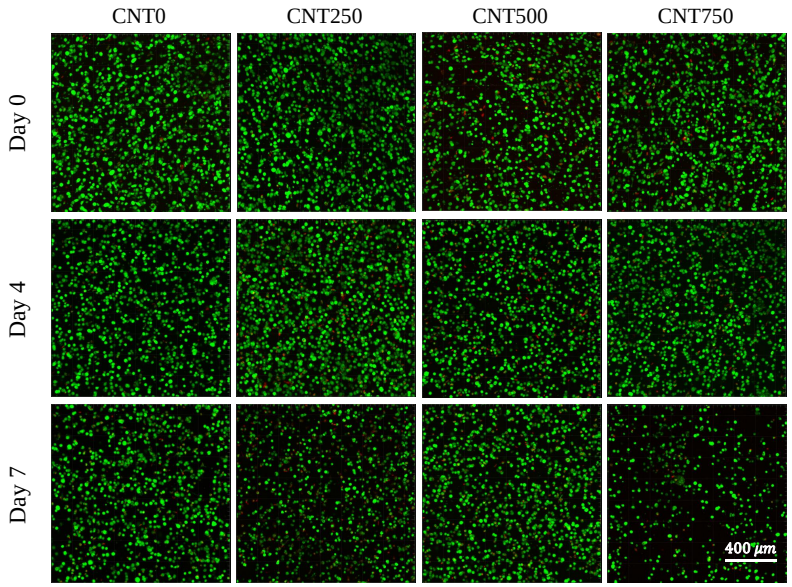

Fig. 3.11. "Representative CLSM images of HVFFs encapsulated in composite GC hydrogels containing medium concentrations of COOH-CNTs. The 3D images were used for determining the viability rate of the hydrogels (Green: live cells, Red: dead cells)." (Reprinted with permission from ref [1]. Copyright 2019 Elsevier.)

Fig. 3.11 shows confocal laser scanning microscopy (CLSM) images of the cell-encapsulated CNT-GC hydrogels with medium concentrations of COOH-CNTs. "In this range of concentration, the cell viability rate for all samples was similar to that for the control sample, as compared in Fig. 3.12-a. There is a clear relationship between cell viability rate, exposure time, and CNT concentration. The viability rate declines as the exposure time and the COOH-CNTs concentration increase. On day 7, a viability rate of 75%, which is considered as the threshold of viability, was obtained for the sample with a CNT concentration of 750 μg ml^{-1}. This point was deemed the maximum COOH-CNTs concentration in the GC hydrogel that can be used in 3D culture of HVFFs without any significant cytotoxicity.

To determine the effect of CNTs' functional group, OH-CNTs were also tested in cell viability experiments. The maximum allowable OH-CNTs concentration was found to be 1250 μg ml^{-1} (Fig. 3.12-b), which is greater than that of the COOH-CNTs samples. This observation proves that although their dispersion is more problematic, the level of biocompatibility for OH-CNTs is greater than that of the COOH-CNTs." However, the interference of the OH functional group with the crosslinkeing mechanism of the GC hydrogel (reaction between hydroxyl group of the OH-CNTs and the aldehyde in glyoxal) inhibited the possibility of utilizing OH-CNTs in the CNT-GC composite hydrogel. Furthermore, the cell viability rate of the OH-CNTs samples on day 0 was significantly lower than that of the

control sample, which confirmed that the addition of OH-CNTs to the GC hydrogel led to a short-term cytotoxicity.

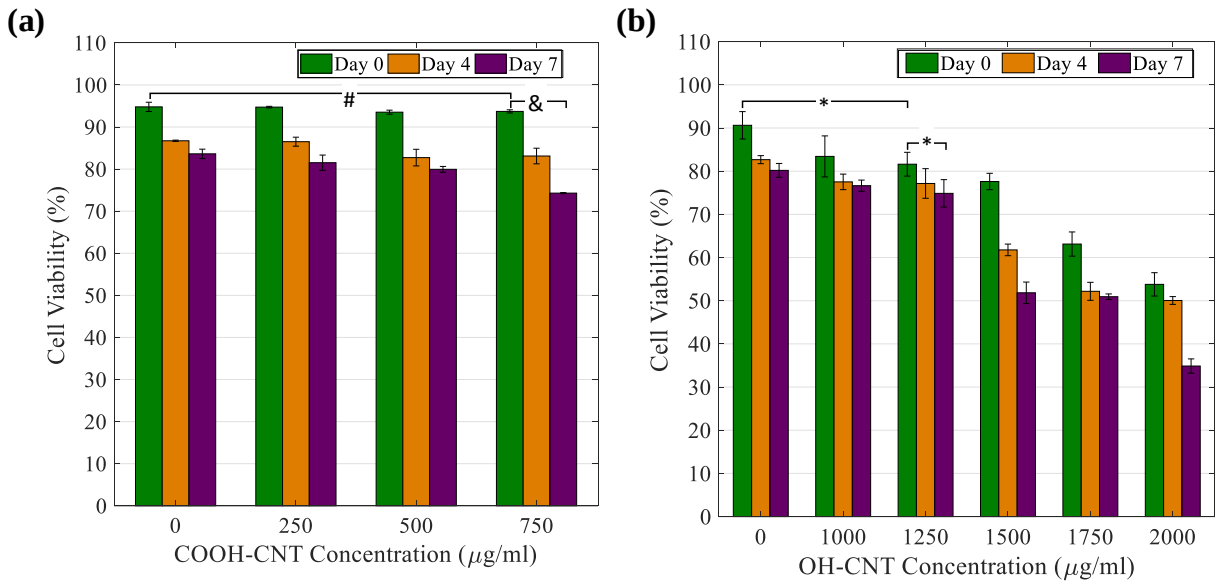

Fig. 3.12. "**(a)** Cell viability rate (i.e., ratio of live cells to total number of cells) for medium concentration COOH-CNTs, and **(b)** OH-CNTs groups. #p < 0.2 corresponds to an insignificant difference, &p $< 10^{-5}$, $*$p < 0.01." (Reprinted with permission from ref [1]. Copyright 2019 Elsevier.)

3.4.2 Cell recruitment

"A droplet of the hydrogel was placed in an uncoated eight-well and surrounded by the fibroblasts. Due to the cells' affinity to migrate toward regions with lower local cell-density [202], they move toward the hydrogel droplet, which has no cells in it. The cells can attach to the hydrogels' surface and in some cases penetrate it. The color-coded regions in Fig. 3.13-a show how the cells move towards the hydrogel. The average displacement of the fibroblasts over time, plotted in Fig. 3.13-b, shows that the CNT-GC composite hydrogels generally recruit the fibroblasts better than the pure GC hydrogel, i.e. the control sample. The average velocity and displacement of the cells toward the center of the hydrogel droplet was measured at t=14 h and plotted in Fig. 3.14-a, b, respectively. The velocity and displacement of the

cells are larger for the CNT250 hydrogel, thereby indicating more effective cell recruitment. For the control samples, both the velocity and the displacement have negative values, which shows that the hydrogel's pore size is not large enough for the cells to penetrate the hydrogel. The fibroblasts moved toward the CNT-free hydrogel until they reached its surface. Afterwards, hydrogel swelling dominated cell motion and moved them backwards with a negative velocity and displacement. Although this method can quantify cell recruitment, there are some drawbacks associated with it. For example, the hydrogel droplet geometry was not reproducible, and hydrogels swelling over the imaging period was not taken into account. These flaws prompted us to find a more accurate method to quantify cell kinematics."

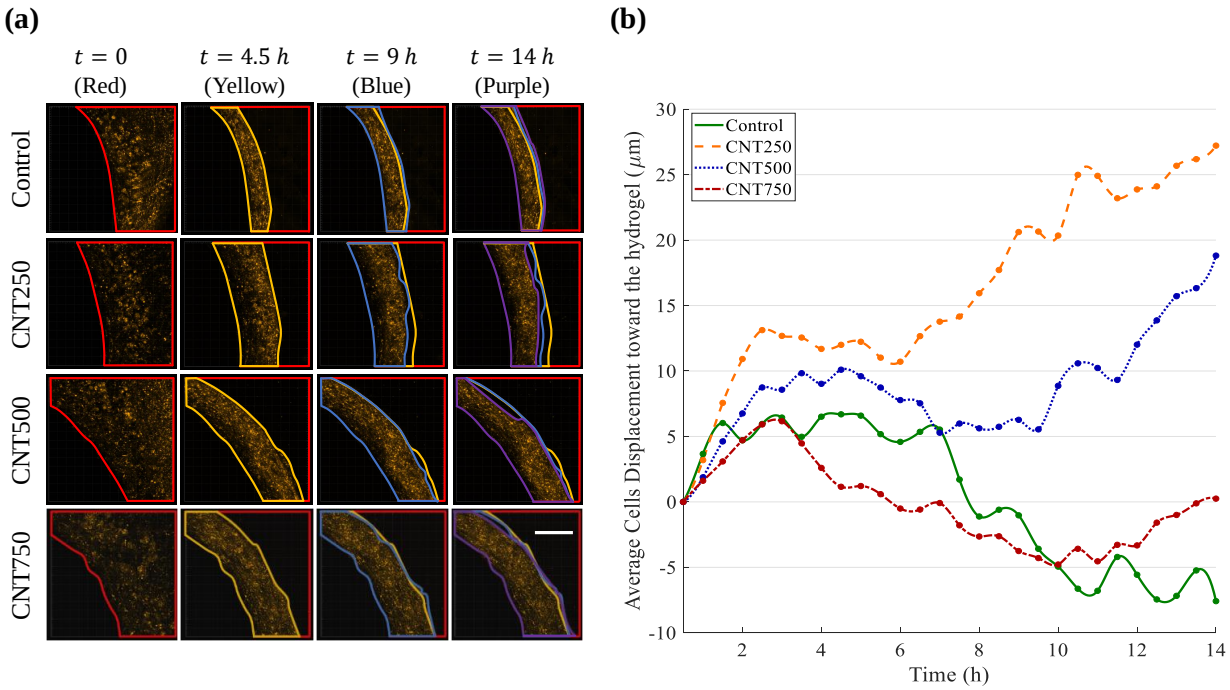

Fig. 3.13. "**(a)** Time-lapse images of the cells (stained in orange) surrounding one drop of hydrogel (left side of the mosaic images). The regions that are occupied by the cells are illustrated in color-coded frames: red, yellow, blue, and purple, chronologically. The scale bar is the same for all the images and is equal to 400 μm. **(b)** Cells' movement toward the hydrogel over time. A positive displacement means that the cells are moving toward the center of the hydrogel, and a negative value indicates that the hydrogel swelling dominates the cell displacement." (Adapted from ref [2] under the terms of the CC BY 4.0 license.)

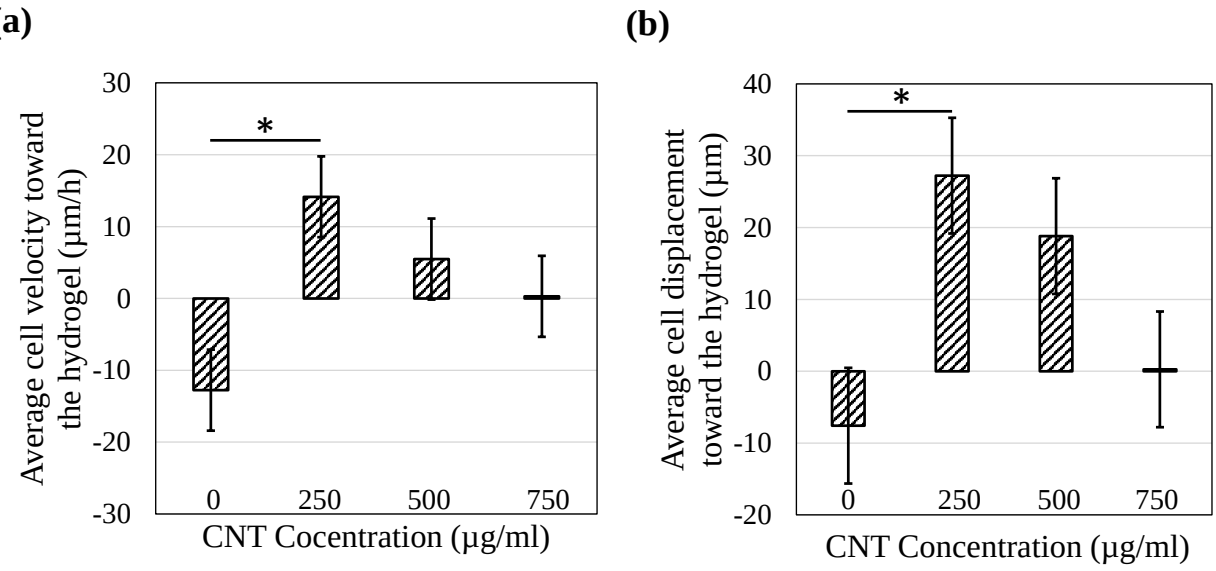

Fig. 3.14. "**(a)** Fibroblasts' average directional velocity at t = 14 h. **(b)** Fibroblasts' average directional displacement at t = 14 h. The cells surrounding CNT250 hydrogel were recruited more effectively. $^{*}p < 0.05$ corresponds to a significant difference." (Adapted from ref [2] under the terms of the CC BY 4.0 license.)

3.4.3 Cell migration

A chemoattractant-induced cell migration assay, previously depicted in Fig. 2.3, was designed to quantify the effect of CNTs on cell migration. "The hydrogel was covered by serum-free media to avoid dehydration during the assay. The 10% fetal bovine serum (FBS) solution beneath the porous membrane served as the chemoattractant agent. The chemoattractant gradient directed fibroblasts motion across the porous polycarbonate membrane. For all hydrogels, two samples were prepared by replacing Dulbecco's Modified Eagle Medium (DMEM) + 10% FBS with serum-free media to study the effect of chemoattractant. Two other samples were also studied using serum-free media in the bottom and DMEM + 10% FBS in the top of the cell-encapsulated hydrogel. The samples were prepared simultaneously in a 24-well companion plate, as shown in Fig. 3.15-a. The cell migration index was defined as the ratio of the number of cells migrated through the porous membrane and the total number of encapsulated cells. As a preliminary study, the migrated cells solution was observed

under a brightfield microscope (Olympus CKX41) to confirm that the cells migrated in the CNT-GC composite hydrogels. Flow cytometry was utilized to accurately count the number of migrated cells, as described in Section 3.4.4. The cell migration index obtained from the flow cytometry measurements is shown in Fig. 3.15-b. The highest rate of cell migration was for the CNT250 group. A higher concentration of CNT did not necessarily increase cell migration further. As expected, the cell migration index for samples without FBS is relatively smaller but follows the same trend with respect to the CNT concentration. In fact, FBS (i.e., cells' nutrient) acts as an activator by accelerating cell migration. For the samples with switched configuration of serum-free media and DMEM + 10% FBS, the cell migration index was negligible. This again highlights the role of the chemoattractant agent."

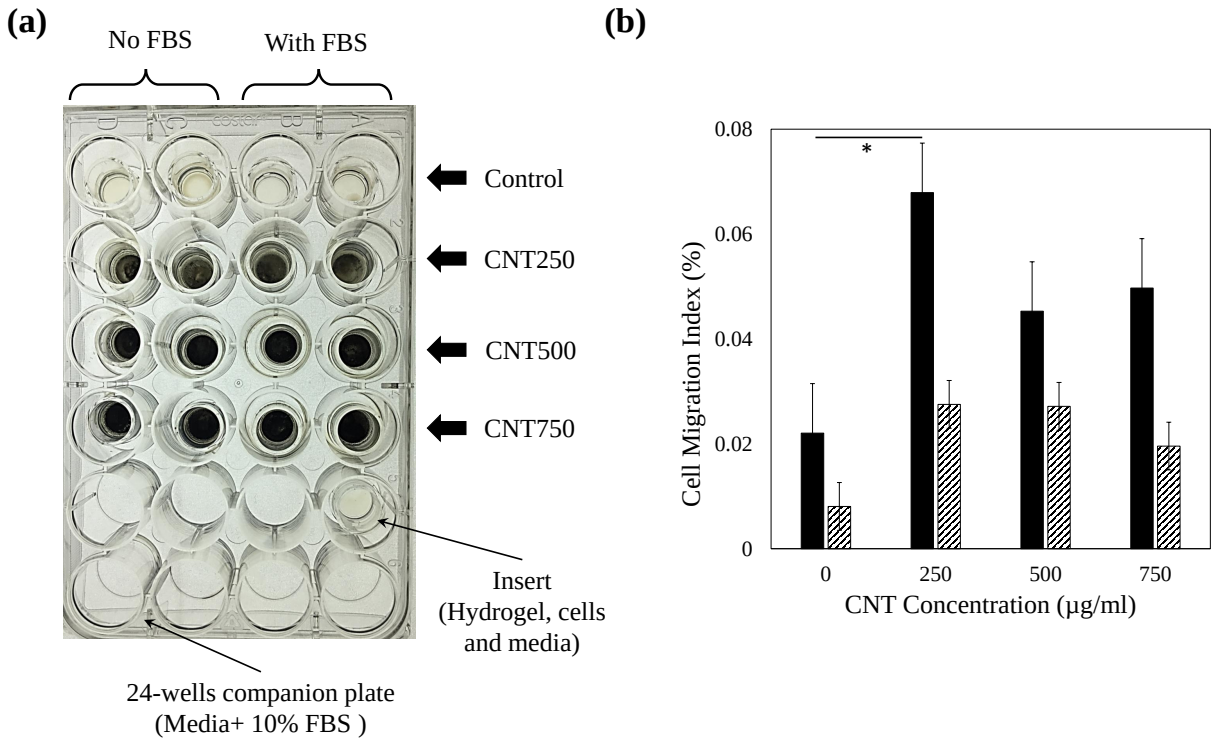

Fig. 3.15. "**(a)** Samples prepared in porous cell culture inserts and 24-well plate. To check the effect of FBS, one-half of the samples, denoted as No FBS, had no chemoattractant. **(b)** The average cell migration index for the samples with (solid pattern) and without (diagonal pattern) chemoattractant. *$p < 0.05$ corresponds to a significant difference." (Adapted from ref [2] under the terms of the CC BY 4.0 license.)

3.4.4 Flow cytometry

"Fig. 3.16 shows representative flow cytometric cell counting results for the samples with FBS in the side scattered area (SSC-A) vs. forward scattered area (FSC-A) graphs. For counting the migrated fibroblasts and the beads in FlowJo software, the single particles were isolated using the diagonal polygon gate in forward-scattered height (FSC-H) vs. FSC-A graph. The counting beads used in this study have a high SSC and a low FSC profile. The fibroblasts, however, have lower SSC and higher FSC signals due to their size and intracellular structure. Therefore, the fibroblasts and the counting beads can be clearly discriminated using a polygon and an ellipse gate, respectively, as in Fig. 3.16. It is evident that the number of migrated cells for the samples with CNT is significantly greater than that of the control sample."

3.4.5 Cell adhesion

"The representative images of the F-actin filaments and the nucleus of the encapsulated fibroblasts are shown in Fig. 3.17-a. The 3D CLSM images of cell adhesion samples were sliced as demonstrated in Fig. 3.17-b, to conduct further morphological analysis. Since the difference in cell morphology is not visually distinguishable, an image processing method was used. The morphology of the cells was quantified based on defining the extensibility ratio (ER) as

$$ER = \left| 1 - \left[\left(4\pi \frac{S}{p^2} \right) \times \left(\frac{L^{'}}{L^{''}} \right) \right] \right| , \tag{3.1}$$

where S is the surface area of each cell in the processed slice of the image, p stands for the perimeter of the cell, and $L^{'}$ and $L^{''}$ represent the length of the minor and the major axis of the ellipse that has the equal normalized second central moments the same as the cell, respectively. For a circular object, i.e. no adhesion at all, the ER value would be equal to 0. When the cells adhere to the hydrogel, the F-actin filaments become elongated, and the cells' shape changes to a less circular geometry, leading to an increased ER. The average value of ER for the cells was used to quantify cell adhesion in hydrogels. As shown in Fig. 3.17-c, the CNT250 samples have an average ER value higher than the other hydrogels, implying

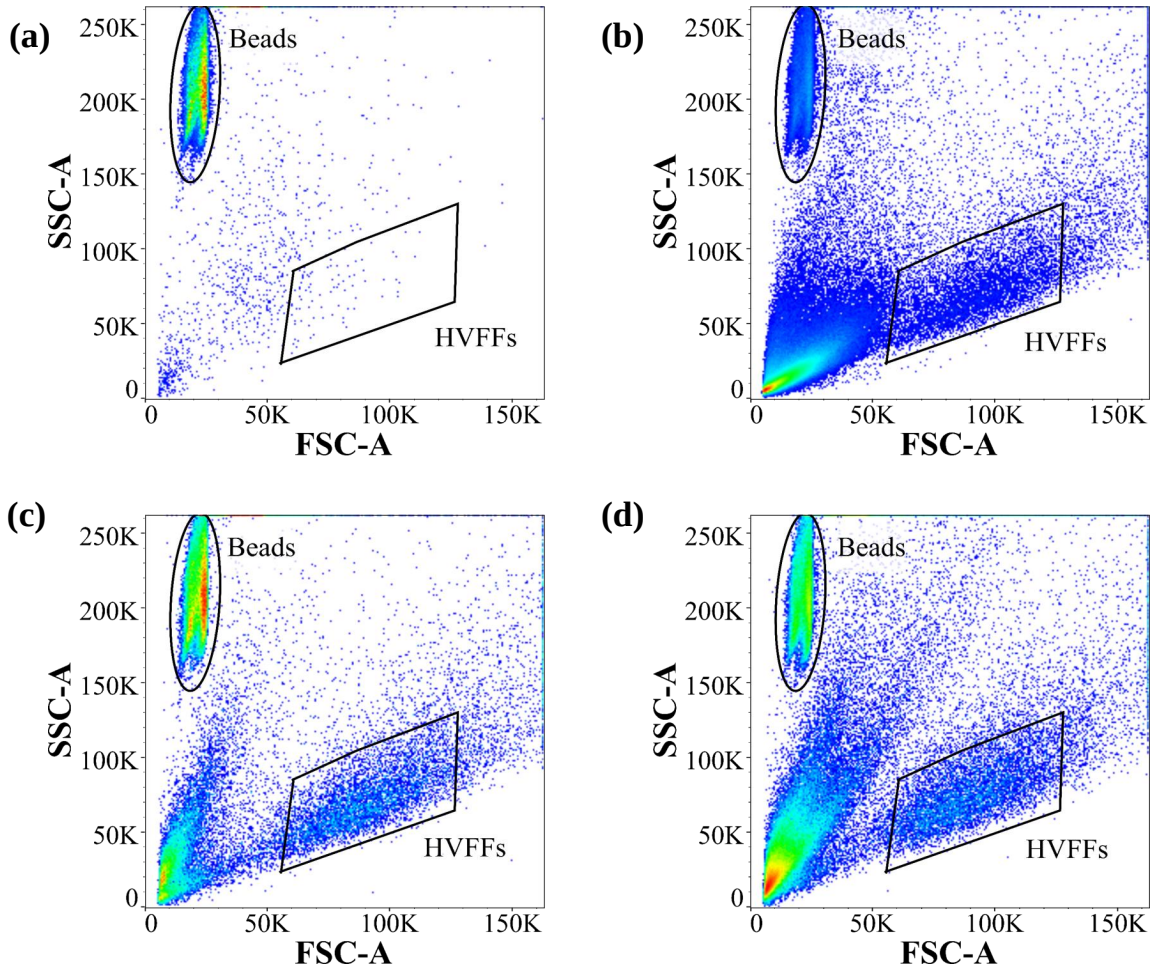

Fig. 3.16. "Discrimination of counting beads and migrated fibroblasts based on SSC-A and FSC-A signals in flow cytometric cell counting in the presence of the chemoattractant. A significant increase in the number of migrated cells in CNT composite hydrogels was observed. The events in the left bottom of the graphs are the debris in the cell solution. **(a)** Control, **(b)** CNT250, **(c)** CNT500, and **(d)** CNT750." (Adapted from ref [2] under the terms of the CC BY 4.0 license.)

better adhesion. This was not visually detectable in the CLSM images but became obvious by processing them and calculating the ER for the samples. In Fig. 3.18, a representative slice of the CLSM image of the cells' F-actin filaments is shown along with a step-by-step image processing procedure."

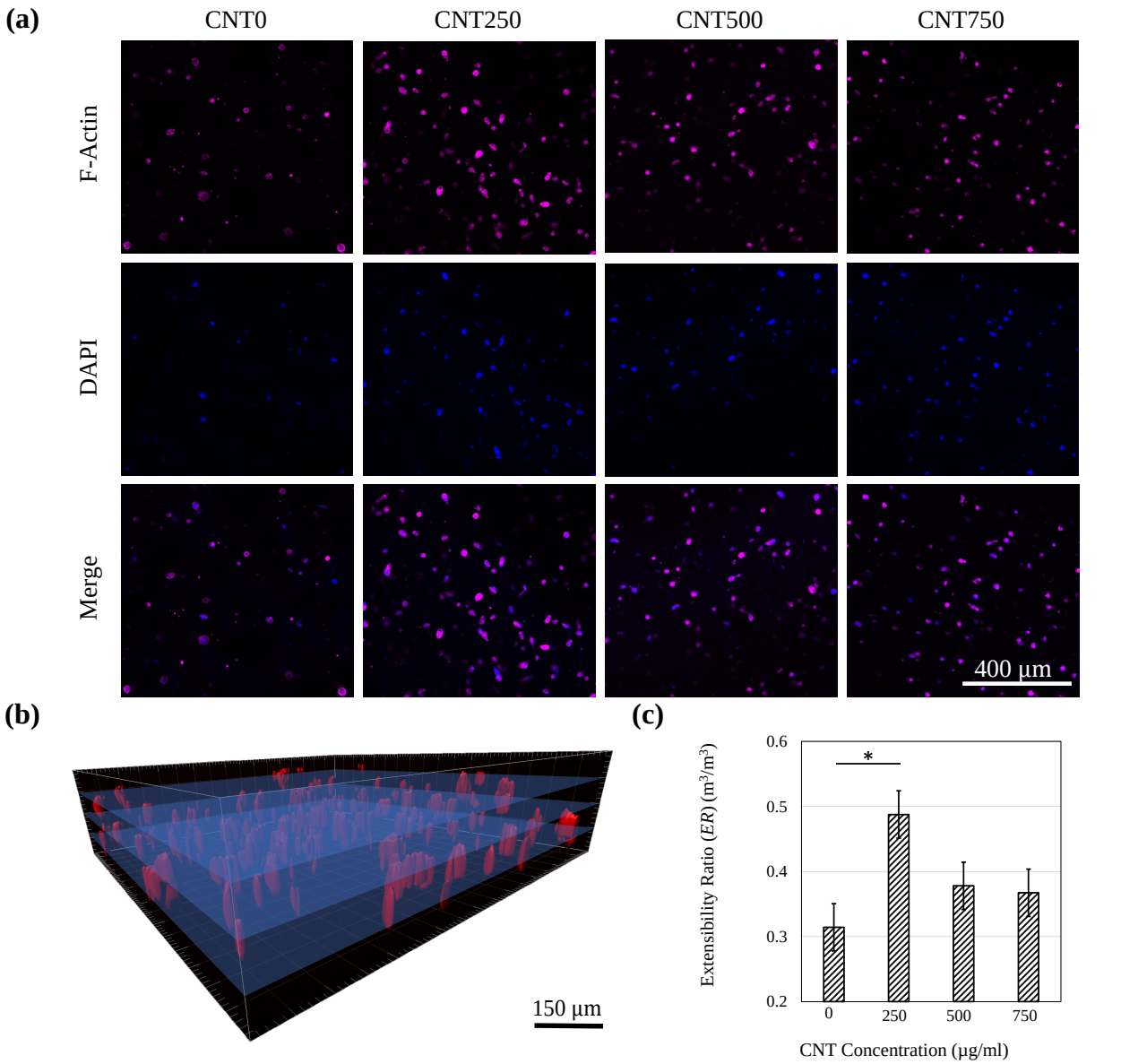

Fig. 3.17. "**(a)** Representative CLSM images of the F-actin filaments stained with Alexa 633-phalloidin, and the nucleus of the encapsulated fibroblasts stained with DAPI. **(b)** Illustration of image segmentation. **(c)** The ER value calculated for different groups of the hydrogels acquired from segmented image analysis. $^{*}p < 0.05$ corresponds to a significant difference." (Adapted from ref [2] under the terms of the CC BY 4.0 license.)

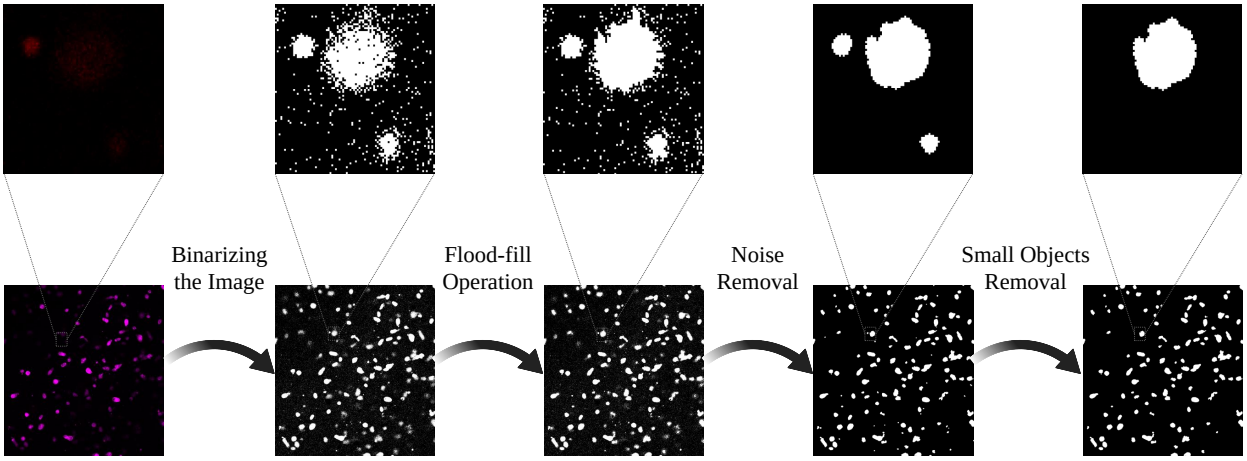

Fig. 3.18. "Demonstration of the step-by-step image processing used to quantify cell morphology and adhesion. The first step was converting the CLSM images to binary images. The black pixels which were surrounded by white pixels were changed to white pixels so that a clear and homogeneous image of the cell was obtained. After removing noise, the small objects, which consisted of less than 100 pixels, were omitted." (Adapted from ref [2] under the terms of the CC BY 4.0 license.)

3.5 Discussion

"Higher concentrations of COOH-CNTs and OH-CNTs introduce more acidic and basic groups in the hydrogel, respectively. This effect changes the pH of the hydrogel, which can influence cell viability [203]. It is generally accepted that the cells maximum growth rate occurs at pH $7.4 - 7.5$, which is the physiological pH level [204]. The pH of the control samples (without CNT) was measured to be $7.2 - 7.4$. When OH-CNTs were added to the hydrogel, the OH functional groups caused the pH to slightly increase towards the physiological pH level. However, acidic functional groups in COOH-CNTs decrease the pH, moving it away from the physiological range. Therefore, the maximum allowable CNT concentration for OH-CNTs hydrogels is greater than that for the COOH-CNTs samples.

It was found that the addition of functionalized CNTs to GC hydrogel has two competing effects. Firstly, the addition of CNTs increased the storage modulus of the composite hydrogel, since the stiffness of CNTs is much greater than that of the matrix. Conversely, the abundance of functional groups in the composite hydrogel impeded fast and complete crosslinking of

glycol chitosan polymer chains when the CNT concentration increased. Slow and incomplete crosslinking of the hydrogel network resulted in an increase in gelation time and a decrease in storage modulus. Therefore, greater CNT concentrations do not necessarily cause an increase in the storage modulus.

For OH-CNTs concentrations of up to 750 μg ml^{-1}, the hydroxyl groups play the role of limiting reactant in chemical crosslinking reaction. Thus, in this range, the gelation time depends on the concentration of functional groups. When higher concentrations are introduced, e.g. 1000 μg ml^{-1} and 1250 μg ml^{-1}, the functional groups are the excess reactants, and the gelation time does not change with increasing the OH-CNTs concentration. However, the storage modulus of the 1000 μg ml^{-1} sample is greater than that of 750 μg ml^{-1} sample, which is due to the higher concentration of stiff CNTs.

The findings in the present thesis show that using COOH-CNTs in GC hydrogel enhanced the swelling ratio and the porosity of the hydrogel. Since the cationization of amine groups is facilitated in an acidic environment [205], samples with higher concentrations of COOH-CNTs absorb more PBS, and thus, have a greater swelling ratio. The greater swelling ratio resulted in a larger average pore size, which can promote cell migration. The addition of OH-CNTs did not alter the absorbance capacity of the hydrogels, which is due to the higher concentration of crosslinker [206]. Therefore, the OH-CNTs neither affected the swelling ratio nor the average pore size of the hydrogel.

Other types of fibers such as collagen type I and III have been used in composite hydrogels [123]. Table 3.1 compares the impact of adding different fibers to GC hydrogel. The addition of collagen and CNT fibers resulted in similar trends in pore size change. The swelling ratio did not change when collagen fibers were added. The storage modulus and gelation time of CNT-based composite hydrogels may be smaller or greater based on the concentration of fibers. This may allow the fine tuning of the storage modulus through the addition of the CNTs."

"The cell recruitment and the 3D chemoattractant-induced cell migration results confirmed that the presence of CNT in the GC hydrogel enhances fibroblasts' migration in the hydrogel network. The average cell migration index is small for all the study groups. This is not specific to the CNT-GC hydrogel, as it has been previously reported that in normal in vitro conditions only a few percents of fibroblasts migrate through chemotactic mechanisms [193, 207]. The cell

Table 3.1. "The effects of adding different fibers to GC hydrogel." (Adapted from ref [2] under the terms of the CC BY 4.0 license.)

	COOH-CNT	**OH-CNT**	**Collagen I and III** [123]
Pore size	Increase	Constant	Increase
Swelling ratio	Increase	Constant	Constant
Storage modulus	Concentration dependent	Concentration dependent	Increase
Gelation time	Concentration dependent	Concentration dependent	Decrease

concentration that was herein used in the chemoattractant-induced cell migration experiment was less than 7 million cells per ml, which is drastically lower than that of a native vocal fold tissue (66 300 million cells per ml) [208, 209]. Higher cell concentration is therefore needed to obtain near-native conditions. The difference between cell migration indices for the CNT-GC hydrogels and the pure GC hydrogel, i.e. the control sample, was, however, statistically significant. The CNT-free GC hydrogel was covalently crosslinked by glyoxal. The addition of COOH-CNTs resulted in a higher concentration of COOH groups in the hydrogel solution. The abundant COOH groups impeded a complete covalent crosslinking in CNT750 and CNT500. This phenomenon yielded more floating CNTs within the hydrogels network, which further led to fewer static adhesion sites for the cells in CNT500 and CNT750 samples. However, the CNTs that were firmly positioned in CNT250 hydrogel network were potential focal adhesion sites for the encapsulated fibroblasts. As elaborated earlier in this section, the gelation mechanism is faster and more complete in CNT250 samples. The cells, therefore, have more focal adhesion sites for anchoring and migrating. Although the cells cannot fully express their spreading capability in 3D environment [124], the trend of changes in the ER with respect to the CNT concentration confirmed that the fibroblasts have more affinity to adhere to CNT250 samples. As a result, cell adhesion deems to be a dominant parameter in cell migration rate, as previously has been reported for two-dimensional (2D) environments [210].

In addition to cell adhesion and gelation time, other characteristics of the hydrogel may affect the cell migration rate [211, 212]. The maximum cell migration occurred in CNT250, while the porosity of CNT750 is the greatest. This reveals that although porosity is important for cell recruitment and migration, it does not necessarily play the most important role. Other parameters including, stress relaxation time, and pH can be also influential in cell migration rate within a 3D scaffold. The insignificant difference in biodegradation ratios on day 7 implies that the higher number of migrated cells in CNT-GC hydrogels is not due to faster degradation of the scaffold. This also addresses concerns about the negative effect of CNTs on the biodegradability of hydrogels. The degradation of CNTs, themselves, has been previously studied [213]. It has been shown that CNTs can be enzymatically degraded through shortening and unzipping mechanisms using horseradish peroxidase. As a result, the CNT-GC composite hydrogel is deemed be biodegradable in the human body. However, in-vivo experiments should be designed and conducted to clearly address the foreign body reaction.

Increasing the CNT concentration yielded a lower relaxation time. This can be explained by the fact that the concentration of ionic crosslinks in CNT-GC hydrogel is proportional to the COOH-CNTs concentration, and the increased ionic crosslinks reduce relaxation time. This trend is in a good agreement with previous studies which compared ionically crosslinked with covalently crosslinked hydrogels [214]. Although hydrogels with lower stress relaxation are believed to provide a better substrate for the cells to adhere [126], cell migration is not necessarily enhanced in hydrogels with faster relaxation. In fact, the addition of COOH-CNTs has different effects on cell migration and stress relaxation of the GC hydrogel.

Based on the results presented in this chapter, two sets of trends were observed for the properties of the CNT-GC composite hydrogels when COOH-CNTs were employed. The swelling ratio, porosity, cell viability, and stress relaxation change proportional to the COOH-CNT concentration. The gelation time, storage modulus, and cell migration, however, have a local extremum value at the COOH-CNTs concentration of 250 μg ml^{-1}."

CHAPTER 4

Cryobioprinting

This chapter is dedicated to presenting and discussing the cryobioprinting results. The modifications applied to a conventional bioprinting apparatus were described and the temperature control accuracy of a cryobioprinting stage was illustrated. Printing quality and fidelity of the cryobioprinted products made of gelatin methacryloyl (GelMA) were quantitatively studied through measuring the filaments' diameter for different printing parameters. Cell viability experiments for designing the cryoprotective bioinks are described. Seven different cell types were used to show the performance and flexibility of the cryobioprinting method for fabricating versatile cell-laden storable implants. Furthermore, cell differentiation and angiogenesis assays were employed to check the performance of the fabricated products in different conditions. The findings in this chapter shed light on the efficacy of the novel cryobioprinting method in biofabricating artificial tissues for future clinical applications.

4.1 Cryobioprinting design and characteristics

4.1.1 Freezing plate

A thermoelectric cooler, which is a solid-state heat pump and works based on the Peltier effect [215, 216], was designed and fabricated to maintain tightly controlled low temperatures on the substrate surface, as previously depicted in Fig. 2.6. This adjustable device transfers the heat from the printing stage, generating a controllable temperature drop. The freezing

plate temperature was adjusted via changing the input voltage or current, as shown in Tables 4.1 and 4.2. The two tables also show that the effect of environmental temperature on the freezing plate's temperature was negligible. Upon extrusion from the bioprinter nozzle and contact with the freezing plate, the bioink rapidly freezes in situ and forms a stable structure.

Table 4.1. Temperature control of the freezing plate at room temperature.

Voltage (V)	**Current (A)**	**Environment temperature (°C)**	**Cooling water temperature (°C)**	**Freezing plate temperature (°C)**
0	0	23.0	1.0	11.0
2.00	0.47	23.0	1.0	-4.5
4.00	0.96	23.0	1.0	-12.2
6.00	1.48	23.0	1.0	-17.5
8.00	1.98	23.0	1.0	-22.3
10.00	2.49	23.0	1.0	-25.0
12.00	3.01	23.0	1.0	-27.2

Table 4.2. Temperature control of the freezing plate in the cold room.

Voltage (V)	**Current (A)**	**Environment temperature (°C)**	**Cooling water temperature (°C)**	**Freezing plate temperature (°C)**
0	0	5.0	1.0	4.0
2.00	0.47	5.0	1.0	-6.0
4.00	0.97	5.0	1.0	-12.7
6.00	1.49	5.0	1.0	-19.2
8.00	2.03	5.0	1.0	-24.9
10.00	2.55	5.0	1.0	-27.8
12.00	3.04	5.0	1.0	-29.5

4.1.2 Printability and fidelity

Printability of potential cryoprotective bioinks with different concentrations of dimethylsulfoxide (DMSO), as the cryoprotective agent (CPA), in GelMA was evaluated. The effects of parameters such as the pressure, the printhead moving speed, and the nozzle size were examined by cryobioprinting a grid structure using 5% (w/v) GelMA containing different

DMSO concentrations. We used a 27G nozzle for cryobioprinting jobs since it generally yielded a better printing resolution than a 30G nozzle (Figs. 4.1 and 4.2). A lower printhead moving speed improved spatial resolution within the range of speed and pressure values investigated (quantitatively analyzed in Fig. 4.3). As expected, increased pressure while keeping printhead speed constant at 10 mm s^{-1}, caused a considerable enlargement in the filament diameter.

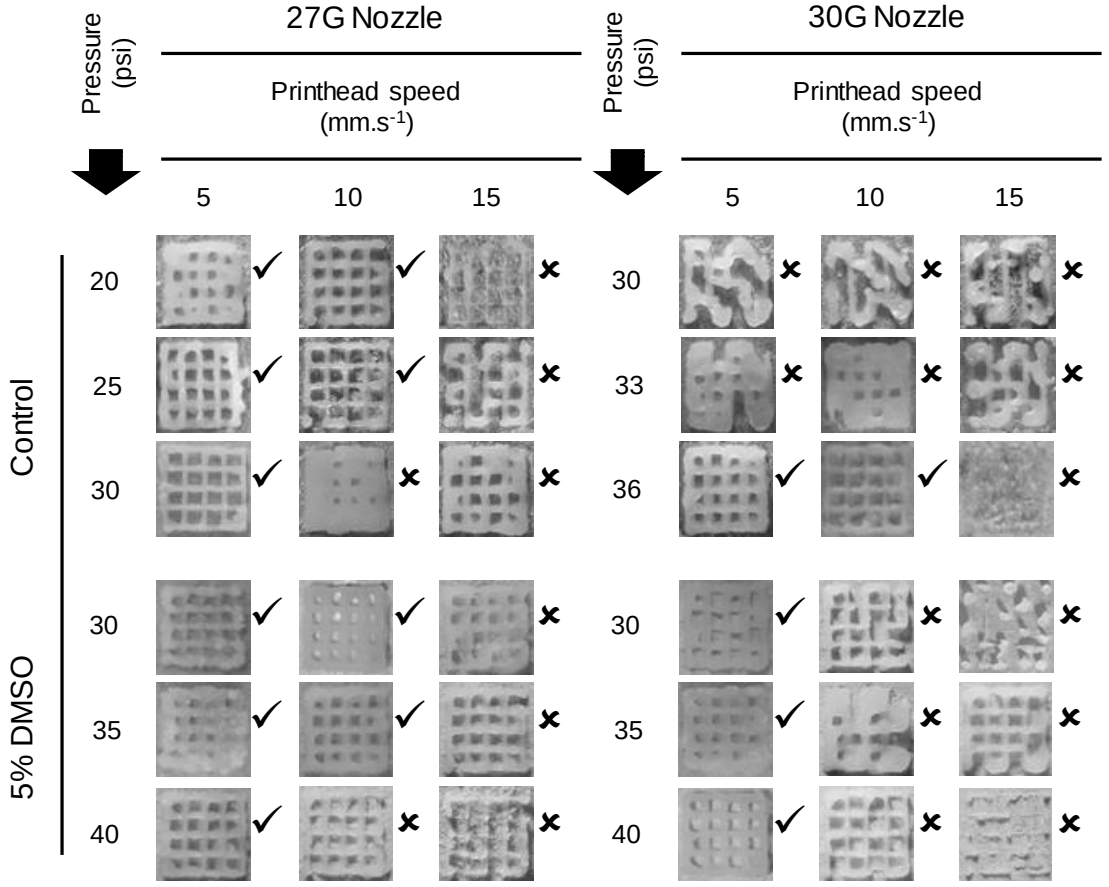

Fig. 4.1. Effects of nozzle size, pressure, and printhead moving speed on the printability of the GelMA bioink with and without DMSO by comparing cryobioprinted 8 × 8-mm^2 grids. The check marks denote that the cryobioprinted patterns were visually acceptable, and the cross signs represent a poor/unsuccessful cryobioprinting job. The addition of DMSO, as the CPA, had minimal effect on the printability of GelMA.

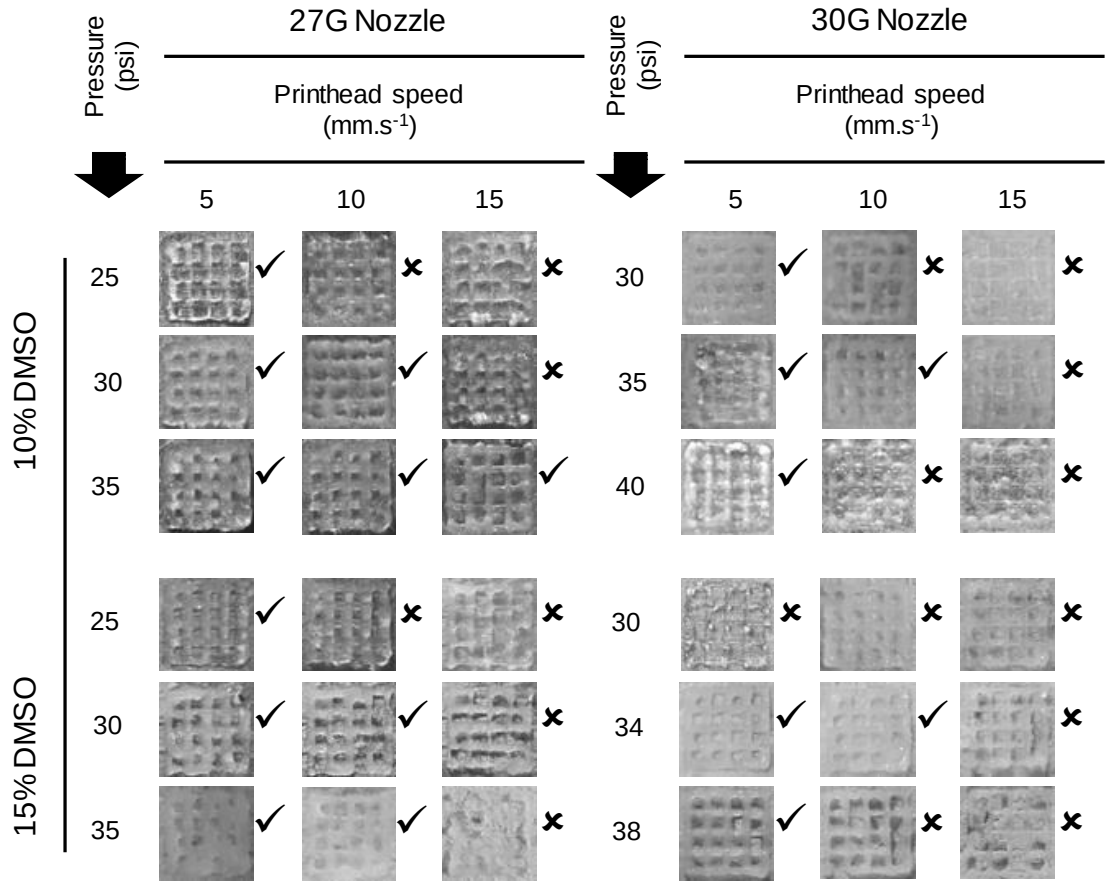

Fig. 4.2. Effects of nozzle size, pressure, and printhead moving speed on the printability of the cryoprotective GelMA bioink with higher concentrations of DMSO. The addition of DMSO, as the CPA, had minimal effect on the printability of GelMA.

The cryobioprinted structures were either immediately crosslinked or cryopreserved in a liquid nitrogen tank for on-demand use. The ultraviolet (UV) exposure time needed for crosslinking a 4-layer, 8×8-mm^2 GelMA grid pattern with different DMSO concentrations was studied. The samples that were not exposed to UV fully dissolved in phosphate-buffered saline (PBS) after shaking overnight. As shown in Fig. 4.4, a 10-s UV exposure resulted in a partially crosslinked sample, which did not maintain its integrity after shaking. Samples that underwent more prolonged UV exposure exhibited an acceptable fidelity, regardless of the DMSO concentration. The minimum essential UV exposure time, i.e., 20 s, was subsequently used for

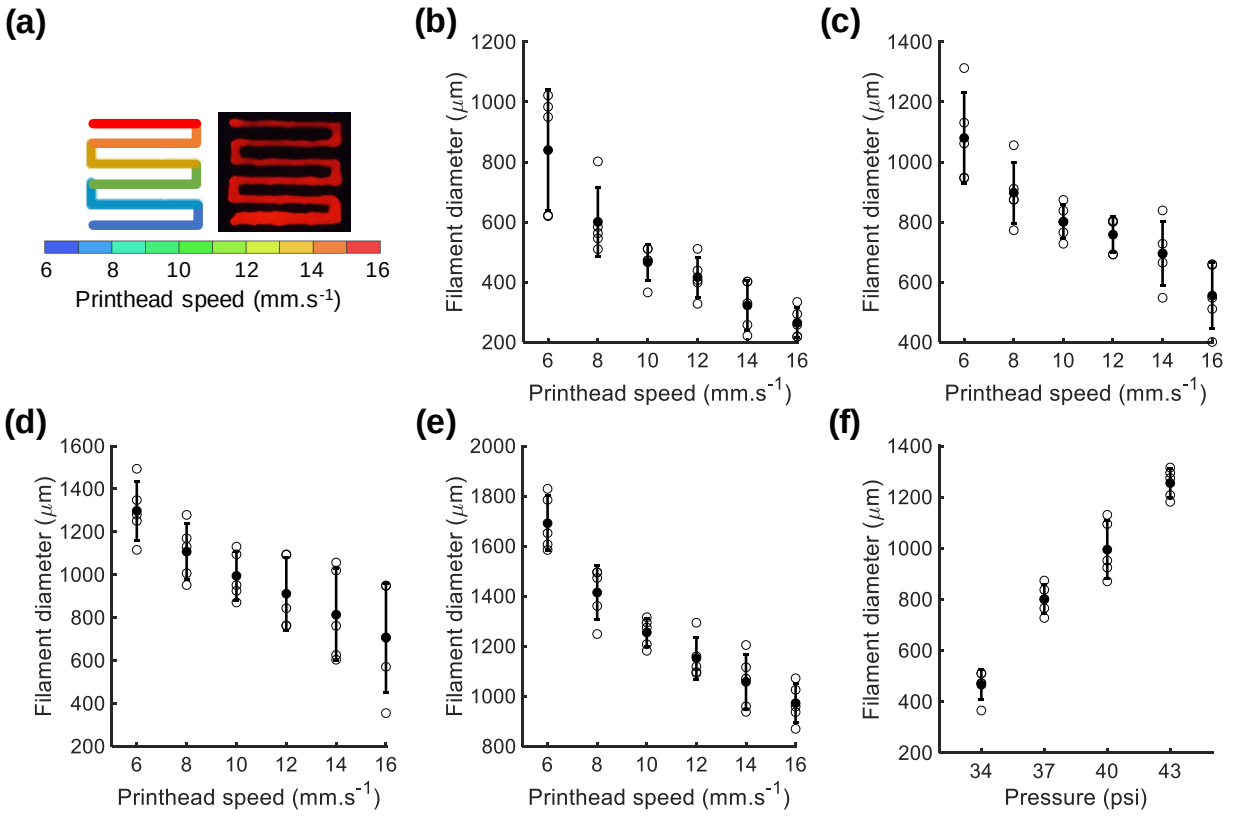

Fig. 4.3. Effects of printhead moving speed and pressure on filament diameter. **(a)** Bioprinting of a continuous filament using a 27G nozzle with different moving speeds for parametrically studying the effect of pressure (P) and speed (V) on the filament diameter. **(b)** P=235 kPa. **(c)** P=255 kPa. **(d)** P=275 kPa. **(e)** P=295 kPa. **(f)** V=10 mm s^{-1}. n = 5.

crosslinking the cell-laden grid structures without compromising cell viability. An increased exposure time was accordingly utilized for larger samples. Representative cryobioprinted structures from simple two-dimensional (2D) patterns to sophisticated three-dimensional (3D) structures were successfully created from both GelMA- and uncrosslinked gelatin-based bioinks (Fig. 4.5). Multi-material 2D and 3D constructs were subsequently fabricated from the bioink based on a mixture of GelMA and gelatin, as shown in Fig. 4.5-m to r. Remarkably, freeform constructs were successfully created using 5% (w/v) GelMA/gelatin/GelMA+gelatin as the base bioinks (Fig. 4.5-p to r). Fabricating freeform constructs is complicated when other extrusion bioprinting methods are employed.

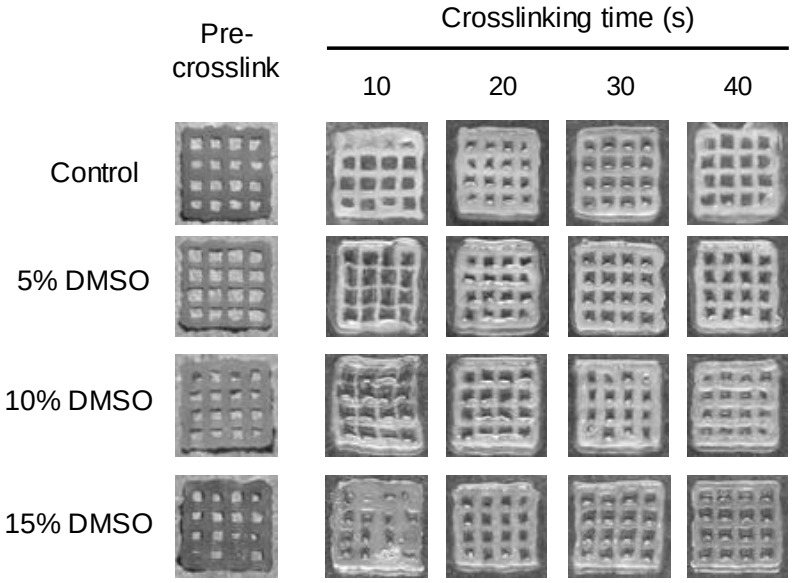

Fig. 4.4. The effect of UV exposure time on the fidelity of the cryobioprinted 8 × 8-mm^2 grid structures. The samples with 10 s of UV crosslinking were not fully crosslinked as the exposure time was not adequate.

4.1.3 Heat transfer simulation

The layer-by-layer cryobioprinting of a grid structure was modeled in COMSOL Multiphysic to understand the mechanism of heat transfer during the process. Fig. 4.6-a shows the simulation of heat transfer in the first layer while it is being cryobioprinted. Since the first layer (15 °C) directly contacts the freezing plate (-15 °C), the heat-transfer from the bioink to the freezing plate occurs instantaneously. Once the bioink contacts the freezing plate, the frozen region expands through the deposited material until the entire layer is frozen. The measured contours of the frozen bioink region perfectly matched that of the simulated model (Fig. 4.6-a-iv), indicating a good agreement between the simulation and the experiment. The freezing regime in the second layer is slower since the entire layer is not touching the underlying frozen layer, as shown in Fig. 4.6-b.

Temperature change through the first layer's filament thickness was plotted for different time steps to analyze the cryobioprinting procedure quantitatively (Fig. 4.6-c). At t=0, the

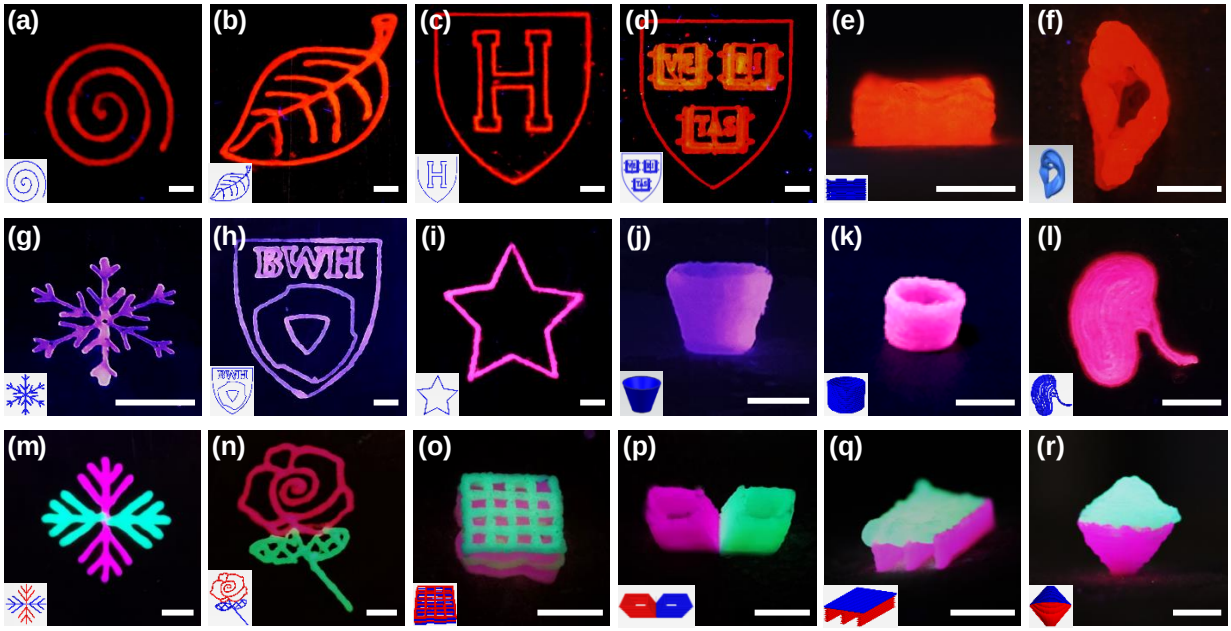

Fig. 4.5. Sample cryobioprinted 2D patterns, 3D structures, and freeform multi-material models made of **(a)** to **(f)** GelMA, **(g)** to **(l)** gelatin, and **(m)** to **(r)** GelMA+gelatin. Scale bars: 5 mm.

first layer's bottom surface is exposed to the freezing plate temperature, while the top of the layer remains at 15 °C. Since the dominant mechanism of heat transfer through the thickness is conduction and obeys Fourier's law, the temperature through the thickness changes linearly with the distance under the constant temperature gradient. At t=0.09 s, the whole bioink is frozen, and the top surface temperature reaches approximately 0 °C. This trend continues until the entire simulated section reaches an isothermal steady state at t=0.45 s. As shown in Fig. 4.6-d, the average surface temperatures of the layers are compared for three different freezing plate temperatures (T_p). For T_p = -15 °C, the top surface temperature of the second layer reaches 0 °C after 1.7 s, which corresponds to the freezing point of the bioink. Increasing T_p to -10 °C and -5 °C results in a slower freezing regime in the second layer, while the rapid temperature change in the first layer is not remarkably affected. As expected, the time needed to completely freeze the second layer is longer than that of the first layer for all three T_p values.

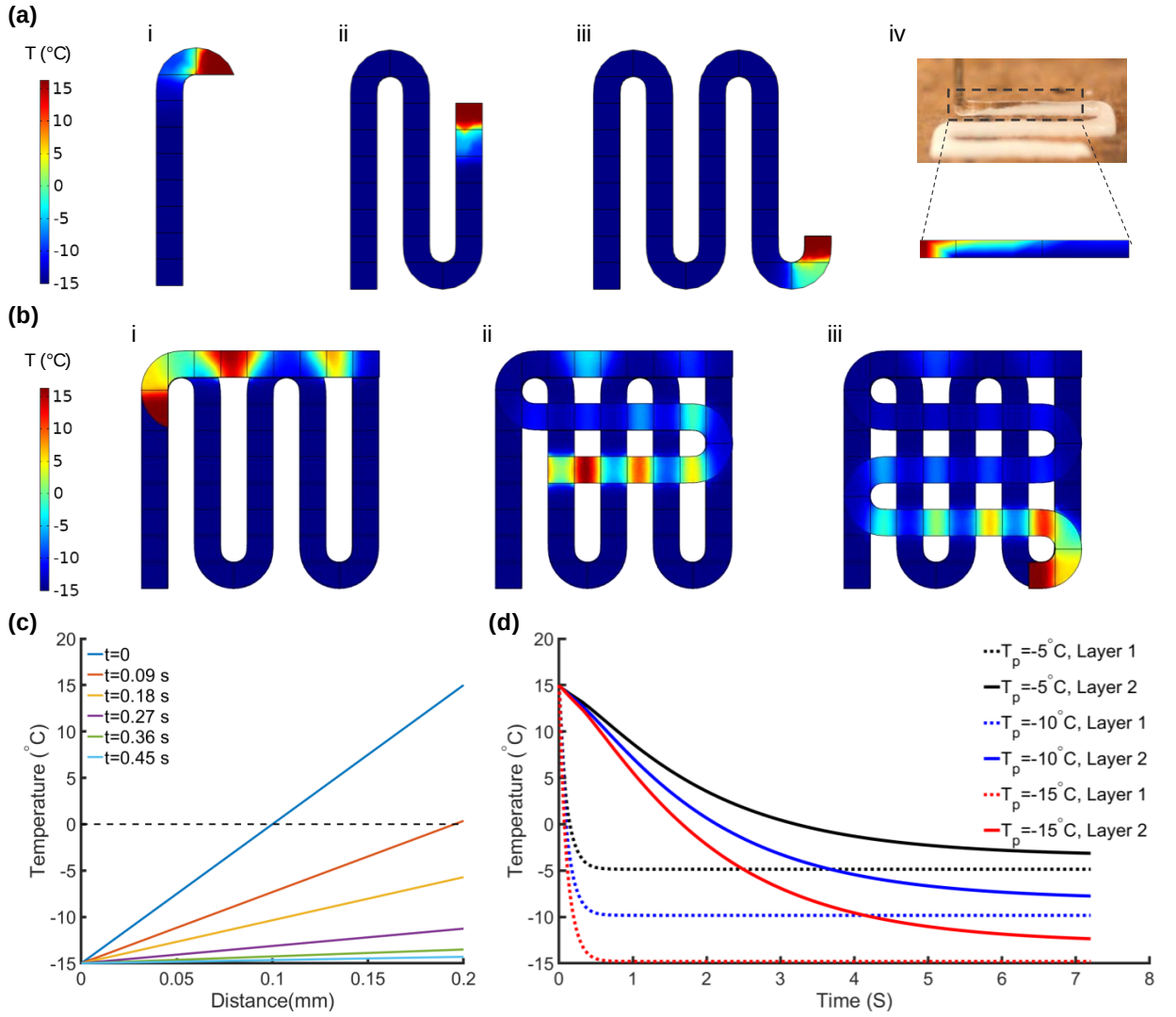

Fig. 4.6. Simulation results for the fabrication of a two-layer grid structure. **(a)** Temperature gradient in the first layer during cryobioprinting. The initial temperature of the bioink was set to 15 °C, and the freezing plate was simulated as a constant -15 °C surface. Panels **(i)** to **(iii)** demonstrate the progress of the cryobioprinting, and panel **(iv)** exhibits the freezing frontier lines in the experiment and the simulation. **(b)** Temperature gradient in the second layer of the grid structure. The regions that were in contact with the first layer froze faster. **(c)** Temperature changes through the thickness of the first layer during cryobioprinting. **(d)** Comparing the average temperature over the freezing period of first and second layers for different values of T_p.

4.2 Cryoprotective bioink design

4.2.1 Ice crystal-formation

One critical factor that affects cell viability during cryopreservation is the formation of ice crystals [217]. The spicular ice crystals can damage the cell membrane, resulting in lower cell viability. Time-lapse images of the ice crystal-formation in GelMA hydrogel groups with different CPA concentrations are shown in Fig. 4.7. The addition of CPAs noticeably affected the shape of ice crystals. In the control sample (without DMSO), the ice crystals were more spicular and formed faster than the other study groups. Increasing the DMSO concentration led to the formation of fine ice crystals; however, no remarkable improvement in ice crystallization was observed when the saccharide concentration was increased, as the saccharide merely prevents osmotic damage to the cells. The fractal dimension (FD) theory, in conjunction with an image processing method, was employed to quantitatively compare the smoothness and the growth rate of the ice crystals. The FD value quantifies the geometry's irregularities. In our analysis, ice crystals' boundaries were extracted from the brightfield images and digitized, as depicted in Fig. 4.8-a. The FD value for the resulting quasi-circle geometry was then calculated using Eq. (4.1) [218]

$$FD = \frac{2ln\left(P/(2\pi)\right)}{ln\left(A/\pi\right)}\,, \tag{4.1}$$

where P and A stand for the perimeter and the area of the quasi-circle geometry, respectively. The FD value is an indicator of how the quasi-circle geometry deviates from a circle. When the geometry of interest is a perfect circle, the FD equals 1. As the irregularities and sharp edges appear in the geometry, the FD increases. For the freezing bioink, when ice crystals form, the geometry of the unfrozen region starts to diverge from a perfect circle, leading to an increased FD. The trends of changes in FD for freezing bioinks with different DMSO concentrations are shown in Fig. 4.8-b. In the control sample, i.e., DMSO-free, the highly spicular ice crystals formed rapidly, and therefore, the FD value was higher than those of the other groups. When 90% of the field of view was frozen, the FD values were recorded

and compared (Fig. 4.8-c). It is evident that the addition of DMSO significantly decreased the FD value. In Fig. 4.8-d, the percentages of the frozen areas were plotted over time to compare the freezing rates. The control sample froze faster than the other samples, and as the DMSO concentration increased, the freezing temperature decreased and the bioink started to freeze slower.

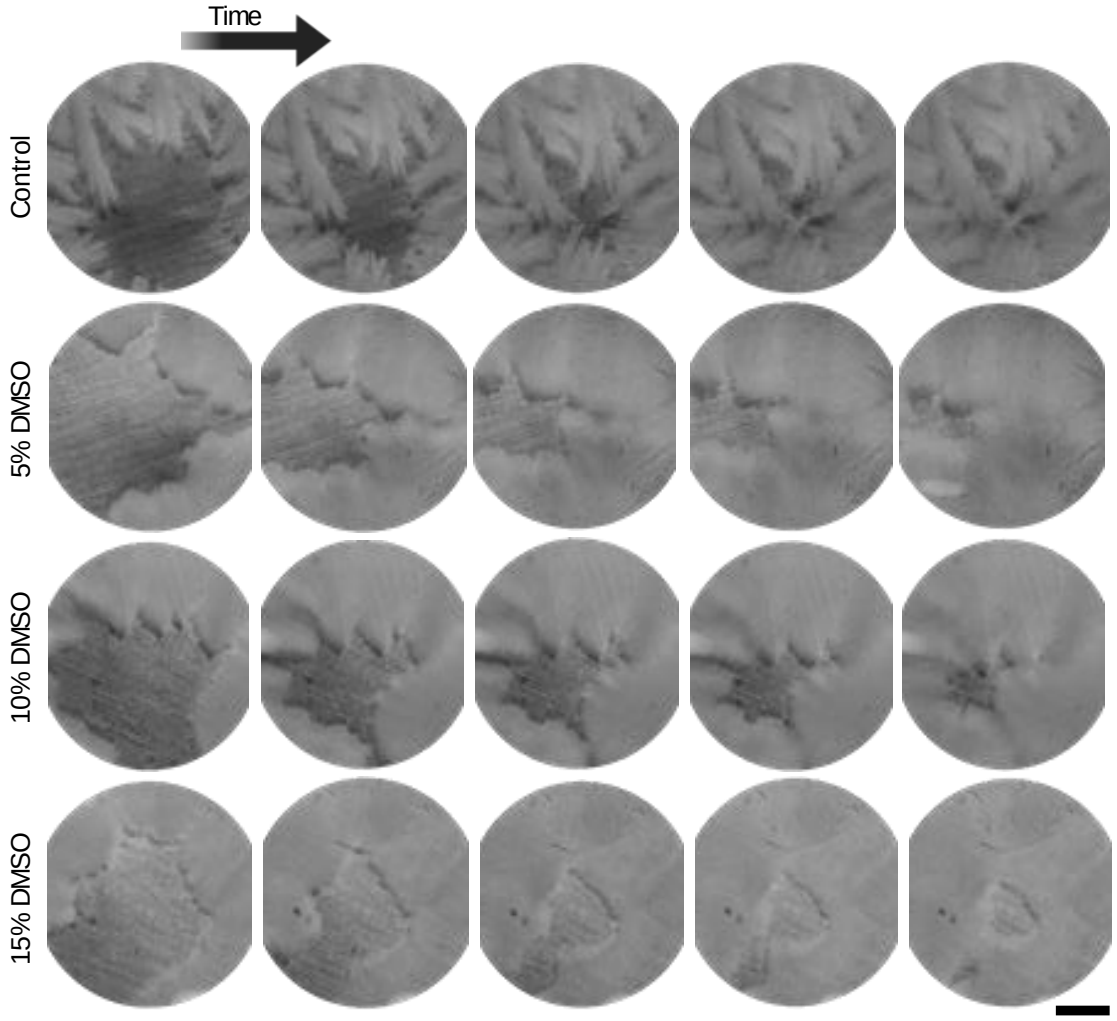

Fig. 4.7. Representative brightfield time-lapse images of GelMA hydrogel groups with different DMSO concentrations during ice crystal formation. The shape and the size of the ice crystals were clearly different in the DMSO-free sample. Scale bar: 2 mm.

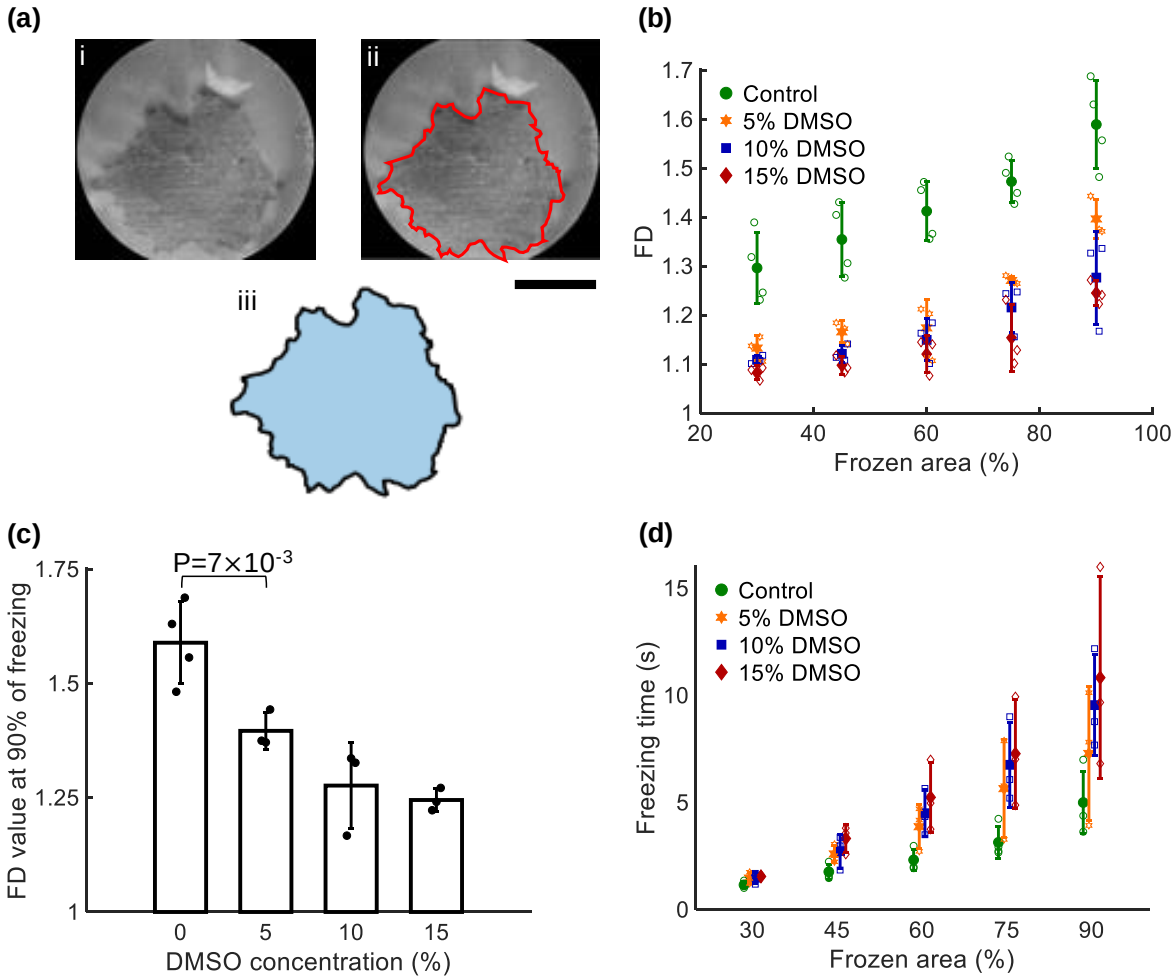

Fig. 4.8. Ice crystals quantification. **(a)** Identifying the ice crystals' borderline in a representative image for quantifying the sharpness of the ice crystals. The unfrozen portion of the hydrogel derived as a polygon in panel **iii** was used to quantify the ice crystals' sharpness. Scale bar: 2 mm. **(b)** Trend of changes in FD during the hydrogel freezing process. When the sharp crystals formed, the irregularities in the polygon geometry increased, which resulted in a higher FD value. **(c)** FD values for different hydrogels when 90% of the samples in the microscope's field of view became frozen. **(d)** Comparison of the freezing times for different hydrogel bioink groups. The addition of DMSO generally increases the freezing time. t=0 corresponds to when the frozen area is approximately 25% of the microscope's field of view. n = 4. (FD: fractal dimension)

4.2.2 Cryoprotective bioink design based on cell viability assays

A series of cell viability experiments were conducted using different concentrations of DMSO and saccharides to find the optimized configuration of the CPA in GelMA. Due to their lower molecular weight, monosaccharides generally show less protective effects regardless of concentration and freezing trend [183]. We, therefore, focused on using disaccharides (lactose, maltose, sucrose, trehalose) and trisaccharides (raffinose, melezitose) (Fig. 4.9) along with DMSO as the CPAs. The cell-laden cryobioprinted samples containing different concentrations of DMSO and saccharides underwent live/dead assay after 72 h of cryopreservation. Fig. 4.10 shows a representative set of live/dead images for immortalized mouse myoblast cells (C2C12) cryopreserved in 5% (w/v) GelMA with different DMSO and melezitose concentrations. Cell viability of C2C12 cells was determined using the fluorescence images (Fig. 4.11). Since the presence of saccharide avoids osmotic shock during the thawing process [184], the saccharide-free groups generally showed lower cell viability, regardless of the DMSO concentration. Saccharide was therefore deemed to be an essential part of a cryoprotective bioink.

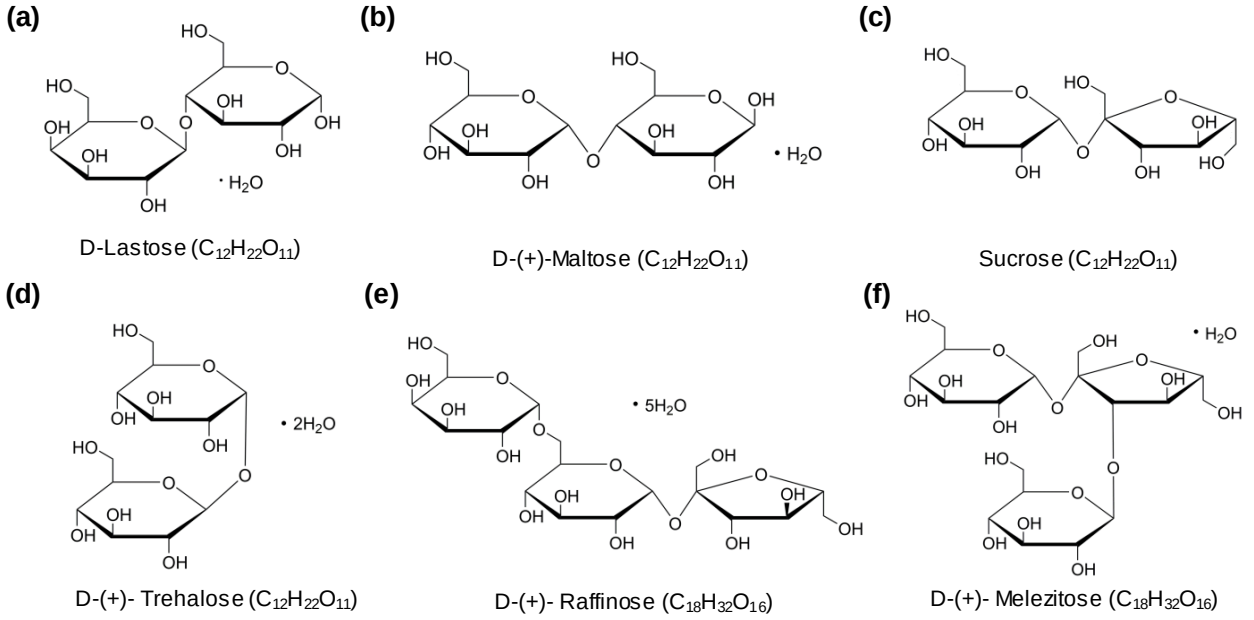

Fig. 4.9. Chemical structures of the investigated saccharides for cryobioprinting. **(a)** Lactose. **(b)** Maltose. **(c)** Sucrose. **(d)** Trehalose. **(e)** Raffinose. **(f)** Melezitose.

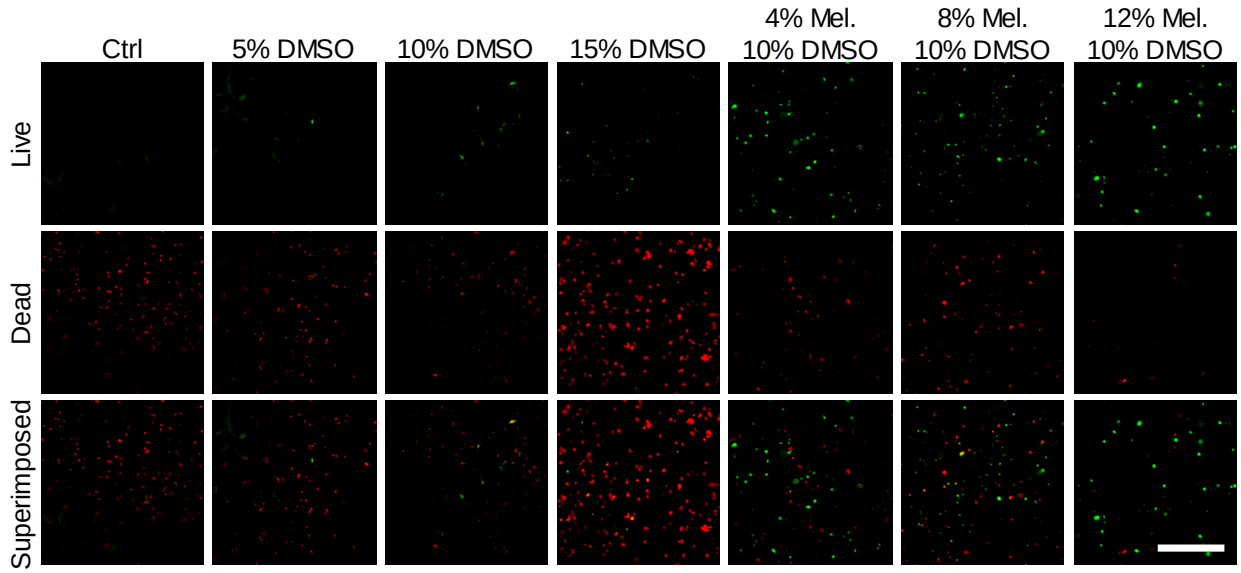

Fig. 4.10. Representative fluorescence live/dead images of the C2C12 cells encapsulated in bioinks, cryopreserved for 72 h, and resuscitated before staining/imaging. Live/dead staining was conducted based on the protocol provided in Section 2.2.2. The cryopreserved bioinks were prepared using 5% (w/v) GelMA, different concentrations of DMSO, and different concentrations of saccharides. Scale bar: 500 μm.

Cell viability of each group was normalized to the control group with the same DMSO concentration to choose the most functional saccharide and its optimum concentration (Fig. 4.12). The most effective saccharides that led to a higher cell viability increase were 12% (w/v) melezitose, 4% (w/v) raffinose, and 4% (w/v) lactose. The increase in cell viability of the groups with respect to the DMSO-free group with the same saccharide concentration was also calculated to identify the most effective DMSO concentration. As shown in Fig. 4.13, the optimum concentration of DMSO was 10% (v/v) for the selected sugar types. As a result, three combinations of CPAs were used with 5% (w/v) GelMA for the next set of experiments: 12% (w/v) melezitose+10% (v/v) DMSO, 4% (w/v) lactose+10% (v/v) DMSO, and 4% (w/v) raffinose+10% (v/v) DMSO. In the following sections, we refer to these selected groups using the names of their saccharides only, considering that they all contained 10% (v/v) DMSO and 5% (w/v) GelMA.

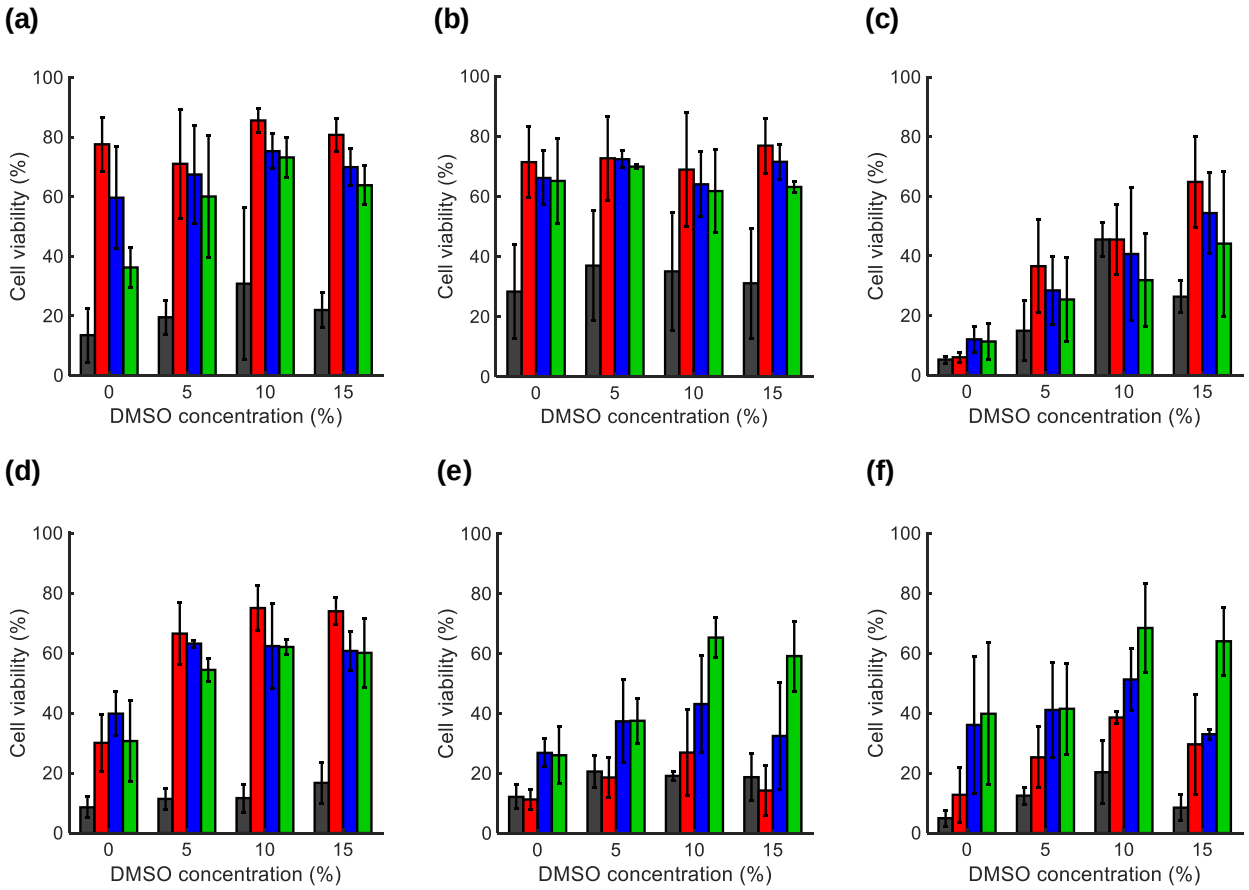

Fig. 4.11. Cell viability in GelMA hydrogels with different concentrations of DMSO and saccharides cryopreserved for 72 h. (Gray: No saccharide; Red: 4% saccharide; Blue: 8% saccharide; Green: 12% saccharide) **(a)** Raffinose. **(b)** Sucrose. **(c)** Maltose. **(d)** Lactose. **(e)** Trehalose. **(f)** Melezitose. The data is presented as mean n=3.

4.2.3 Using different cell types to assess the effectiveness of the CPAs

The efficacy of the CPAs varies with the cryopreserved cell type and cell size [219]. We studied the cell viability of six other cell types, including mouse embryonic fibroblast cell line (NIH/3T3), human liver cancer cell line (HepG2), human breast cancer cell line (MCF-7), primary human smooth muscle cells (SMCs), primary human umbilical vein endothelial cells

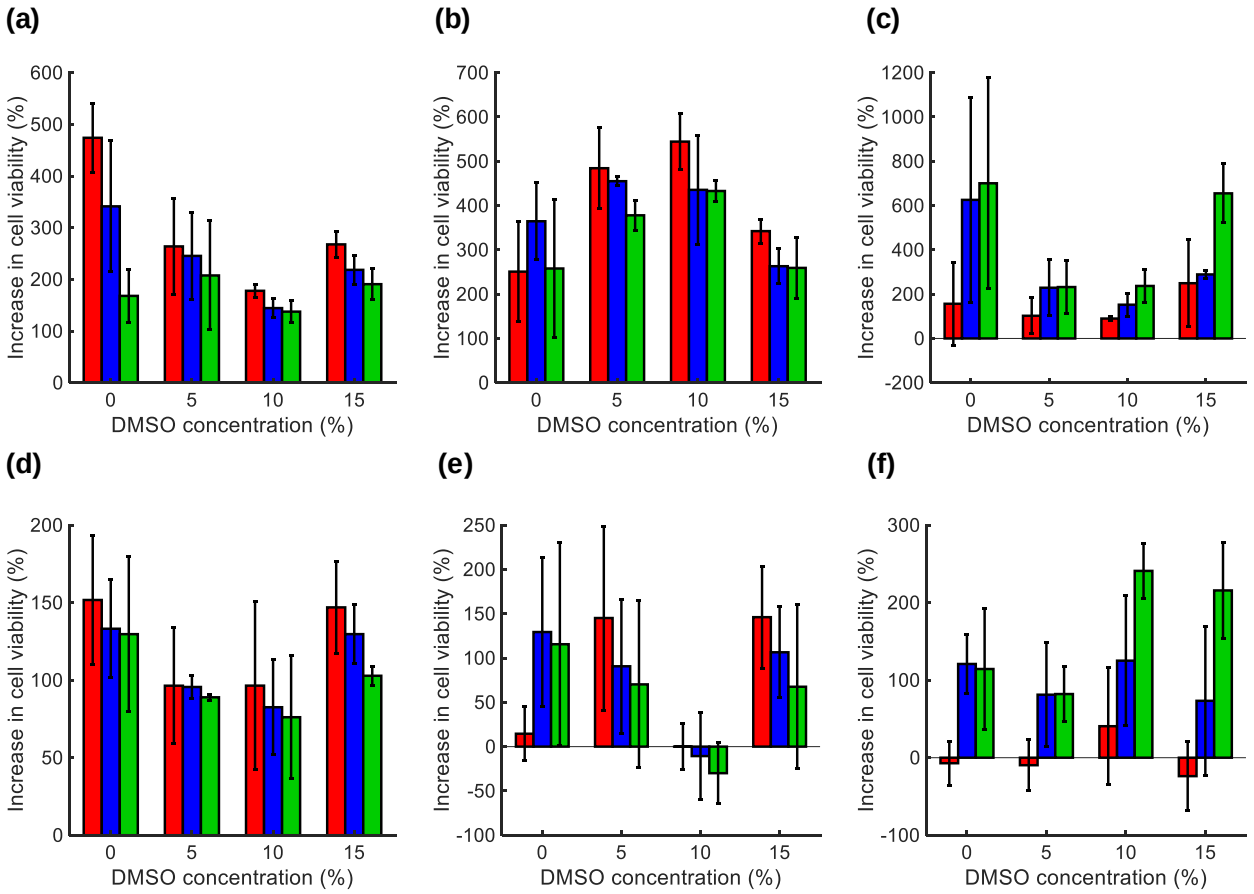

Fig. 4.12. Quantified increases in cell viability post-cryopreservation for 72 h due to supplementing the cryoprotective bioink with different saccharides. (Red: 4% saccharide; Blue: 8% saccharide; Green: 12% saccharide) **(a)** Raffinose. **(b)** Lactose. **(c)** Melezitose. **(d)** Sucrose. **(e)** Maltose. **(f)** Trehalose. n=3.

(HUVECs), and primary human mesenchymal stem cells (hMSCs), using the three selected bioink groups to assess the feasibility of the cryobioprinting method. As demonstrated in Fig. 4.14, all the cell types were significantly more viable after 72 h of cryopreservation in the selected groups compared to the control group, i.e., the group without any CPAs. The high cell viability values for all the cell types confirmed the effectiveness of all three CPA combinations. Given the higher cell viability rates and solubility, the melezitose group was selected for subsequent cryobioprinting jobs.

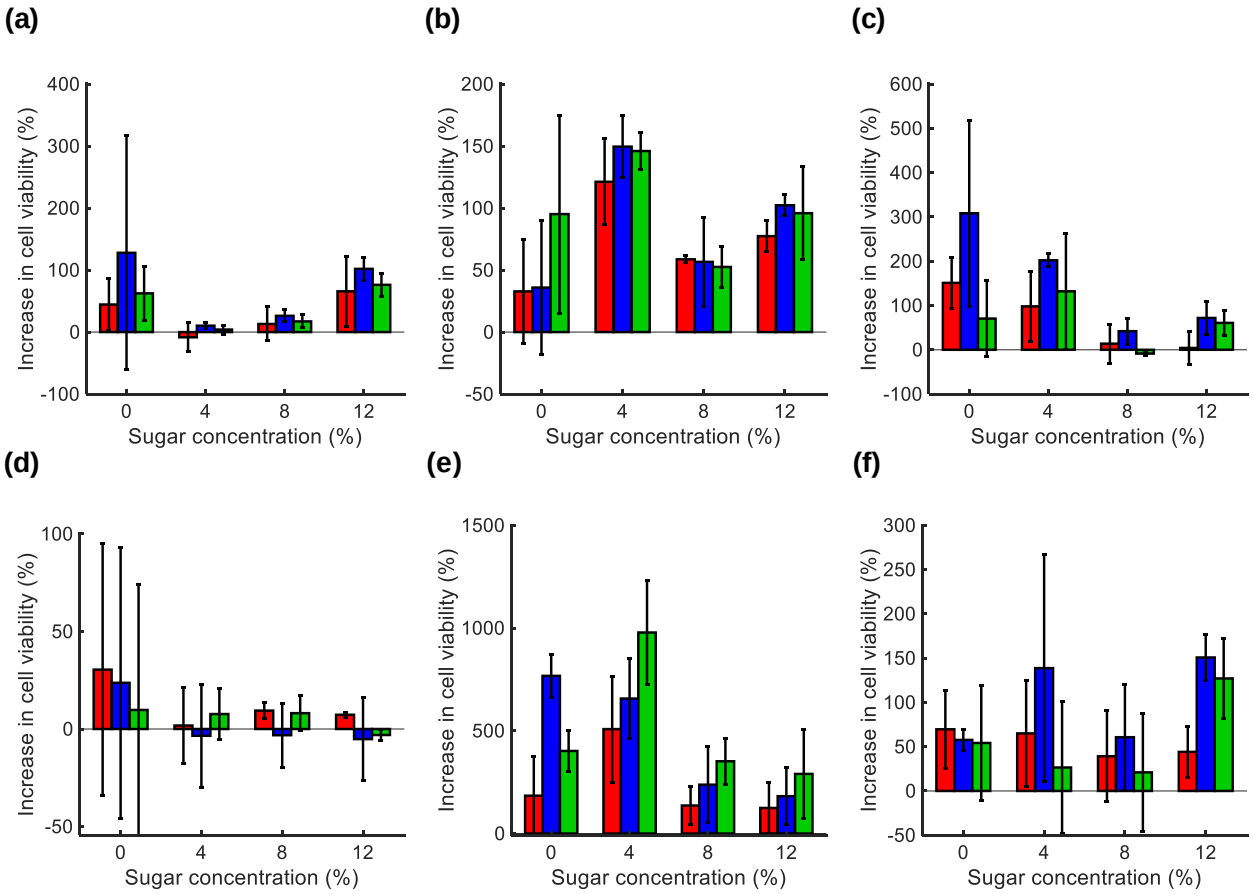

Fig. 4.13. Quantification of the effect of DMSO in the cryoprotective bioink formulations on enhancing cell viability post-cryopreservation for 72 h. (Red: 4% saccharide; Blue: 8% saccharide; Green: 12% saccharide) **(a)** Raffinose. **(b)** Lactose. **(c)** Melezitose. **(d)** Sucrose. **(e)** Maltose. **(f)** Trehalose. n=3.

4.2.4 Effect of the CPAs on the cells before cryobioprinting

In extrusion bioprinting, it is inevitable to keep the cells in contact with the bioink/CPAs for several minutes. Contact with the CPAs over an extended time period before cryobioprinting may jeopardize cell viability due to toxicity of the DMSO and the prolonged exposure to osmotic pressure caused by the presence of saccharide molecules. In this section, the cell viability of the NIH/3T3 fibroblasts encapsulated in GelMA/CPA after being kept at room temperature (RT) for different time periods was investigated. As shown in Fig. 4.15, increased

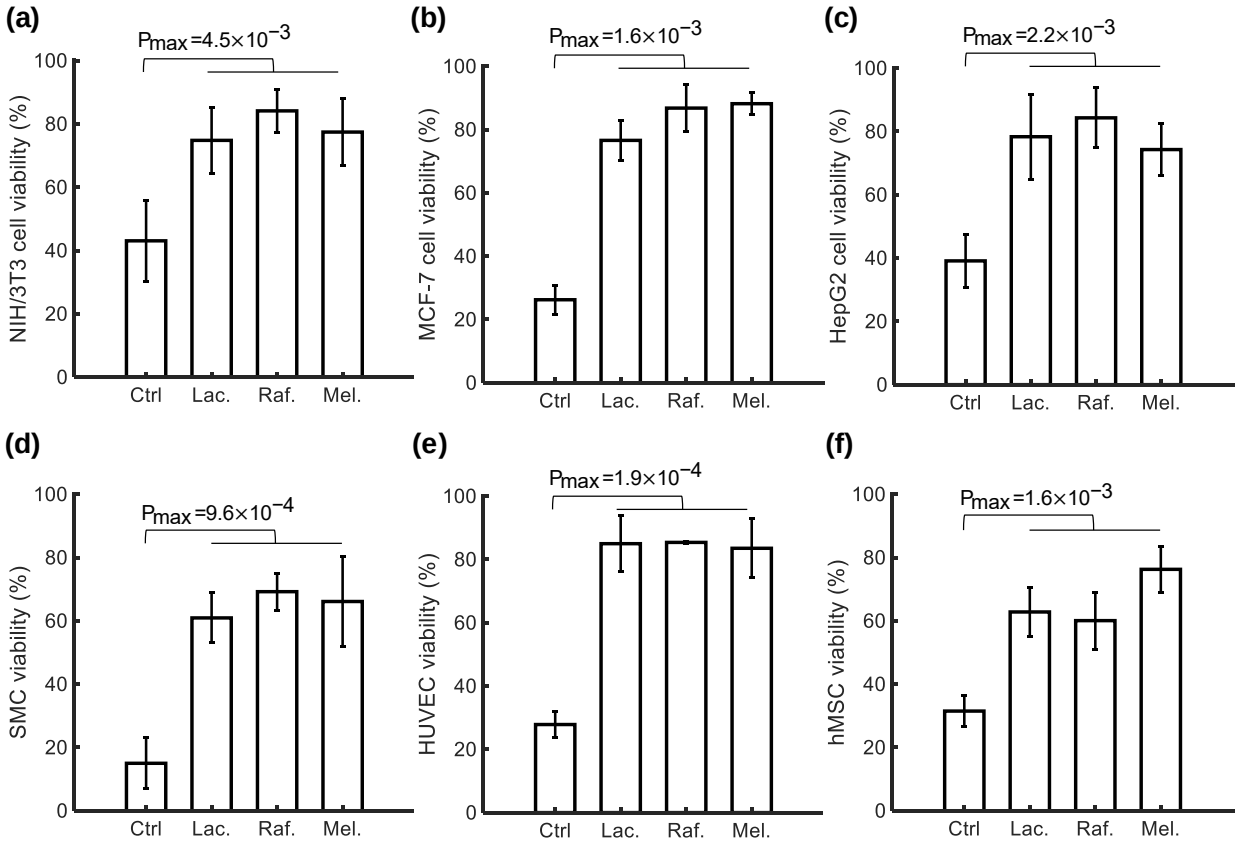

Fig. 4.14. Cell viability of various cell types when selected CPAs were employed. (Ctrl: Control; Lac.: lactose; Raf.: raffinose; Mel.: melezitose) n = 3.

exposure time yields lower cell viability. We, therefore, minimized exposure time for our cryobioprinting jobs by using small aliquots of bioinks for each round. The viability drop within 60 min of exposure was acceptable at >80%.

4.2.5 Effect of T_p on cell viability

The sample freezing rate during the cryobioprinting process has a critical impact on ice crystal-formation and cell viability. Different freezing rates were achieved by changing T_p. Representative live/dead images of the NIH/3T3 fibroblasts cryobioprinted on the freezing plate with various temperatures, -5 °C, -10 °C, -15 °C, and -20 °C, are shown in Fig. 4.16-a, b. The samples were stained and imaged immediately after cryobioprinting. For cases for which

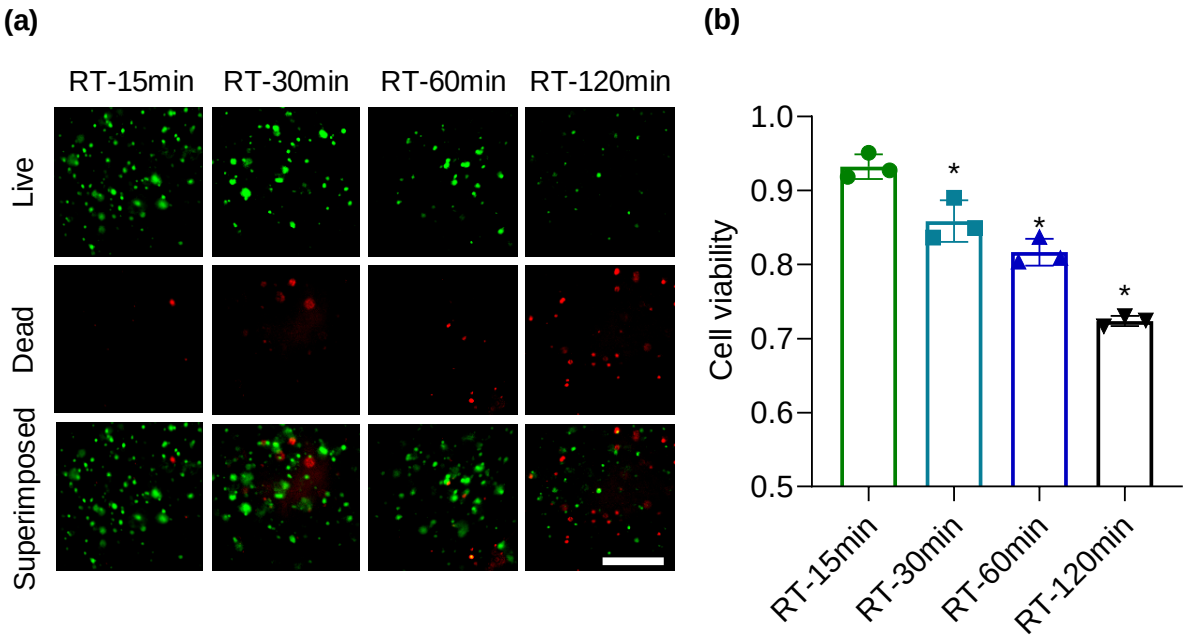

Fig. 4.15. Effects of keeping NIH/3T3 cells in contact with the selected CPAs (DMSO+melezitose) within GelMA for different timespans. **(a)** Fluorescence live/dead images. Live/dead staining was conducted based on the protocol provided in Section 2.2.2. **(b)** Quantification of cell viability based on the ratio of viable cells over the total number of cells. Scale bar: 500 μm. n=3; *P<0.05.

T_p was -15 °C, the cell viability was not significantly different from the original unbioprinted bioink. However, decreasing the T_p to -20 °C caused a major decline in cell viability (only 60% viable cells).

4.2.6 Medium-term and long-term cryopreservation

Cryobioprinted hMSC-laden samples were cryopreserved for 14 and 28 days to study the effect of medium-term cryopreservation on cell viability. No significant difference between the cell viability rates of the cryopreserved samples in liquid nitrogen was observed after day 14 and day 28 (Fig. 4.16-c, d). More importantly, the viability of NIH/3T3 fibroblasts and HUVECs after 3 months of cryopreservation were determined to be 83% and 86% (ratio of viable cells over the total number of encapsulated cells) after 7 days of culture, respectively

(Fig. 4.17), proving the efficacy of our cryobioprinting method for longer-term storage.

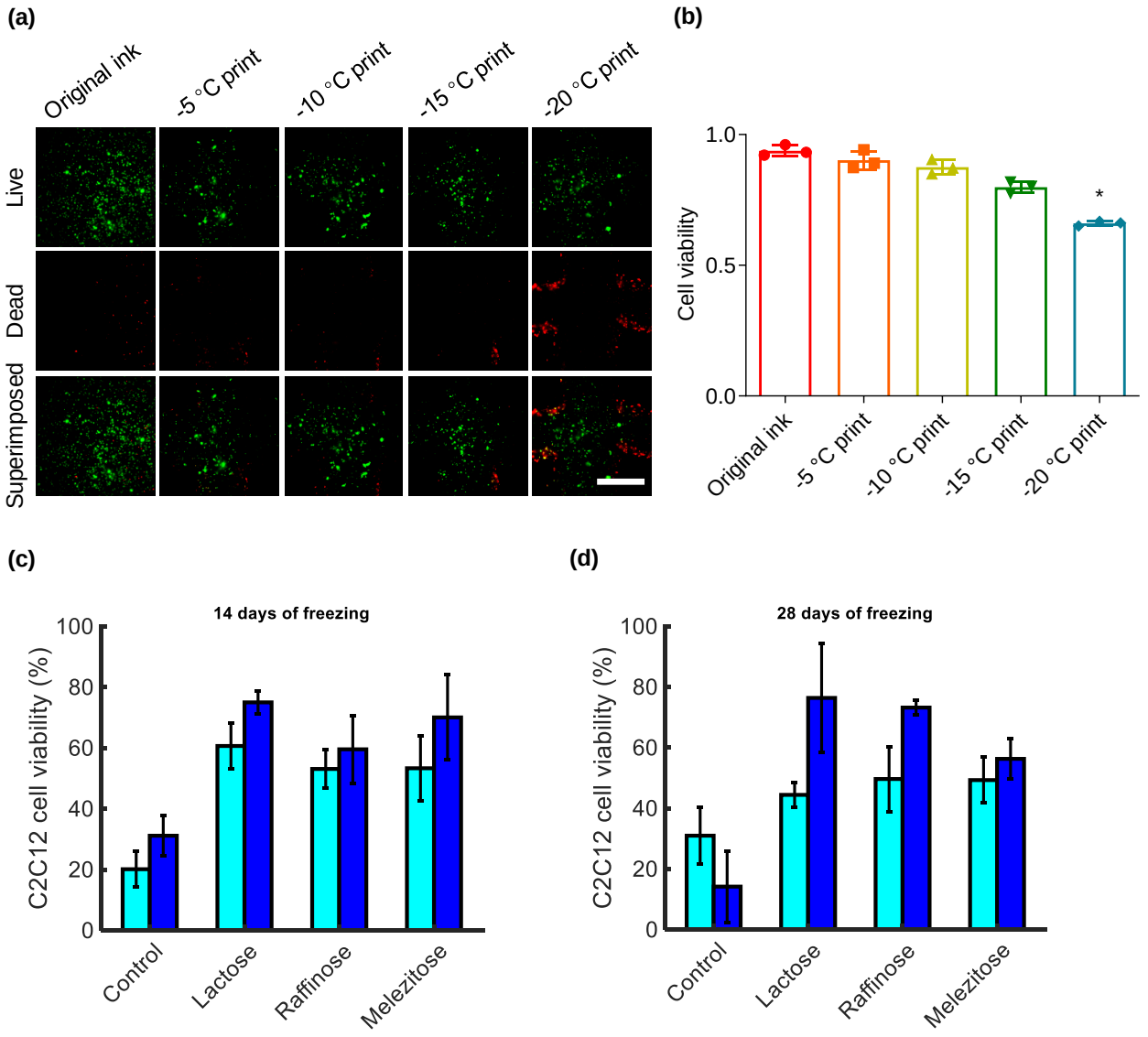

Fig. 4.16. Effects of the freezing plate and the cryopreservation temperatures on the cell viability. **(a)** Fluorescence microscopy images showing viability of NIH/3T3 cells in the GelMA/CPA matrix after cryobioprinting at different temperatures of the freezing plate. Scale bar: 500 μm. **(b)** Quantification of cell viability. **(c)** Shorter-term, and **(d)** longer-term cryopreservation at -80 °C and -196 °C. (Cyan: -80 °C Freezer; Blue: -196 °C Liquid nitrogen) n=3; *P<0.05.

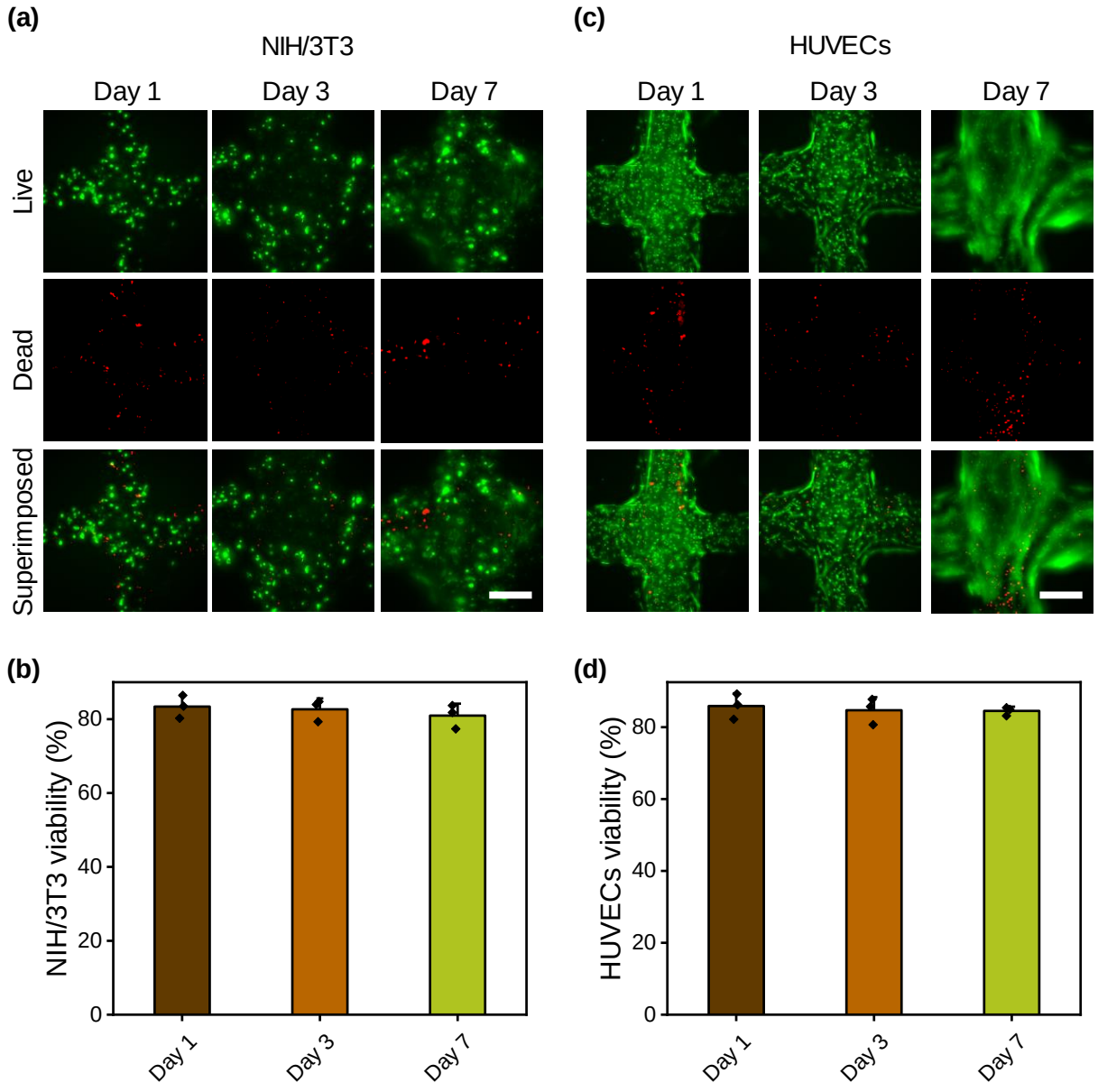

Fig. 4.17. Cell viability of cryobioprinted cell-laden constructs after 3 months of cryopreservation at -196°C (liquid nitrogen), at different days post-revival. **(a)** and **(b)** NIH/3T3. **(c)** and **(d)** HUVECs. Scale bars: 500 μm.

4.3 Functionality of the cryobioprinted products

4.3.1 Cell differentiation

The functionality of hMSCs after cryobioprinting was investigated through cell differentiation assays. Fig. 4.18 shows the live/dead images for hMSCs after 72 h of cryopreservation. Based on the medium-term results, cryobioprinted hMSCs-laden samples were used after 14 days of cryopreservation in liquid nitrogen. On day 14, the samples were crosslinked, resuscitated, and cultured for 1 week before adding the differentiation media. The three types of cell differentiation, including osteogenic, chondrogenic, and adipogenic, were studied. In osteogenesis differentiation, runt-related transcription factor 2 (RUNX2, 1 week) and osteocalcin (2 and 3 weeks) immunostaining were conducted. Peroxisome proliferator-activated receptor gamma (PPARγ) and SOX-9 immunostaining assays were used for assessing adipogenic and chondrogenic differentiation, respectively. In Fig. 4.19, the fluorescence and immunostaining images of the encapsulated hMSCs after being cultured in differentiation media for 7 days, 14 days, and 21 days are presented. The quantitative analyses of osteogenesis (Fig. 4.20-a, b), chondrogenesis (Fig. 4.20-c, d), and adipogenesis (Fig. 4.20-e, f) revealed that the trends of differentiation in cryobioprinted samples were not notably different than those in control samples (i.e., the unfrozen samples). This finding proves that cryobioprinting did not affect the capability of hMSCs to differentiate.

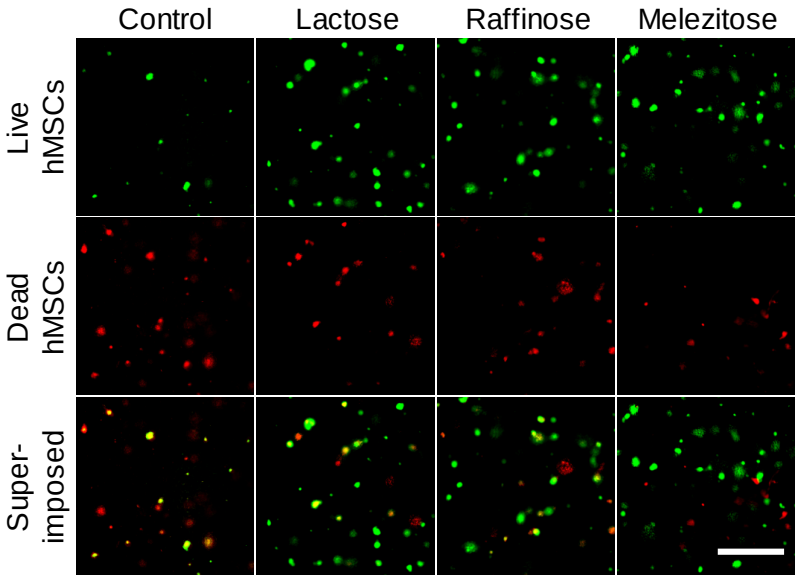

Fig. 4.18. Representative live (green)/dead (red) fluorescence images of hMSCs encapsulated in the three selected cryoprotective bioinks and cryopreserved for 72 h. Scale bar: 500 μm.

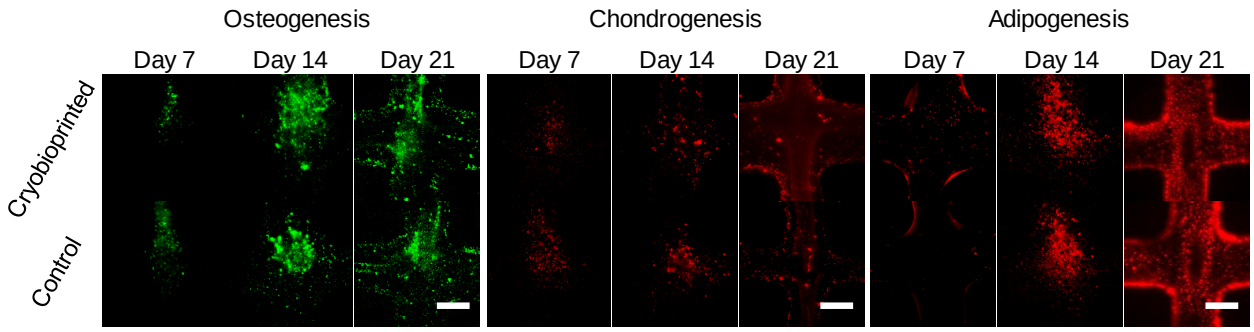

Fig. 4.19. Fluorescence micrographs of hMSCs differentiation assays in cryobioprinted GelMA/CPA constructs. Scale bars: 500 μm. n=3.

4.3.2 Chorioallantoic membrane (CAM) assay

Angiogenesis potentials of the cryobioprinted scaffolds was evaluated via CAM assay. The cryobioprinted constructs (previously stored in liquid nitrogen for 14 days) were implanted on day-7 ex ovo CAM and were collected after 7 days of additional incubation (Fig. 4.21-a). The extents of angiogenesis in the cryobioprinted groups were determined using an image-processing method and histology (Fig. 4.21-b). The average lengths of newly formed blood vessel (BV) series were measured to quantify the angiogenic responses surrounding the different cryobioprinted constructs. As presented in Fig. 4.22-a, the smallest average length of BVs was associated with the control group (i.e., cryobioprinted GelMA+CPA) while adding either HUVECs or vascular endothelial growth factor (VEGF) resulted in a significant increase in the BV length. Cryobioprinted constructs with both HUVEC+VEGF (H&V) yielded the highest vascular growth. When the same bioink (H&V) was bioprinted at RT without freezing, similar vascular growth was achieved. These observations proved that the cryobioprinting procedure did not affect the functionality of HUVECs and VEGF.

Histological analyses further confirmed that the presence of HUVECs had a significant effect on CAM vessel formation within the 3D constructs (Fig. 4.21-b). Almost no BVs grew into the control group, while the vascular infiltration in the HUVECs group was significantly higher. Similarly, vascular invasion in the H&V group was substantially higher than that of the VEGF group. Furthermore, neovascularization was observed deep in the H&V group, as shown in the histology images.

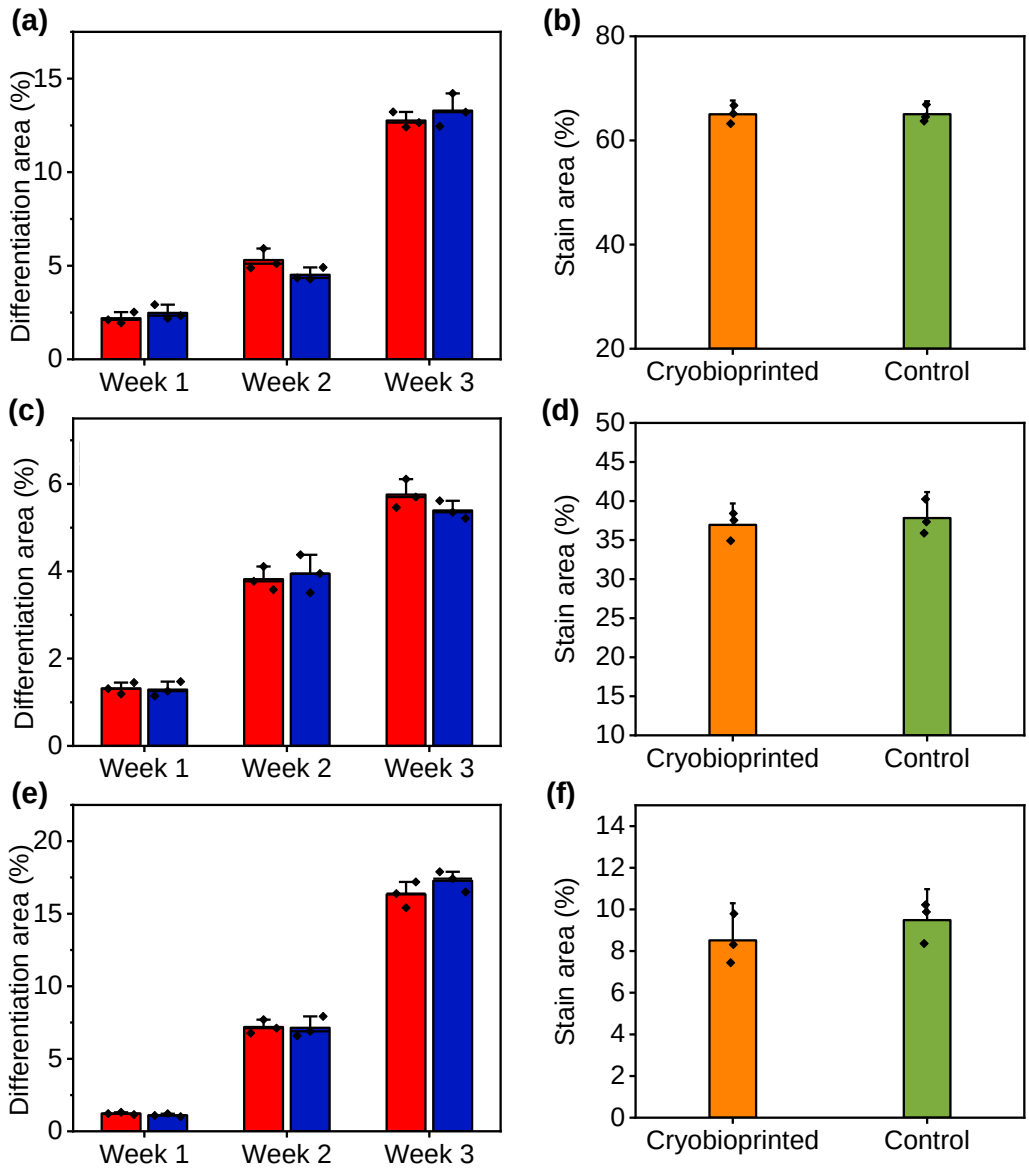

Fig. 4.20. Quantitative cell differentiation results. Osteogenic differentiation: **(a)** Semi-quantitative measurements of RUNX2 (1 week) and osteocalcin (2 and 3 weeks), and **(b)** quantification of Alizarin Red S-staining (3 weeks). Chondrogenic differentiation: **(c)** Semi-quantitative measurements of SOX-9, and **(d)** quantification of Alcian blue staining (3 weeks). Adipogenic differentiation: **(e)** Semi-quantitative measurements of PPARγ, and **(f)** quantification of Oil Red O staining (3 weeks) (Red: Cryobioprinted; Blue: Control).

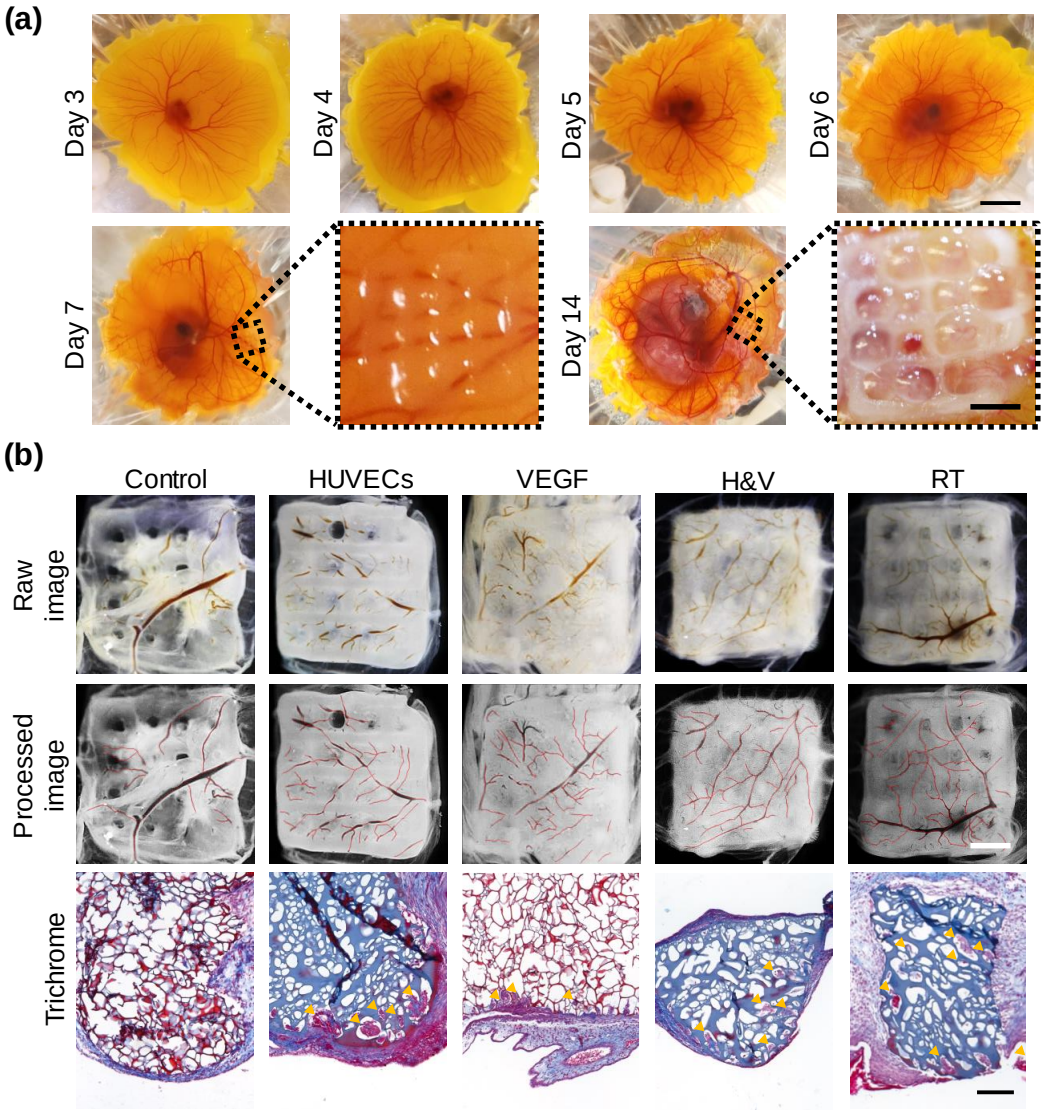

Fig. 4.21. Chick ex ovo culture and CAM assay for investigating the vascularization in cryobioprinted scaffolds. **(a)** Representative images of chick ex ovo culture with implanted cryobioprinted scaffolds for CAM assay in different timesteps. Scale bars: 2 cm for the low-magnification images and 2 mm for the high-magnification images. **(b)** Angiogenic abilities of the scaffolds and Goldner's trichrome staining showing erythrocytes in red and collagen in green, where the blood vessels are indicated by yellow arrowheads. Scale bars: 2 mm for optical images and 200 μm for histology images.

The BV density (Fig. 4.22-b) and the ratio of BV-to-tissue areas (Fig. 4.22-c) within the constructs was also quantified. The BV density was calculated as the number of BVs within 1 mm of the interface along the scaffold/tissue border. The ratio of the BV-to-tissue area was defined as the percentage of the BVs area over the area of the section [200]. The density of the BVs in the HUVECs group was significantly higher than that in the control group. Similarly, the H&V group showed a significantly higher BV density than the VEGF group. The ratio of BV-to-tissue areas also resulted in a similar trend.

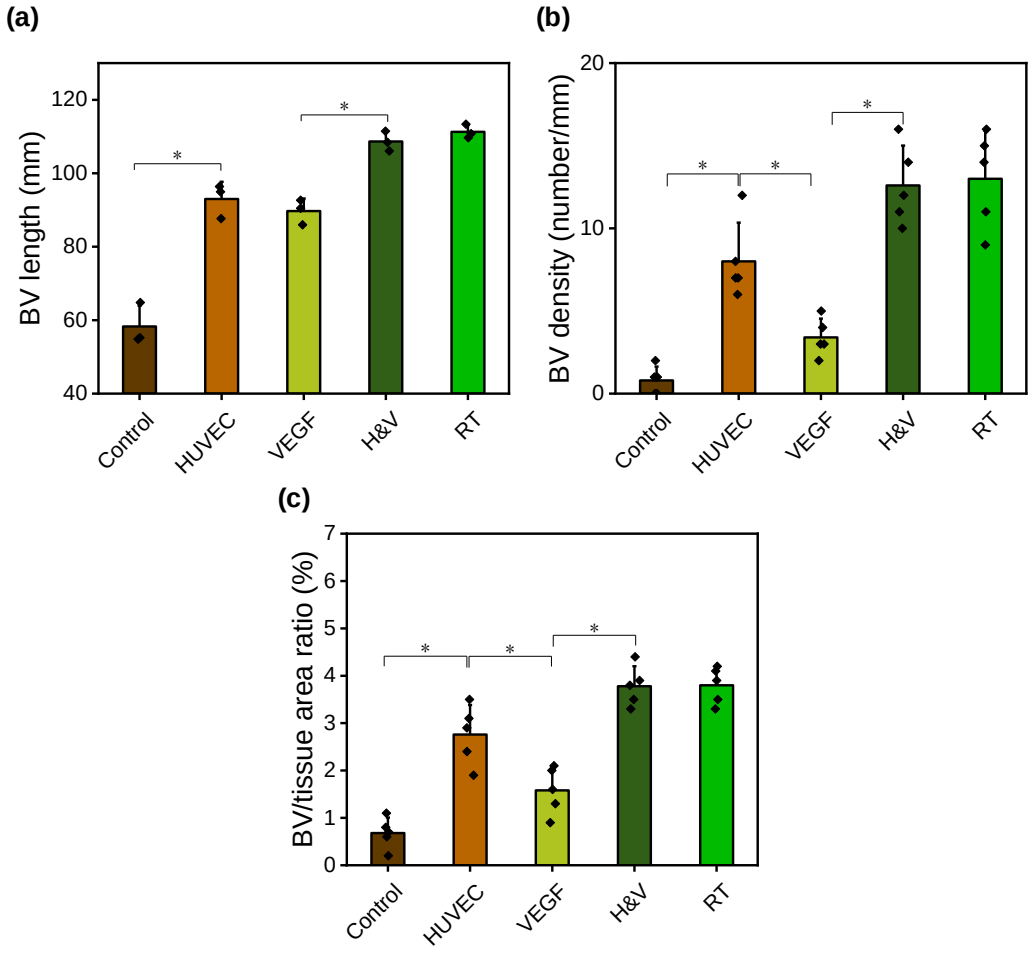

Fig. 4.22. Quantification of the BV growth surrounding and within the cryobioprinted constructs by measuring different parameters. **(a)** Lengths of the BVs surrounding the scaffolds. **(b)** BV densities. **(c)** The ratio of BV-to-tissue areas within the scaffolds. n=5; *P<0.05.

4.4 Discussion

Considering the propensity to use shelf-ready products for clinical needs, the development of biofabrication methods capable of creating storable tissue constructs is useful. In this chapter, the invention and optimization of cryobioprinting, a biofabrication process to simultaneously create and store tissue constructs was explained. The results emphasized the unique synergy between bioprinting and cryopreservation, leading to faithful fabrication of tissue constructs with an uncompromising cell viability rate. One of the key points in our approach was designing a freezing plate that allowed precisely controllable and stable temperature during the cryobioprinting procedure.

The limited printability window of soft materials, especially hydrogels, restricts the availability of bioinks [141]. For example, 5% (w/v) GelMA bioink should be kept at approximately 15 °C or lower to be applicable for bioprinted constructs [7]. In cryobioprinting, the deposited layers immediately freeze in situ. This rapid solidification enhances the printability of the bioink and fidelity of the 3D-bioprinted constructs, providing an expanded range of options to be used as the bioink. Free-standing and oblique constructs have been previously bioprinted using a cell-friendly supporting bath as the collecting substrate [6, 220–223]. Our cryobioprinting approach offers another suitable method for bioprinting such constructs (Fig. 4.5-p to r), without any need for supporting baths, extra supports, or sacrificial materials. Another advantage of cryobioprinting is the capability of fabricating ready-to-use products. No washing steps are required to remove excessive supporting materials that exist in embedded bioprinting. This feature can transform cryobioprinting into a promising method for leveraging the scalability of the 3D bioprinting technology.

Fetal bovine serum (FBS) is normally used as the CPA in place of saccharides in conventional cell cryopreservation. Since the FBS content varies based on the source of derivation, the cryopreservation efficiency might be affected in an unknown manner. We, therefore, used well-defined saccharides for cryobioprinting to systematically track the CPAs' effect. Saccharides, as non-permeating CPAs, can preserve the cells during the thawing process by minimizing the osmotic shock [224]. It has been previously reported that raffinose in concentrations of 10-18% (w/v) is an effective CPA [225]. Other researchers have shown that melezitose and maltose offer acceptable and practical cryoprotective effects [188]. Trehalose

and sucrose may also reduce the intramembrane lateral stress [226]. Apart from saccharides, DMSO is a permeating CPA that prohibits the formation of intracellular spicular ice crystals. Our findings showed that cell viability is a function of the type and the concentration of CPAs. Furthermore, the freezing regime had a critical effect on cell viability. For many types of cells, there is a so-called "temperature danger zone", which lies between -15 °C to -60 °C [172]. During the freezing/resuscitation processes, the cells pass this range of temperature twice. Increased time period in this zone, generally increases the risk of cell damage. In addition, slow freezing causes a gradual increase in the solute concentration of the intra- and extracellular solutions, leading to a change in osmotic pressure [227]. When the freezing procedure is too rapid on the other hand, the chance of intracellular ice crystallization and cell damage increases [228]. These opposite effects contribute to reduce cell viability, thereby narrowing the range of optimum cryopreservation.

As thoroughly reviewed before [229], the formation of sharp ice crystals at the ice nucleation point may jeopardize the viability of encapsulated cells. It was found that the addition of CPAs decreased the sharpness and sizes of the ice crystals in the frozen hydrogel constructs. It was previously reported that CPAs lower the freezing point of water and changes the ice crystals' microstructure [177]. We observed a similar phenomenon for GelMA-based cryoprotective bioinks. Avoiding the formation of spicular ice crystals is critical during freezing/thawing and helps keeping the cells intact [230]. In complement to the benefits of CPAs, the hydrogels' 3D network also reduces ice-crystal formation, thereby contributing to an intrinsic physical cryoprotective microenvironment for the cells [217, 231].

CHAPTER 5

Conclusions and perspectives

This chapter is focused on summarizing the main conclusions of the thesis regarding the design and biofabrication of cell-laden implants for tissue engineering (TE) applications. The outcome of using carbon nanotube (CNT) as an additive in fabricating composite hydrogels is discussed and the role of cryobioprinting in the evolvement of the field of biofabrication is elaborated. The last part of this chapter is dedicated to comprehensively explaining the future directions and perspectives in the field of biofabrication, specifically three-dimensional (3D) bioprinting.

5.1 Conclusions

5.1.1 Characteristics of CNT composite hyrdogels

The unique properties of CNTs were postulated to enhance the mechanical, biological, and physoical properties of the hydrogels. Based upon this hypothesis, the addition of carboxylic acid-functionalized carbon nanotubes (COOH-CNTs) and hydroxyl-functionalized carbon nanotubes (OH-CNTs) in a glycol chitosan (GC) hydrogel matrix was explored for possible applications as an injectable biomimetic hydrogel in TE. The two types of CNTs were separately incorporated in GC hydrogels and underwent biological, rheological, and physical tests. Although hydrogels made of COOH-CNTs exhibited a lower cytocompatibility in comparison with OH-CNTs-based hydrogels, they were found to be preferable as they caused

a 120% enlargement in the hydrogels' pore size. Such increase in porosity has not been previously reported. It was also found that the gelation time and the mechanical properties of the carbon nanotube glycol chitosan (CNT-GC) composite hydrogels do not necessarily change in proportion with the CNT concentration. The key outcome of this phase of the project was that COOH-CNTs increase the average pore size of the GC hydrogel. A larger pore size may improve cell migration and cell adhesion in the cell-laden scaffold.

5.1.2 Cell-biomaterial interactions in CNT composite hyrdogels

A paramount motivation for adding CNTs in hydrogels was to enhance the focal adhesion sites for the encapsulated cells and therefore increase cell-biomaterial interactions. It was observed that the addition of CNTs changed the morphology of the encapsulated cells and increased cell adhesion in the hydrogel. Cell recruitment and the cell migration rates also significantly enhanced when COOH-CNTs at concentrations of 250, 500, and 750 μg ml^{-1} were incorporated in a GC hydrogel. The stress relaxation time changed only slightly with modulating CNT concentration, and the trend of changes was different from that of the cell migration and cell adhesion. Stress relaxation time is therefore not correlated with cell migration. In summary, CNTs could positively affect cell-material interaction and enhance cell migration and adhesion in hydrogels.

5.1.3 Cryobioprinting

A novel biofabrication method was developed by synergistically combining the advantages of bioprinting and cryopreservation methods. With the aid of a custom-designed freezing plate, faithful cell-laden tissue constructs were biofabricated. A systematic cell viability study was employed to effectively design the bioink based on a combination of optimized cryoprotective agent (CPA) and gelatin methacryloyl (GelMA). It was found that trisaccharides are generally more effective in terms of cryopreservation comparing to disaccharides. The findings presented in this thesis showed that cryobioprinting is a feasible method for fabricating cell-laden storable tissue constructs to be used as the next generation of shelf-ready implants. Intriguingly, the cryobioprinted cell-laden constructs were stored for up to 3 months without any significant reduction in cell viability. Apart from viability, the functionality of the cryobioprinted

cells is also essential for developing a practical biofabrication approach. Two methods were employed to demonstrate how different types of cells could remain functional after being cryobioprinted. First, the differentiation of human mesenchymal stem cells (hMSCs) was investigated. It was shown that similar to normal hMSCs, cryobioprinted hMSCs were able to successfully differentiate to osteoblasts, chondrocytes, or adipocytes when exposed to proper differentiation media. Furthermore, we demonstrated that cryobioprinted human umbilical vein endothelial cells (HUVECs) and vascular endothelial growth factor (VEGF) could maintain their ability to induce angiogenesis when investigated in the chorioallantoic membrane (CAM) assay. These in vitro cell differentiation studies and ex ovo CAM assays shed light on the efficacy of cryobioprinting as a functional approach for creating cell-laden implants or tissue models. As the field of tissue engineering grows fast, expanded applications are readily envisaged for these storable implants.

5.2 Perspectives and future directions

5.2.1 Composite hydrogels

The addition of fibers, nanotubes, and nanoparticles to hydrogels for creating composite biomaterials for different biomedical applications have attracted a great deal of attention. One possible direction that can be followed in future studies is the use of conductive composite hydrogels. Conductive CNTs can be embedded in cell-laden hydrogels to be used as stimulators for faster cell growth. Specifically, applying harmonic electrical voltage to CNTs with piezoelectric properties, may induce periodic micro-oscillations. This vibration may resemble the environments such as vocal folds, where the cells are subject to periodic oscillations.

One of the key applications of composite hydrogels is in 3D bioprinting. “In terms of the printing materials themselves, tremendous achievements have been made in the past few years regarding the development of composite inks. With designer characteristics and flexibility, composite inks are showing great potentials for clinically repairing/replacing biological tissues.” “However, long-term stability should be emphasized when developing composite inks. Despite the great efforts that have been made to improve the toughness of

composite materials, few of them enhance the fatigue threshold. It is critically needed to improve the threshold of printed composite inks when repairing mechanically active tissues, such as tendon and cardiac tissues where cyclic loading is experienced. A potential solution to improve the toughness and threshold of the printed composite structures is to use a reversible chemical cross-linking mechanism. Commonly used reversible bonds include dynamic covalent bonds, ionic bonds, hydrogen bonds, hydrophobic interactions, dipole–dipole interactions, and host–guest interactions. Some of these bonds can reform quickly upon rupture while others may require outside stimuli, such as elevated temperature, pH change, presence of enzymes, or light exposure [232–234]. Improving the fatigue threshold may be realized through the interactions between the matrices and the composite materials."

"The rapidly evolving four-dimensional (4D) printing technology is driving the advanced design of stimuli-triggered soft robotics. Common strategies utilize the anisotropy or gradient material properties created by the precision positioning of composite inks to sense the external triggers [141, 235, 236]. Shape-changing hydrogels and hydrogel actuators are especially interesting for applications as artificial muscles and cell-manipulators. In spite of the sensitivity to various environmental changes, such as temperature, humidity, and light, the responses of most current 4D printing technologies are much slower compared to traditional robotics. The slow real-time responses of hydrogel actuators may be due to the slow water diffusion-induced hydrogel volume transition and the hysteresis behavior caused by reversible chemical bonds and intermolecular interactions [237]. To drive the field forward, composite inks yielding hydrogels with fast responses to external stimuli need to be developed. Methods such as designing hydrogels without mechanical hysteresis may provide a solution to this challenge [238, 239]. The limited sensing ability for each type of hydrogels also restricts the ability of 4D-printed devices. Developing multiresponsive and biocompatible triggers is also critical to ensuring the implementation of this technology in biological environments."

5.2.2 Bioprinting

One of the critical aspects of TE and regenerative medicine is the capability of biofabricating cell-laden implants. Inert implants have been developed for years and are already commercially available for many applications, such as dentures and dental implant replacements. However,

there are still many obstacles in the advancement path of cell-laden soft implants. Although the use of bioprinting have facilitated the fabrication of cell laden constructs, more improvements are needed. Each of the four primary bioprinting technologies, introduced in Section 1.3.4, has its own advantages and disadvantages. In Fig. 5.1, these technologies are compared in three aspects: bioprinter basics, cost-effectiveness, and functionality. Due to their simplicity and prevalence, nozzle-based techniques provide the basics of a bioprinter in a more cost-effective manner. However, in terms of functionality, the laser/light-based technologies, i.e., laser-induced forward transfer (LIFT) and vat-polymerization, are likely more advantageous.

Regarding the bioprinter basics, extrusion and inkjet bioprinters are very flexible to be upgraded for bioprinting more than a single material. There are, however, complications for accommodating this feature in laser/light-based technologies, although not impossible. Another advantage of nozzle-based techniques is the relatively high material-switching speed, which is missing in laser/light-based methods. LIFT and vat-polymerization are excellent in terms of printing speed; however, their building volumes and user-friendliness cannot compete with the extrusion method, at least at this stage of development. In general, nozzle-based modalities are more commercially available, which results in a lower price for their hardware and consumable parts. Furthermore, the minimal bioink usage, due to the intrinsic nature of nozzle-based techniques, and the abundance of compatible bioinks make this technique a cost-efficient and accessible method. In the functionality spider chart of Fig. 5.1, it is evident that there is still room for enhancing the resolution and cell viability of the extrusion technique. Laser/light-based methods deliver excellent resolutions and cell viabilities. Specifically, the most suitable approach for printing multi-scale vascular structures is perhaps vat-polymerization. A critical drawback of the current multi-material vat-polymerization techniques is the risk of cross-contamination, which could be a potential direction for future endeavors.

One possible improvement to the current technologies of biofabrication is to move toward fabricating heterogeneous tissue constructs, which mimic the structure of the native tissue more realistically. The main tool to achieve this goal is to improve multi-material bioprinting technologies. Multi-material bioprinters outperform their single-material counterparts in fabricating heterogenous/multi-cellular tissue constructs. As illustrated in Fig. 5.2, several improvements are envisioned to overcome the current limitations in multi-material bioprinting.

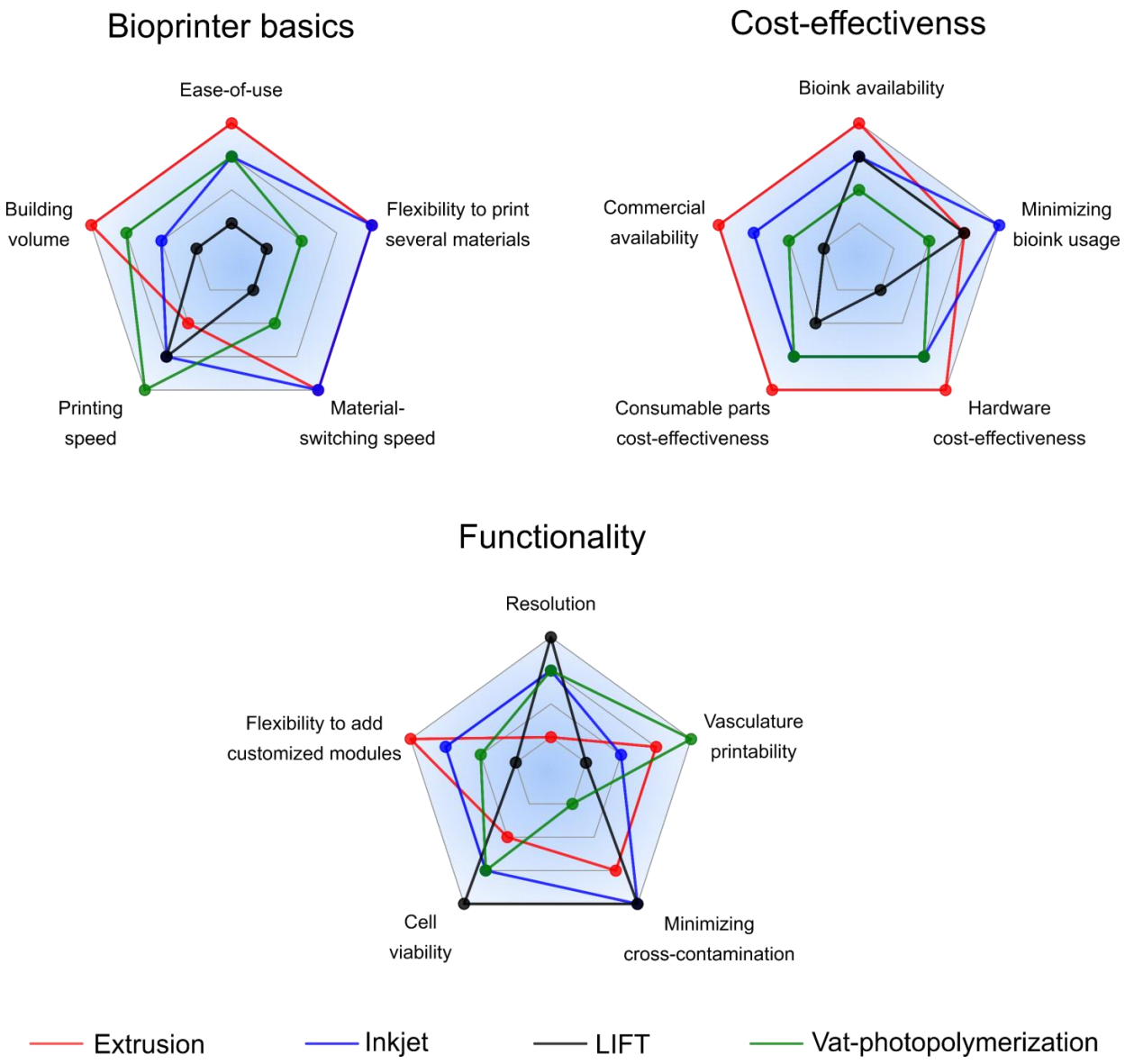

Fig. 5.1. Comparison of the four primary bioprinting technologies in different aspects. Features are ranked in four levels with the outer level presenting the highest score.

One challenge faced by most existing multi-material bioprinting technologies is to scale-up the printing volume to clinically relevant sizes within a reasonable fabrication time. For

instance, with a typical extrusion-based bioprinter, it can take hours to even days to create an entire multi-cellular organ structure with a decent resolution. Such a long fabrication process keeps the cells away from physiological conditions and significantly decreases the cell viability in the fabricated cell-laden constructs. Embedded bioprinting can possibly alleviate this concern for mid-sized organs to some extent since cells stay in a humidified environment. Yet, bioprinted full-sized organs with high cell viability have not been reported so far with embedded bioprinting. Other designs such as multi-nozzle printheads have also been explored [240], but they are mainly suitable for creating repeating patterns.

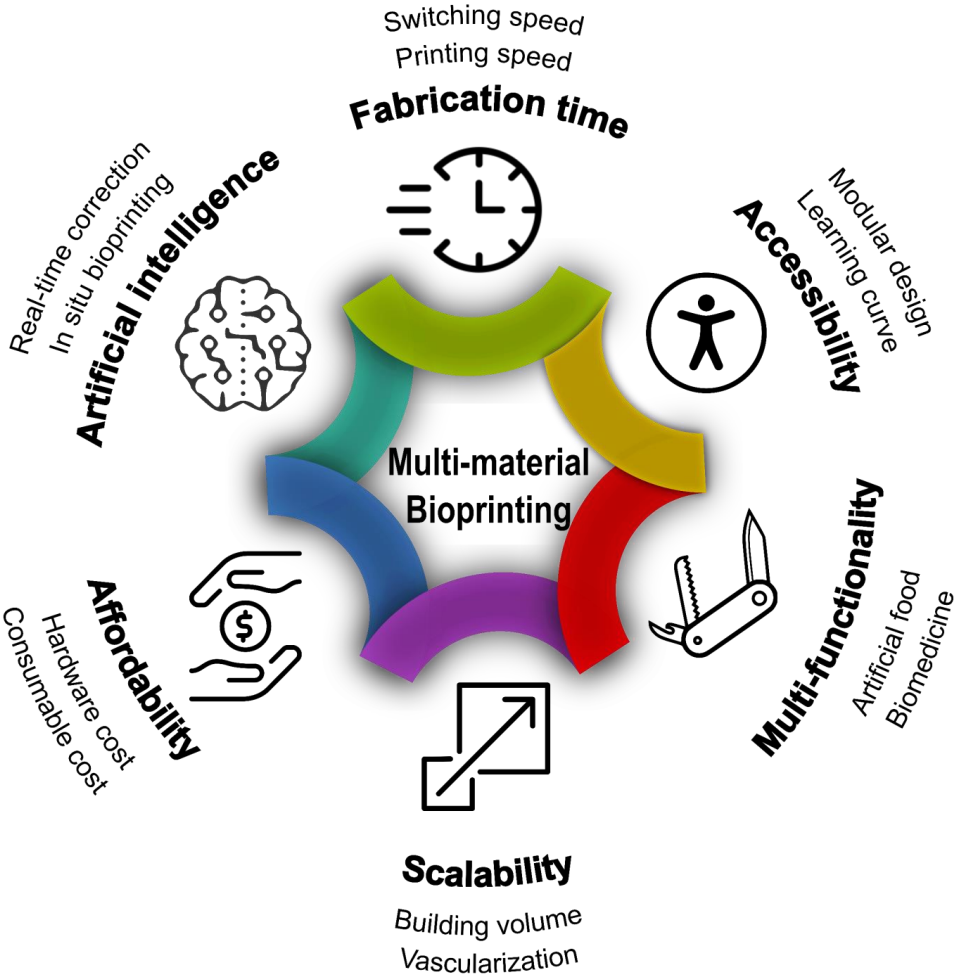

Fig. 5.2. Future perspective of potential improvements in multi-material bioprinting.

Large-scale bioprinting has higher chances to introduce defects, such as bubbles and voids. The involvement of multiple materials further impedes the quality control for layer-by-layer methods, leading to a low success rate for production. Such complications are mainly due to the relatively unstable properties of soft bioinks. Although the defects are difficult to avoid or predict, they are usually easy to detect during the printing process. Machine-learning approaches have been recently employed to enhance the printing quality [241]. By introducing artificial intelligence (AI), bioprinting on dynamically moving substrates, such as breathing lungs, has been successfully demonstrated [242, 242, 243]. With the assistance of AI in conjunction with computer vision, substrate height, printing pressure, or writing speed can be dynamically adjusted to correct the defects and errors, yielding better printing quality [241].

Application-wise, multi-material bioprinting may be employed to further improve the current single-material designs through the use of sacrificial inks. For instance, tubular vessel-like constructs may be fabricated using a sacrificial material as the core ink [244]. Generally, the fabrication of vascularized constructs can be fostered by effectively exploiting multi-material bioprinting of bioinks and sacrificial inks. Another unique perspective in bioprinting is integrating multi-material technologies in 4D bioprinting, a method to use stimuli-responsive materials as the bioink [245–247]. Multi-material bioprinters can accommodate the use of multiple smart bioinks to fabricate multi-functional stimuli-responsive constructs.

The accessibility of commercial multi-material bioprinters has motivated many researchers from different fields to leverage this technology for desirable tissue engineering applications without spending time and resources on the production of bioprinters. Previously, multi-material technologies were mostly limited to biomedical engineering labs with essential engineering backgrounds for its development. Most commercial bioprinters are based on the extrusion technique due to its simplicity and affordability. There is still an unmet need for commercial multi-material LIFT and vat-polymerization bioprinters to make these technologies accessible and available to more research labs, where they can be used for cutting-edge applications. The cost barrier and the complexity of the LIFT bioprinting method are the main challenges in commercializing this method.

Looking into the future, the development of hybrid bioprinters comprising multi-material modules can be anticipated. With the aid of various parallel modules, different tissue parts can be fabricated and assembled to form a complete and functional whole-size organ. An

exploratory 3D printer combining an aerosol jet head, a photonic cure head, extrusion modules, and inkjet heads has been recently reported to create complex structures with high precision [248]. Hybrid bioprinters comprising molten material extrusion and stereolithography modules has also been used to print soft hydrogels and thermoplastics simultaneously [249]. Such a combination is favorable to fabricate cell-laden constructs with gradients and high mechanical strength. Other works such as manual [250] or robotic [251] mini-tissue assemblies also prove the feasibility of modular tissue fabrication.

Significant advances in multi-material bioprinting technologies have been achieved over the last two decades. However, synergetic efforts on developing bioprinting techniques, bioinks, and gantries are still needed to realize the full potential of these technologies. Multi-disciplinary research and collaborations between academic research and industries will be crucial to bringing multi-material bioprinting technologies into clinical use.

Bibliography

[1] H. Ravanbakhsh, G. Bao, N. Latifi, L. G. Mongeau, Carbon nanotube composite hydrogels for vocal fold tissue engineering: Biocompatibility, rheology, and porosity, Materials Science and Engineering: C 103 (2019) 109861.

[2] H. Ravanbakhsh, G. Bao, L. Mongeau, Carbon nanotubes promote cell migration in hydrogels, Scientific reports 10 (2020) 1–10.

[3] H. Ravanbakhsh, G. Bao, Z. Luo, L. G. Mongeau, Y. S. Zhang, Composite inks for extrusion printing of biological and biomedical constructs, ACS Biomaterials Science & Engineering (2020).

[4] D. J. Munoz-Pinto, A. C. Jimenez-Vergara, T. P. Gharat, M. S. Hahn, Characterization of sequential collagen-poly (ethylene glycol) diacrylate interpenetrating networks and initial assessment of their potential for vascular tissue engineering, Biomaterials 40 (2015) 32–42.

[5] A. Vedadghavami, F. Minooei, M. H. Mohammadi, S. Khetani, A. R. Kolahchi, S. Mashayekhan, A. Sanati-Nezhad, Manufacturing of hydrogel biomaterials with controlled mechanical properties for tissue engineering applications, Acta biomaterialia 62 (2017) 42–63.

[6] G. Bao, T. Jiang, H. Ravanbakhsh, A. Reyes, Z. Ma, M. Strong, H. Wang, J. M. Kinsella, J. Li, L. Mongeau, Triggered micropore-forming bioprinting of porous viscoelastic hydrogels, Materials Horizons 7 (2020) 2336–2347.

[7] G. Ying, N. Jiang, C. Parra-Cantu, G. Tang, J. Zhang, H. Wang, S. Chen, N.-P. Huang, J. Xie, Y. S. Zhang, Bioprinted injectable hierarchically porous gelatin methacryloyl hydrogel constructs with shape-memory properties, Advanced Functional Materials 30 (2020) 2003740.

[8] A. S. Gladman, E. A. Matsumoto, R. G. Nuzzo, L. Mahadevan, J. A. Lewis, Biomimetic 4d printing, Nature materials 15 (2016) 413–418.

[9] Y. S. Zhang, A. Khademhosseini, Advances in engineering hydrogels, Science 356 (2017).

[10] R. Edri, I. Gal, N. Noor, T. Harel, S. Fleischer, N. Adadi, O. Green, D. Shabat, L. Heller, A. Shapira, et al., Personalized hydrogels for engineering diverse fully autologous tissue implants, Advanced materials 31 (2019) 1803895.

[11] G. Tang, L. Chen, L. Lian, F. Li, H. Ravanbakhsh, M. Wang, Y. S. Zhang, C. Huang, Designable dual-power micromotors fabricated from a biocompatible gas-shearing strategy, Chemical Engineering Journal 407 (2021) 127187.

[12] Q. Qu, J. Zhang, X. Chen, H. Ravanbakhsh, G. Tang, R. Xiong, B. B. Manshian, S. J. Soenen, F. Sauvage, K. Braeckmans, et al., Triggered release from cellulose microparticles inspired by wood degradation by fungi, ACS Sustainable Chemistry & Engineering (2020).

[13] A. Pacifici, L. Laino, M. Gargari, F. Guzzo, A. V. Luz, A. Polimeni, L. Pacifici, Decellularized hydrogels in bone tissue engineering: a topical review, International journal of medical sciences 15 (2018) 492.

[14] D. Loessner, C. Meinert, E. Kaemmerer, L. C. Martine, K. Yue, P. A. Levett, T. J. Klein, F. P. Melchels, A. Khademhosseini, D. W. Hutmacher, Functionalization, preparation and use of cell-laden gelatin methacryloyl–based hydrogels as modular tissue culture platforms, Nature protocols 11 (2016) 727.

[15] P. A. DiMilla, K. Barbee, D. A. Lauffenburger, Mathematical model for the effects of adhesion and mechanics on cell migration speed, Biophysical journal 60 (1991) 15–37.

[16] L. C. Bahlmann, L. J. Smith, M. S. Shoichet, Designer biomaterials to model cancer cell invasion in vitro: predictive tools or just pretty pictures?, Advanced Functional Materials 30 (2020) 1909032.

[17] R. S. Lakes, Composite biomaterials, Biomaterials: Principles and Applications, ed. JB Park and JD Bronzino, CRC Press, Boca Raton, FL, (2003) 79.

[18] Y. Zhang, L. Czerwonka, C. Tao, J. J. Jiang, A biphasic theory for the viscoelastic behaviors of vocal fold lamina propria in stress relaxation, The Journal of the Acoustical Society of America 123 (2008) 1627–1636.

[19] B. Li, T. Webster, Orthopedic biomaterials: advances and applications, Springer, 2018.

[20] K. K. Moncal, D. N. Heo, K. P. Godzik, D. M. Sosnoski, O. D. Mrowczynski, E. Rizk, V. Ozbolat, S. M. Tucker, E. M. Gerhard, M. Dey, et al., 3d printing of poly (ε-caprolactone)/poly (d, l-lactide-co-glycolide)/hydroxyapatite composite constructs for bone tissue engineering, Journal of Materials Research 33 (2018) 1972–1986.

[21] K. Jakab, C. Norotte, B. Damon, F. Marga, A. Neagu, C. L. Besch-Williford, A. Kachurin, K. H. Church, H. Park, V. Mironov, et al., Tissue engineering by self-assembly of cells printed into topologically defined structures, Tissue Engineering Part A 14 (2008) 413–421.

[22] D. Nguyen, D. A. Hägg, A. Forsman, J. Ekholm, P. Nimkingratana, C. Brantsing, T. Kalogeropoulos, S. Zaunz, S. Concaro, M. Brittberg, et al., Cartilage tissue engineering by the 3d bioprinting of ips cells in a nanocellulose/alginate bioink, Scientific reports 7 (2017) 1–10.

[23] Y. Huang, X.-F. Zhang, G. Gao, T. Yonezawa, X. Cui, 3d bioprinting and the current applications in tissue engineering, Biotechnology journal 12 (2017) 1600734.

[24] P. Kamali, S. J. Lin, Reply: The current role of three-dimensional printing in plastic surgery, Plastic and reconstructive surgery 139 (2017) 812e–813e.

[25] Y. Zhang, Y. Yu, I. T. Ozbolat, Direct bioprinting of vessel-like tubular microfluidic channels, Journal of nanotechnology in engineering and medicine 4 (2013).

[26] W. Sun, B. Starly, A. C. Daly, J. A. Burdick, J. Groll, G. Skeldon, W. Shu, Y. Sakai, M. Shinohara, M. Nishikawa, et al., The bioprinting roadmap, Biofabrication 12 (2020) 022002.

[27] H. Yuk, B. Lu, S. Lin, K. Qu, J. Xu, J. Luo, X. Zhao, 3d printing of conducting polymers, Nature communications 11 (2020) 1–8.

[28] A. Skardal, S. V. Murphy, M. Devarasetty, I. Mead, H.-W. Kang, Y.-J. Seol, Y. S. Zhang, S.-R. Shin, L. Zhao, J. Aleman, et al., Multi-tissue interactions in an integrated three-tissue organ-on-a-chip platform, Scientific reports 7 (2017) 1–16.

[29] Y. S. Zhang, A. Arneri, S. Bersini, S.-R. Shin, K. Zhu, Z. Goli-Malekabadi, J. Aleman, C. Colosi, F. Busignani, V. Dell'Erba, et al., Bioprinting 3d microfibrous scaffolds for engineering endothelialized myocardium and heart-on-a-chip, Biomaterials 110 (2016) 45–59.

[30] X. Ma, J. Liu, W. Zhu, M. Tang, N. Lawrence, C. Yu, M. Gou, S. Chen, 3d bioprinting of functional tissue models for personalized drug screening and in vitro disease modeling, Advanced drug delivery reviews 132 (2018) 235–251.

[31] J. Guo, R. Zhang, L. Zhang, X. Cao, 4d printing of robust hydrogels consisted of agarose nanofibers and polyacrylamide, ACS Macro Letters 7 (2018) 442–446.

[32] B. A. Nerger, P.-T. Brun, C. M. Nelson, Microextrusion printing cell-laden networks of type i collagen with patterned fiber alignment and geometry, Soft matter 15 (2019) 5728–5738.

[33] N. Schaefer, D. Janzen, E. Bakirci, A. Hrynevich, P. D. Dalton, C. Villmann, 3d electrophysiological measurements on cells embedded within fiber-reinforced matrigel, Advanced healthcare materials 8 (2019) 1801226.

[34] R. Fan, M. Piou, E. Darling, D. Cormier, J. Sun, J. Wan, Bio-printing cell-laden matrigel–agarose constructs, Journal of biomaterials applications 31 (2016) 684–692.

[35] Z. Ding, C. Yuan, X. Peng, T. Wang, H. J. Qi, M. L. Dunn, Direct 4d printing via active composite materials, Science advances 3 (2017) e1602890.

[36] M. C. Mulakkal, R. S. Trask, V. P. Ting, A. M. Seddon, Responsive cellulose-hydrogel composite ink for 4d printing, Materials & Design 160 (2018) 108–118.

[37] T.-S. Jang, H.-D. Jung, M. H. Pan, W. T. Han, S. Chen, J. Song, 3d printing of hydrogel composite systems: Recent advances in technology for tissue engineering (2018).

[38] Y. Jin, Y. Shen, J. Yin, J. Qian, Y. Huang, Nanoclay-based self-supporting responsive nanocomposite hydrogels for printing applications, ACS applied materials & interfaces 10 (2018) 10461–10470.

[39] P. Balasubramanian, M. P. Prabhakaran, M. Sireesha, S. Ramakrishna, Collagen in human tissues: structure, function, and biomedical implications from a tissue engineering perspective, in: Polymer Composites–Polyolefin Fractionation–Polymeric Peptidomimetics–Collagens, Springer, 2012, pp. 173–206.

[40] A. J. Heim, W. G. Matthews, T. J. Koob, Determination of the elastic modulus of native collagen fibrils via radial indentation, Applied physics letters 89 (2006) 181902.

[41] W. Li, J. Sigley, M. Pieters, C. C. Helms, C. Nagaswami, J. W. Weisel, M. Guthold, Fibrin fiber stiffness is strongly affected by fiber diameter, but not by fibrinogen glycation, Biophysical journal 110 (2016) 1400–1410.

[42] I. V. Roberts, D. Bukhary, C. Y. L. Valdivieso, N. Tirelli, Fibrin matrices as (injectable) biomaterials: Formation, clinical use, and molecular engineering, Macromolecular Bioscience 20 (2020) 1900283.

[43] J.-P. Collet, H. Shuman, R. E. Ledger, S. Lee, J. W. Weisel, The elasticity of an individual fibrin fiber in a clot, Proceedings of the National Academy of Sciences 102 (2005) 9133–9137.

[44] I. Usov, G. Nyström, J. Adamcik, S. Handschin, C. Schütz, A. Fall, L. Bergström, R. Mezzenga, Understanding nanocellulose chirality and structure–properties relationship at the single fibril level, Nature communications 6 (2015) 1–11.

[45] K. J. De France, T. Hoare, E. D. Cranston, Review of hydrogels and aerogels containing nanocellulose, Chemistry of Materials 29 (2017) 4609–4631.

[46] K. De France, Z. Zeng, T. Wu, G. Nyström, Functional materials from nanocellulose: Utilizing structure–property relationships in bottom-up fabrication, Advanced Materials (2020) 2000657.

[47] N. Lin, A. Dufresne, Nanocellulose in biomedicine: Current status and future prospect, European Polymer Journal 59 (2014) 302–325.

[48] M. M. Pereira, N. Raposo, R. Brayner, E. Teixeira, V. Oliveira, C. C. R. Quintão, L. Camargo, L. Mattoso, H. Brandão, Cytotoxicity and expression of genes involved in the cellular stress response and apoptosis in mammalian fibroblast exposed to cotton cellulose nanofibers, Nanotechnology 24 (2013) 075103.

[49] B. Nazari, V. Kumar, D. W. Bousfield, M. Toivakka, Rheology of cellulose nanofibers suspensions: boundary driven flow, Journal of Rheology 60 (2016) 1151–1159.

[50] R. J. Crawford, K. J. Edler, S. Lindhoud, J. L. Scott, G. Unali, Formation of shear thinning gels from partially oxidised cellulose nanofibrils, Green chemistry 14 (2012) 300–303.

[51] M. J. Treacy, T. W. Ebbesen, J. M. Gibson, Exceptionally high young's modulus observed for individual carbon nanotubes, nature 381 (1996) 678–680.

[52] S. Agarwala, G. L. Goh, G. D. Goh, V. Dikshit, W. Y. Yeong, 3d and 4d printing of polymer/cnts-based conductive composites, in: 3D and 4D Printing of Polymer Nanocomposite Materials, Elsevier, 2020, pp. 297–324.

[53] C. Marques, G. Diogo, S. Pina, J. M. Oliveira, T. Silva, R. Reis, Collagen-based bioinks for hard tissue engineering applications: a comprehensive review, Journal of Materials Science: Materials in Medicine 30 (2019) 1–12.

[54] M. D. Shoulders, R. T. Raines, Collagen structure and stability, Annual review of biochemistry 78 (2009) 929–958.

[55] C. A. Grant, D. J. Brockwell, S. E. Radford, N. H. Thomson, Effects of hydration on the mechanical response of individual collagen fibrils, Applied Physics Letters 92 (2008) 233902.

[56] A. Ozcelikkale, B. Han, Thermal destabilization of collagen matrix hierarchical structure by freeze/thaw, PloS one 11 (2016) e0146660.

[57] N. Davidenko, C. F. Schuster, D. V. Bax, R. W. Farndale, S. Hamaia, S. M. Best, R. E. Cameron, Evaluation of cell binding to collagen and gelatin: a study of the effect of 2d and 3d architecture and surface chemistry, Journal of Materials Science: Materials in Medicine 27 (2016) 148.

[58] K. K. Moncal, V. Ozbolat, P. Datta, D. N. Heo, I. T. Ozbolat, Thermally-controlled extrusion-based bioprinting of collagen, Journal of Materials Science: Materials in Medicine 30 (2019) 55.

[59] W. Kim, G. Kim, Collagen/bioceramic-based composite bioink to fabricate a porous 3d hascs-laden structure for bone tissue regeneration, Biofabrication 12 (2019) 015007.

[60] C. M. Homenick, G. de Silveira, H. Sheardown, A. Adronov, Pluronics as crosslinking agents for collagen: novel amphiphilic hydrogels, Polymer International 60 (2011) 458–465.

[61] H. Heidari, H. Taylor, Multilayered microcasting of agarose–collagen composites for neurovascular modeling, Bioprinting 17 (2020) e00069.

[62] S. Choy, D. V. Lam, S.-M. Lee, D. S. Hwang, Prolonged biodegradation and improved mechanical stability of collagen via vapor-phase ti stitching for long-term tissue regeneration, ACS applied materials & interfaces 11 (2019) 38440–38447.

[63] W. Li, J. Sigley, S. R. Baker, C. C. Helms, M. T. Kinney, M. Pieters, P. H. Brubaker, R. Cubcciotti, M. Guthold, Nonuniform internal structure of fibrin fibers: protein density and bond density strongly decrease with increasing diameter, BioMed research international 2017 (2017).

[64] N. Laurens, P. d. Koolwijk, M. De Maat, Fibrin structure and wound healing, Journal of Thrombosis and Haemostasis 4 (2006) 932–939.

[65] M. Pieters, A. S. Wolberg, Fibrinogen and fibrin: An illustrated review, Research and practice in thrombosis and haemostasis 3 (2019) 161–172.

[66] W. Liu, L. Jawerth, E. Sparks, M. Falvo, R. Hantgan, R. Superfine, S. Lord, M. Guthold, Fibrin fibers have extraordinary extensibility and elasticity, Science 313 (2006) 634–634.

[67] O. S. Manoukian, N. Sardashti, T. Stedman, K. Gailiunas, A. Ojha, A. Penalosa, C. Mancuso, M. Hobert, S. G. Kumbar, Biomaterials for tissue engineering and regenerative medicine (2019).

[68] J. E. Pomeroy, A. Helfer, N. Bursac, Biomaterializing the promise of cardiac tissue engineering, Biotechnology advances (2019).

[69] R. I. Litvinov, J. W. Weisel, Fibrin mechanical properties and their structural origins, Matrix Biology 60 (2017) 110–123.

[70] A. Mohandas, W. Sun, T. Nimal, S. A. Shankarappa, N. S. Hwang, R. Jayakumar, Injectable chitosan-fibrin/nanocurcumin composite hydrogel for the enhancement of angiogenesis, Research on Chemical Intermediates 44 (2018) 4873–4887.

[71] T. Heinze, Cellulose: structure and properties, in: Cellulose chemistry and properties: fibers, nanocelluloses and advanced materials, Springer, 2015, pp. 1–52.

[72] L. He, A. Karumuri, S. M. Mukhopadhyay, Wettability tailoring of nanotube carpets: morphology-chemistry synergy for hydrophobic–hydrophilic cycling, RSC advances 7 (2017) 25265–25275.

[73] M. E. Van den Berg, S. Kuster, E. J. Windhab, J. Adamcik, R. Mezzenga, T. Geue, L. M. Sagis, P. Fischer, Modifying the contact angle of anisotropic cellulose nanocrystals: Effect on interfacial rheology and structure, Langmuir 34 (2018) 10932–10942.

[74] H.-M. Ng, L. T. Sin, T.-T. Tee, S.-T. Bee, D. Hui, C.-Y. Low, A. Rahmat, Extraction of cellulose nanocrystals from plant sources for application as reinforcing agent in polymers, Composites Part B: Engineering 75 (2015) 176–200.

[75] I. A. Sacui, R. C. Nieuwendaal, D. J. Burnett, S. J. Stranick, M. Jorfi, C. Weder, E. J. Foster, R. T. Olsson, J. W. Gilman, Comparison of the properties of cellulose nanocrystals and cellulose nanofibrils isolated from bacteria, tunicate, and wood processed using acid, enzymatic, mechanical, and oxidative methods, ACS applied materials & interfaces 6 (2014) 6127–6138.

[76] S. Sultan, A. P. Mathew, 3d printed scaffolds with gradient porosity based on a cellulose nanocrystal hydrogel, Nanoscale 10 (2018) 4421–4431.

[77] K. Tashiro, M. Kobayashi, Theoretical evaluation of three-dimensional elastic constants of native and regenerated celluloses: role of hydrogen bonds, Polymer 32 (1991) 1516–1526.

[78] E. B. Heggset, B. L. Strand, K. W. Sundby, S. Simon, G. Chinga-Carrasco, K. Syverud, Viscoelastic properties of nanocellulose based inks for 3d printing and mechanical properties of cnf/alginate biocomposite gels, Cellulose 26 (2019) 581–595.

[79] J. Wang, A. Chiappone, I. Roppolo, F. Shao, E. Fantino, M. Lorusso, D. Rentsch, K. Dietliker, C. F. Pirri, H. Grützmacher, All-in-one cellulose nanocrystals for 3d printing of nanocomposite hydrogels, Angewandte Chemie International Edition 57 (2018) 2353–2356.

[80] J. S. Gonzalez, L. N. Ludueña, A. Ponce, V. A. Alvarez, Poly (vinyl alcohol)/cellulose nanowhiskers nanocomposite hydrogels for potential wound dressings, Materials Science and Engineering: C 34 (2014) 54–61.

[81] M. Müller, E. Öztürk, Ø. Arlov, P. Gatenholm, M. Zenobi-Wong, Alginate sulfate–nanocellulose bioinks for cartilage bioprinting applications, Annals of biomedical engineering 45 (2017) 210–223.

[82] Y. Chen, W. Xu, W. Liu, G. Zeng, Responsiveness, swelling, and mechanical properties of pnipa nanocomposite hydrogels reinforced by nanocellulose, Journal of Materials Research 30 (2015) 1797.

[83] S. S. Athukoralalage, R. Balu, N. K. Dutta, N. Roy Choudhury, 3d bioprinted nanocellulose-based hydrogels for tissue engineering applications: A brief review, Polymers 11 (2019) 898.

[84] G. Chinga-Carrasco, Potential and limitations of nanocelluloses as components in biocomposite inks for three-dimensional bioprinting and for biomedical devices, Biomacromolecules 19 (2018) 701–711.

[85] S. Iijima, Helical microtubules of graphitic carbon, nature 354 (1991) 56–58.

[86] I. A. Kinloch, J. Suhr, J. Lou, R. J. Young, P. M. Ajayan, Composites with carbon nanotubes and graphene: An outlook, Science 362 (2018) 547–553.

[87] N. Gupta, S. M. Gupta, S. Sharma, Carbon nanotubes: synthesis, properties and engineering applications, Carbon Letters (2019) 1–29.

[88] H.-B. Kim, D. K. Patel, Y.-R. Seo, K.-T. Lim, 3d-printed scaffolds with reinforced poly (lactic acid)/carbon nanotube filaments based on melt extrusion, Journal of Biosystems Engineering 44 (2019) 120–127.

[89] G. D. Goh, Y. L. Yap, S. Agarwala, W. Y. Yeong, Recent progress in additive manufacturing of fiber reinforced polymer composite, Advanced Materials Technologies 4 (2019) 1800271.

[90] Y. Yang, Z. Chen, X. Song, Z. Zhang, J. Zhang, K. K. Shung, Q. Zhou, Y. Chen, Biomimetic anisotropic reinforcement architectures by electrically assisted nanocomposite 3d printing, Advanced materials 29 (2017) 1605750.

[91] C. M. B. Ho, A. Mishra, P. T. P. Lin, S. H. Ng, W. Y. Yeong, Y.-J. Kim, Y.-J. Yoon, 3d printed polycaprolactone carbon nanotube composite scaffolds for cardiac tissue engineering, Macromolecular bioscience 17 (2017) 1600250.

[92] A. Razzazan, F. Atyabi, B. Kazemi, R. Dinarvand, In vivo drug delivery of gemcitabine with pegylated single-walled carbon nanotubes, Materials Science and Engineering: C 62 (2016) 614–625.

[93] S. Zhang, M. Xing, B. Li, Recent advances in musculoskeletal local drug delivery, Acta Biomaterialia 93 (2019) 135–151.

[94] M. Dresselhaus, Y. Lin, O. Rabin, A. Jorio, A. Souza Filho, M. Pimenta, R. Saito, G. Samsonidze, G. Dresselhaus, Nanowires and nanotubes, Materials Science and Engineering: C 23 (2003) 129–140.

[95] T. Distler, A. R. Boccaccini, 3d printing of electrically conductive hydrogels for tissue engineering and biosensors–a review, Acta Biomaterialia 101 (2020) 1–13.

[96] S. R. Shin, R. Farzad, A. Tamayol, V. Manoharan, P. Mostafalu, Y. S. Zhang, M. Akbari, S. M. Jung, D. Kim, M. Comotto, et al., A bioactive carbon nanotube-based ink for printing 2d and 3d flexible electronics, Advanced Materials 28 (2016) 3280–3289.

[97] K. Gnanasekaran, T. Heijmans, S. Van Bennekom, H. Woldhuis, S. Wijnia, G. de With, H. Friedrich, 3d printing of cnt-and graphene-based conductive polymer nanocomposites by fused deposition modeling, Applied materials today 9 (2017) 21–28.

[98] F. V. Ferreira, L. D. S. Cividanes, F. S. Brito, B. R. C. de Menezes, W. Franceschi, E. A. N. Simonetti, G. P. Thim, Functionalization of carbon nanotube and applications, in: Functionalizing Graphene and Carbon Nanotubes, Springer, 2016, pp. 31–61.

[99] A. Abo-Hamad, M. Hayyan, M. A. AlSaadi, M. E. Mirghani, M. A. Hashim, Functionalization of carbon nanotubes using eutectic mixtures: A promising route for enhanced aqueous dispersibility and electrochemical activity, Chemical Engineering Journal 311 (2017) 326–339.

[100] K. Z. Milowska, M. Burda, L. Wolanicka, P. D. Bristowe, K. K. Koziol, Carbon nanotube functionalization as a route to enhancing the electrical and mechanical properties of cu–cnt composites, Nanoscale 11 (2019) 145–157.

[101] S. Smart, A. Cassady, G. Lu, D. Martin, The biocompatibility of carbon nanotubes, Carbon 44 (2006) 1034–1047.

[102] M. Bhattacharya, W.-J. Seong, Carbon nanotube-based materials—preparation, biocompatibility, and applications in dentistry, in: Nanobiomaterials in Clinical Dentistry, Elsevier, 2019, pp. 41–76.

[103] M. Landry, M. Pinault, S. Tchankouo, É. Charon, A. Ridoux, J. Boczkowski, M. Mayne-L'Hermite, S. Lanone, Early signs of multi-walled carbon nanotbues degradation in macrophages, via an intracellular ph-dependent biological mechanism; importance of length and functionalization, Particle and fibre toxicology 13 (2016) 1–12.

[104] M. Yang, M. Zhang, Biodegradation of carbon nanotubes by macrophages, Frontiers in Materials 6 (2019) 225.

[105] G. Modugno, F. Ksar, A. Battigelli, J. Russier, P. Lonchambon, E. E. da Silva, C. Ménard-Moyon, B. Soula, A.-M. Galibert, M. Pinault, et al., A comparative study on the enzymatic biodegradability of covalently functionalized double-and multi-walled carbon nanotubes, Carbon 100 (2016) 367–374.

[106] M. Chen, X. Qin, G. Zeng, Biodegradation of carbon nanotubes, graphene, and their derivatives, Trends in biotechnology 35 (2017) 836–846.

[107] M. Zhang, M. Yang, H. Nakajima, M. Yudasaka, S. Iijima, T. Okazaki, Diameter-dependent degradation of 11 types of carbon nanotubes: safety implications, ACS Applied Nano Materials 2 (2019) 4293–4301.

[108] J. M. Tan, P. Arulselvan, S. Fakurazi, H. Ithnin, M. Z. Hussein, A review on characterizations and biocompatibility of functionalized carbon nanotubes in drug delivery design, Journal of Nanomaterials 2014 (2014).

[109] F. M. Tonelli, A. K. Santos, K. N. Gomes, E. Lorencon, S. Guatimosim, L. O. Ladeira, R. R. Resende, Carbon nanotube interaction with extracellular matrix proteins producing scaffolds for tissue engineering, International journal of nanomedicine 7 (2012) 4511.

[110] K. Pulskamp, S. Diabaté, H. F. Krug, Carbon nanotubes show no sign of acute toxicity but induce intracellular reactive oxygen species in dependence on contaminants, Toxicology letters 168 (2007) 58–74.

[111] X. Liu, T. Walimbe, W. P. Schrock, W. Zheng, M. P. Sivasankar, Acute nanoparticle exposure to vocal folds: a laboratory study, Journal of Voice 31 (2017) 662–668.

[112] J. Muller, F. Huaux, N. Moreau, P. Misson, J.-F. Heilier, M. Delos, M. Arras, A. Fonseca, J. B. Nagy, D. Lison, Respiratory toxicity of multi-wall carbon nanotubes, Toxicology and applied pharmacology 207 (2005) 221–231.

[113] K. Werengowska-Ciećwierz, M. Wiśniewski, A. P. Terzyk, K. Roszek, J. Czarnecka, P. Bolibok, G. Rychlicki, Conscious changes of carbon nanotubes cytotoxicity by manipulation with selected nanofactors, Applied biochemistry and biotechnology 176 (2015) 730–741.

[114] Y. Lin, S. Taylor, H. Li, K. S. Fernando, L. Qu, W. Wang, L. Gu, B. Zhou, Y.-P. Sun, Advances toward bioapplications of carbon nanotubes, Journal of Materials Chemistry 14 (2004) 527–541.

[115] P. A. Tran, L. Zhang, T. J. Webster, Carbon nanofibers and carbon nanotubes in regenerative medicine, Advanced drug delivery reviews 61 (2009) 1097–1114.

[116] F. Liang, B. Chen, A review on biomedical applications of single-walled carbon nanotubes, Current medicinal chemistry 17 (2010) 10–24.

[117] R. Tekade, R. Maheshwari, N. Jain, Toxicity of nanostructured biomaterials, in: Nanobiomaterials, Elsevier, 2018, pp. 231–256.

[118] C. M. Sayes, F. Liang, J. L. Hudson, J. Mendez, W. Guo, J. M. Beach, V. C. Moore, C. D. Doyle, J. L. West, W. E. Billups, et al., Functionalization density dependence of single-walled carbon nanotubes cytotoxicity in vitro, Toxicology letters 161 (2006) 135–142.

[119] S. Vardharajula, S. Z. Ali, P. M. Tiwari, E. Eroğlu, K. Vig, V. A. Dennis, S. R. Singh, Functionalized carbon nanotubes: biomedical applications, International journal of nanomedicine 7 (2012) 5361.

[120] P. S. Kumar, N. M. Raj, G. Praveen, K. P. Chennazhi, S. V. Nair, R. Jayakumar, In vitro and in vivo evaluation of microporous chitosan hydrogel/nanofibrin composite bandage for skin tissue regeneration, Tissue Engineering Part A 19 (2013) 380–392.

[121] H. K. Heris, J. Daoud, S. Sheibani, H. Vali, M. Tabrizian, L. Mongeau, Investigation of the viability, adhesion, and migration of human fibroblasts in a hyaluronic acid/gelatin microgel-reinforced composite hydrogel for vocal fold tissue regeneration, Advanced healthcare materials 5 (2016) 255–265.

[122] A. S. Gobin, J. L. West, Effects of epidermal growth factor on fibroblast migration through biomimetic hydrogels, Biotechnology progress 19 (2003) 1781–1785.

[123] N. Latifi, M. Asgari, H. Vali, L. Mongeau, A tissue-mimetic nano-fibrillar hybrid injectable hydrogel for potential soft tissue engineering applications, Scientific reports 8 (2018) 1–18.

[124] M. Cavo, M. Caria, I. Pulsoni, F. Beltrame, M. Fato, S. Scaglione, A new cell-laden 3d alginate-matrigel hydrogel resembles human breast cancer cell malignant morphology, spread and invasion capability observed “in vivo”, Scientific reports 8 (2018) 1–12.

[125] K. M. Hakkinen, J. S. Harunaga, A. D. Doyle, K. M. Yamada, Direct comparisons of the morphology, migration, cell adhesions, and actin cytoskeleton of fibroblasts in four different three-dimensional extracellular matrices, Tissue Engineering Part A 17 (2011) 713–724.

[126] O. Chaudhuri, L. Gu, D. Klumpers, M. Darnell, S. A. Bencherif, J. C. Weaver, N. Huebsch, H.-p. Lee, E. Lippens, G. N. Duda, et al., Hydrogels with tunable stress relaxation regulate stem cell fate and activity, Nature materials 15 (2016) 326–334.

[127] L. Van den Broeck, S. Piluso, A. H. Soultan, M. De Volder, J. Patterson, Cytocompatible carbon nanotube reinforced polyethylene glycol composite hydrogels for tissue engineering, Materials Science and Engineering: C 98 (2019) 1133–1144.

[128] S. R. Shin, H. Bae, J. M. Cha, J. Y. Mun, Y.-C. Chen, H. Tekin, H. Shin, S. Farshchi, M. R. Dokmeci, S. Tang, et al., Carbon nanotube reinforced hybrid microgels as scaffold materials for cell encapsulation, ACS nano 6 (2012) 362–372.

[129] N. Cai, C. C. Wong, Y. X. Gong, S. C. Tan, V. Chan, K. Liao, Modulating cell adhesion dynamics on carbon nanotube monolayer engineered with extracellular matrix proteins, ACS applied materials & interfaces 2 (2010) 1038–1047.

[130] B. Gorain, H. Choudhury, M. Pandey, P. Kesharwani, M. M. Abeer, R. K. Tekade, Z. Hussain, Carbon nanotube scaffolds as emerging nanoplatform for myocardial tissue regeneration: a review of recent developments and therapeutic implications, Biomedicine & Pharmacotherapy 104 (2018) 496–508.

[131] M. Sheikholeslam, S. D. Wheeler, K. G. Duke, M. Marsden, M. Pritzker, P. Chen, Peptide and peptide-carbon nanotube hydrogels as scaffolds for tissue & 3d tumor engineering, Acta biomaterialia 69 (2018) 107–119.

[132] T. Schreier, E. Degen, W. Baschong, Fibroblast migration and proliferation during in vitro wound healing, Research in experimental medicine 193 (1993) 195–205.

[133] M. F. Cordeiro, S. S. Bhattacharya, G. S. Schultz, P. T. Khaw, Tgf-β1,-β2, and-β3 in vitro: biphasic effects on tenon's fibroblast contraction, proliferation, and migration, Investigative ophthalmology & visual science 41 (2000) 756–763.

[134] Y.-C. Chen, S. G. Allen, P. N. Ingram, R. Buckanovich, S. D. Merajver, E. Yoon, Single-cell migration chip for chemotaxis-based microfluidic selection of heterogeneous cell populations, Scientific reports 5 (2015) 1–13.

[135] M. L. De Ieso, J. V. Pei, An accurate and cost-effective alternative method for measuring cell migration with the circular wound closure assay, Bioscience reports 38 (2018).

[136] K. M. Wisdom, K. Adebowale, J. Chang, J. Y. Lee, S. Nam, R. Desai, N. S. Rossen, M. Rafat, R. B. West, L. Hodgson, et al., Matrix mechanical plasticity regulates cancer cell migration through confining microenvironments, Nature communications 9 (2018) 1–13.

[137] N. Kramer, A. Walzl, C. Unger, M. Rosner, G. Krupitza, M. Hengstschläger, H. Dolznig, In vitro cell migration and invasion assays, Mutation Research/Reviews in Mutation Research 752 (2013) 10–24.

[138] X. Li, X. Liu, W. Zhao, X. Wen, N. Zhang, Manipulating neural-stem-cell mobilization and migration in vitro, Acta biomaterialia 8 (2012) 2087–2095.

[139] Y. S. Zhang, R. Oklu, M. R. Dokmeci, A. Khademhosseini, Three-dimensional bioprinting strategies for tissue engineering, Cold Spring Harbor perspectives in medicine 8 (2018) a025718.

[140] P. N. Bernal, P. Delrot, D. Loterie, Y. Li, J. Malda, C. Moser, R. Levato, Volumetric bioprinting of complex living-tissue constructs within seconds, Advanced materials 31 (2019) 1904209.

[141] J. Li, C. Wu, P. K. Chu, M. Gelinsky, 3d printing of hydrogels: Rational design strategies and emerging biomedical applications, Materials Science and Engineering: R: Reports 140 (2020) 100543.

[142] S. Van Belleghem, L. Torres Jr, M. Santoro, B. Mahadik, A. Wolfand, P. Kofinas, J. P. Fisher, Hybrid 3d printing of synthetic and cell-laden bioinks for shape retaining soft tissue grafts, Advanced Functional Materials 30 (2020) 1907145.

[143] S. You, J. Li, W. Zhu, C. Yu, D. Mei, S. Chen, Nanoscale 3d printing of hydrogels for cellular tissue engineering, Journal of Materials Chemistry B 6 (2018) 2187–2197.

[144] S. Correia Carreira, R. Begum, A. W. Perriman, 3d bioprinting: the emergence of programmable biodesign, Advanced healthcare materials 9 (2020) 1900554.

[145] J. M. Lee, W. Y. Yeong, Design and printing strategies in 3d bioprinting of cell-hydrogels: A review, Advanced healthcare materials 5 (2016) 2856–2865.

[146] S. Freeman, R. Ramos, P. A. Chando, L. Zhou, K. Reeser, S. Jin, P. Soman, K. Ye, A bioink blend for rotary 3d bioprinting tissue engineered small-diameter vascular constructs, Acta biomaterialia 95 (2019) 152–164.

[147] S. Derakhshanfar, R. Mbeleck, K. Xu, X. Zhang, W. Zhong, M. Xing, 3d bioprinting for biomedical devices and tissue engineering: A review of recent trends and advances, Bioactive materials 3 (2018) 144–156.

[148] M. T. Poldervaart, B. Goversen, M. De Ruijter, A. Abbadessa, F. P. Melchels, F. C. Öner, W. J. Dhert, T. Vermonden, J. Alblas, 3d bioprinting of methacrylated hyaluronic acid (meha) hydrogel with intrinsic osteogenicity, PLoS One 12 (2017) e0177628.

[149] M. A. Skylar-Scott, S. G. Uzel, L. L. Nam, J. H. Ahrens, R. L. Truby, S. Damaraju, J. A. Lewis, Biomanufacturing of organ-specific tissues with high cellular density and embedded vascular channels, Science advances 5 (2019) eaaw2459.

[150] M. Kesti, C. Eberhardt, G. Pagliccia, D. Kenkel, D. Grande, A. Boss, M. Zenobi-Wong, Bioprinting complex cartilaginous structures with clinically compliant biomaterials, Advanced Functional Materials 25 (2015) 7406–7417.

[151] Y. S. Zhang, K. Yue, J. Aleman, K. Mollazadeh-Moghaddam, S. M. Bakht, J. Yang, W. Jia, V. Dell'Erba, P. Assawes, S. R. Shin, et al., 3d bioprinting for tissue and organ fabrication, Annals of biomedical engineering 45 (2017) 148–163.

[152] T. Jiang, J. G. Munguia-Lopez, S. Flores-Torres, J. Kort-Mascort, J. M. Kinsella, Extrusion bioprinting of soft materials: An emerging technique for biological model fabrication, Applied Physics Reviews 6 (2019) 011310.

[153] X. Li, J. Chen, B. Liu, X. Wang, D. Ren, T. Xu, A. Ovsianikov, J. Yoo, V. Mironov, Inkjet printing for biofabrication, 3D Printing and Biofabrication. Reference Series in Biomedical Engineering; Ovsianikov, A., Yoo, J., Mironov, V., Eds (2018) 1–19.

[154] P. Serra, A. Piqué, Laser-induced forward transfer: Fundamentals and applications, Advanced Materials Technologies 4 (2019) 1800099.

[155] H. Kumar, K. Kim, Stereolithography 3d bioprinting, in: 3D Bioprinting, Springer, 2020, pp. 93–108.

[156] J. Leijten, J. Seo, K. Yue, G. Trujillo-de Santiago, A. Tamayol, G. U. Ruiz-Esparza, S. R. Shin, R. Sharifi, I. Noshadi, M. M. Álvarez, et al., Spatially and temporally controlled hydrogels for tissue engineering, Materials Science and Engineering: R: Reports 119 (2017) 1–35.

[157] J. Jang, H.-J. Park, S.-W. Kim, H. Kim, J. Y. Park, S. J. Na, H. J. Kim, M. N. Park, S. H. Choi, S. H. Park, et al., 3d printed complex tissue construct using stem cell-laden decellularized extracellular matrix bioinks for cardiac repair, Biomaterials 112 (2017) 264–274.

[158] N. Ashammakhi, S. Ahadian, C. Xu, H. Montazerian, H. Ko, R. Nasiri, N. Barros, A. Khademhosseini, Bioinks and bioprinting technologies to make heterogeneous and biomimetic tissue constructs, Materials Today Bio 1 (2019) 100008.

[159] G. Ying, J. Manríquez, D. Wu, J. Zhang, N. Jiang, S. Maharjan, D. H. Medina, Y. Zhang, An open-source handheld extruder loaded with pore-forming bioink for in situ wound dressing, Materials Today Bio 8 (2020) 100074.

[160] R. Lozano, L. Stevens, B. C. Thompson, K. J. Gilmore, R. Gorkin III, E. M. Stewart, M. in het Panhuis, M. Romero-Ortega, G. G. Wallace, 3d printing of layered brain-like structures using peptide modified gellan gum substrates, Biomaterials 67 (2015) 264–273.

[161] N. Hakimi, R. Cheng, L. Leng, M. Sotoudehfar, P. Q. Ba, N. Bakhtyar, S. Amini-Nik, M. G. Jeschke, A. Günther, Handheld skin printer: in situ formation of planar biomaterials and tissues, Lab on a Chip 18 (2018) 1440–1451.

[162] C. Di Bella, S. Duchi, C. D. O'Connell, R. Blanchard, C. Augustine, Z. Yue, F. Thompson, C. Richards, S. Beirne, C. Onofrillo, et al., In situ handheld three-dimensional bioprinting for cartilage regeneration, Journal of tissue engineering and regenerative medicine 12 (2018) 611–621.

[163] E. Alarçin, T. Y. Lee, S. Karuthedom, M. Mohammadi, M. A. Brennan, D. H. Lee, A. Marrella, J. Zhang, D. Syla, Y. S. Zhang, et al., Injectable shear-thinning hydrogels for delivering osteogenic and angiogenic cells and growth factors, Biomaterials science 6 (2018) 1604–1615.

[164] I. T. Ozbolat, M. Hospodiuk, Current advances and future perspectives in extrusion-based bioprinting, Biomaterials 76 (2016) 321–343.

[165] W. Liu, M. A. Heinrich, Y. Zhou, A. Akpek, N. Hu, X. Liu, X. Guan, Z. Zhong, X. Jin, A. Khademhosseini, et al., Extrusion bioprinting of shear-thinning gelatin methacryloyl bioinks, Advanced healthcare materials 6 (2017) 1601451.

[166] Z. Wang, X. Jin, Z. Tian, F. Menard, J. F. Holzman, K. Kim, A novel, well-resolved direct laser bioprinting system for rapid cell encapsulation and microwell fabrication, Advanced healthcare materials 7 (2018) 1701249.

[167] L. Shi, Y. Hu, M. W. Ullah, H. Ou, W. Zhang, L. Xiong, X. Zhang, et al., Cryogenic free-form extrusion bioprinting of decellularized small intestinal submucosa for potential applications in skin tissue engineering, Biofabrication 11 (2019) 035023.

[168] C. D. O'Connell, S. Konate, C. Onofrillo, R. Kapsa, C. Baker, S. Duchi, T. Eekel, Z. Yue, S. Beirne, G. Barnsley, et al., Free-form co-axial bioprinting of a gelatin methacryloyl bio-ink by direct in situ photo-crosslinking during extrusion, Bioprinting 19 (2020) e00087.

[169] L. Shao, Q. Gao, C. Xie, J. Fu, M. Xiang, Y. He, Directly coaxial 3d bioprinting of large-scale vascularized tissue constructs, Biofabrication 12 (2020) 035014.

[170] G. Luo, Y. Yu, Y. Yuan, X. Chen, Z. Liu, T. Kong, Freeform, reconfigurable embedded printing of all-aqueous 3d architectures, Advanced Materials 31 (2019) 1904631.

[171] O. Jeon, Y. B. Lee, T. J. Hinton, A. W. Feinberg, E. Alsberg, Cryopreserved cell-laden alginate microgel bioink for 3d bioprinting of living tissues, Materials Today Chemistry 12 (2019) 61–70.

[172] G. Zhao, J. Fu, Microfluidics for cryopreservation, Biotechnology advances 35 (2017) 323–336.

[173] G. Zhao, X. Liu, K. Zhu, X. He, Hydrogel encapsulation facilitates rapid-cooling cryopreservation of stem cell-laden core–shell microcapsules as cell–biomaterial constructs, Advanced healthcare materials 6 (2017) 1700988.

[174] Y. S. Song, S. Moon, L. Hulli, S. K. Hasan, E. Kayaalp, U. Demirci, Microfluidics for cryopreservation, Lab on a Chip 9 (2009) 1874–1881.

[175] R. J. de Vries, P. D. Banik, S. Nagpal, L. Weng, S. Ozer, T. M. van Gulik, M. Toner, S. N. Tessier, K. Uygun, Bulk droplet vitrification: An approach to improve large-scale hepatocyte cryopreservation outcome, Langmuir 35 (2018) 7354–7363.

[176] Y. Akiyama, M. Shinose, H. Watanabe, S. Yamada, Y. Kanda, Cryoprotectant-free cryopreservation of mammalian cells by superflash freezing, Proceedings of the National Academy of Sciences 116 (2019) 7738–7743.

[177] S. Jiang, C. Lyu, P. Zhao, W. Li, W. Kong, C. Huang, G. M. Genin, Y. Du, Cryoprotectant enables structural control of porous scaffolds for exploration of cellular mechano-responsiveness in 3d, Nature communications 10 (2019) 1–14.

[178] H. Huang, G. Zhao, Y. Zhang, J. Xu, T. L. Toth, X. He, Predehydration and ice seeding in the presence of trehalose enable cell cryopreservation, ACS biomaterials science & engineering 3 (2017) 1758–1768.

[179] L. Bahari, A. Bein, V. Yashunsky, I. Braslavsky, Directional freezing for the cryopreservation of adherent mammalian cells on a substrate, PLoS One 13 (2018) e0192265.

[180] W. Stock, E. Pinseel, S. De Decker, J. Sefbom, L. Blommaert, O. Chepurnova, K. Sabbe, W. Vyverman, Expanding the toolbox for cryopreservation of marine and freshwater diatoms, Scientific reports 8 (2018) 1–9.

[181] A. von Bomhard, A. Elsässer, L. M. Ritschl, S. Schwarz, N. Rotter, Cryopreservation of endothelial cells in various cryoprotective agents and media–vitrification versus slow freezing methods, PLoS One 11 (2016) e0149660.

[182] A. C. Drake, Y. Lee, E. M. Burgess, J. O. Karlsson, A. Eroglu, A. Z. Higgins, Effect of water content on the glass transition temperature of mixtures of sugars, polymers, and penetrating cryoprotectants in physiological buffer, PloS one 13 (2018) e0190713.

[183] T. Z. An, M. Iwakiri, K. Edashige, T. Sakurai, M. Kasai, Factors affecting the survival of frozen–thawed mouse spermatozoa, Cryobiology 40 (2000) 237–249.

[184] J. Solocinski, Q. Osgood, M. Wang, A. Connolly, M. A. Menze, N. Chakraborty, Effect of trehalose as an additive to dimethyl sulfoxide solutions on ice formation, cellular viability, and metabolism, Cryobiology 75 (2017) 134–143.

[185] S. Tsai, G. Chong, P.-J. Meng, C. Lin, Sugars as supplemental cryoprotectants for marine organisms, Reviews in Aquaculture 10 (2018) 703–715.

[186] C. Malo, L. Gil, N. Gonzalez, R. Cano, I. De Blas, E. Espinosa, Comparing sugar type supplementation for cryopreservation of boar semen in egg yolk based extender, Cryobiology 61 (2010) 17–21.

[187] C. Silva, E. Cunha, G. Blume, J. Malaquias, S. Báo, C. Martins, Cryopreservation of boar sperm comparing different cryoprotectants associated in media based on powdered coconut water, lactose and trehalose, Cryobiology 70 (2015) 90–94.

[188] T. Hino, M. Takabe, R. Suzuki-Migishima, M. Yokoyama, Cryoprotective effects of various saccharides on cryopreserved mouse sperm from various strains, Reproductive medicine and biology 6 (2007) 229–233.

[189] A. Eroglu, Cryopreservation of mammalian oocytes by using sugars: intra-and extracellular raffinose with small amounts of dimethylsulfoxide yields high cryosurvival, fertilization, and development rates, Cryobiology 60 (2010) S54–S59.

[190] J. Gong, C. C. Schuurmans, A. M. van Genderen, X. Cao, W. Li, F. Cheng, J. J. He, A. López, V. Huerta, J. Manríquez, et al., Complexation-induced resolution enhancement of 3d-printed hydrogel constructs, Nature communications 11 (2020) 1–14.

[191] H. J. Yoon, S. R. Shin, J. M. Cha, S.-H. Lee, J.-H. Kim, J. T. Do, H. Song, H. Bae, Cold water fish gelatin methacryloyl hydrogel for tissue engineering application, PloS one 11 (2016) e0163902.

[192] A. M. Cole, H.-I. Liao, O. Stuchlik, J. Tilan, J. Pohl, T. Ganz, Cationic polypeptides are required for antibacterial activity of human airway fluid, The Journal of Immunology 169 (2002) 6985–6991.

[193] R. Sadeghi, P. Mahdavi, W. Lee, B. Quan, E. Sone, B. Ganss, C. McCulloch, A novel, cell-permeable, collagen-based membrane promotes fibroblast migration, Journal of periodontal research 53 (2018) 727–735.

[194] A. Adan, G. Alizada, Y. Kiraz, Y. Baran, A. Nalbant, Flow cytometry: basic principles and applications, Critical reviews in biotechnology 37 (2017) 163–176.

[195] L. A. Solchaga, K. J. Penick, J. F. Welter, Chondrogenic differentiation of bone marrow-derived mesenchymal stem cells: tips and tricks, in: Mesenchymal stem cell assays and applications, Springer, 2011, pp. 253–278.

[196] N. Mangir, S. Dikici, F. Claeyssens, S. MacNeil, Using ex ovo chick chorioallantoic membrane (cam) assay to evaluate the biocompatibility and angiogenic response to biomaterials, ACS Biomaterials Science & Engineering 5 (2019) 3190–3200.

[197] Y. Mousseau, S. Mollard, H. Qiu, L. Richard, R. Cazal, A. Nizou, N. Vedrenne, S. Rémi, Y. Baaj, L. Fourcade, et al., In vitro 3d angiogenesis assay in egg white matrix: comparison to matrigel, compatibility to various species, and suitability for drug testing, Laboratory investigation 94 (2014) 340–349.

[198] Y. Wu, M. A. Al-Ameen, G. Ghosh, Integrated effects of matrix mechanics and vascular endothelial growth factor (vegf) on capillary sprouting, Annals of biomedical engineering 42 (2014) 1024–1036.

[199] G. Cidonio, C. R. Alcala-Orozco, K. S. Lim, M. Glinka, I. Mutreja, Y.-H. Kim, J. I. Dawson, T. B. Woodfield, R. O. Oreffo, Osteogenic and angiogenic tissue formation in high fidelity nanocomposite laponite-gelatin bioinks, Biofabrication 11 (2019) 035027.

[200] S.-W. Choi, Y. Zhang, M. R. MacEwan, Y. Xia, Neovascularization in biodegradable inverse opal scaffolds with uniform and precisely controlled pore sizes, Advanced healthcare materials 2 (2013) 145–154.

[201] S. Kim, Z.-K. Cui, B. Koo, J. Zheng, T. Aghaloo, M. Lee, Chitosan–lysozyme conjugates for enzyme-triggered hydrogel degradation in tissue engineering applications, ACS applied materials & interfaces 10 (2018) 41138–41145.

[202] P. Rosen, D. S. Misfeldt, Cell density determines epithelial migration in culture, Proceedings of the National Academy of Sciences 77 (1980) 4760–4763.

[203] C. R. Kruse, M. Singh, S. Targosinski, I. Sinha, J. A. Sørensen, E. Eriksson, K. Nuutila, The effect of ph on cell viability, cell migration, cell proliferation, wound closure, and wound reepithelialization: In vitro and in vivo study, Wound Repair and Regeneration 25 (2017) 260–269.

[204] C. Ceccarini, H. Eagle, ph as a determinant of cellular growth and contact inhibition, Proceedings of the national academy of Sciences 68 (1971) 229–233.

[205] H. Park, K. Park, D. Kim, Preparation and swelling behavior of chitosan-based superporous hydrogels for gastric retention application, Journal of Biomedical Materials Research Part A: An Official Journal of The Society for Biomaterials, The Japanese Society for Biomaterials, and The Australian Society for Biomaterials and the Korean Society for Biomaterials 76 (2006) 144–150.

[206] E.-Y. Chuang, C.-W. Chiang, P.-C. Wong, C.-H. Chen, Hydrogels for the application of articular cartilage tissue engineering: A review of hydrogels, Advances in Materials Science and Engineering 2018 (2018).

[207] M. Ono, A. Masaki, A. Maeda, T. M. Kilts, E. S. Hara, T. Komori, H. Pham, T. Kuboki, M. F. Young, Ccn4/wisp1 controls cutaneous wound healing by modulating proliferation, migration and ecm expression in dermal fibroblasts via $\alpha 5\beta 1$ and tnfα, Matrix Biology 68 (2018) 533–546.

[208] T. L. Rosenberg, J. M. Schweinfurth, Cell density of the lamina propria of neonatal vocal folds, Annals of Otology, Rhinology & Laryngology 118 (2009) 87–90.

[209] G. Zajicek, R. Breuer, Cell kinetics of lamina propria fibroblasts in normal adult hamster bronchus, The Anatomical Record 233 (1992) 257–260.

[210] B. K. Mann, J. L. West, Cell adhesion peptides alter smooth muscle cell adhesion, proliferation, migration, and matrix protein synthesis on modified surfaces and in polymer scaffolds, Journal of biomedical materials research 60 (2002) 86–93.

[211] B. B. Mandal, S. C. Kundu, Cell proliferation and migration in silk fibroin 3d scaffolds, Biomaterials 30 (2009) 2956–2965.

[212] B. A. Harley, H.-D. Kim, M. H. Zaman, I. V. Yannas, D. A. Lauffenburger, L. J. Gibson, Microarchitecture of three-dimensional scaffolds influences cell migration behavior via junction interactions, Biophysical journal 95 (2008) 4013–4024.

[213] Y. Zhao, B. L. Allen, A. Star, Enzymatic degradation of multiwalled carbon nanotubes, The journal of physical chemistry A 115 (2011) 9536–9544.

[214] X. Zhao, N. Huebsch, D. J. Mooney, Z. Suo, Stress-relaxation behavior in gels with ionic and covalent crosslinks, Journal of applied physics 107 (2010) 063509.

[215] N. Savage, Thermoelectric coolers, Nature Photonics 3 (2009) 541–542.

[216] R. A. Kishore, A. Nozariasbmarz, B. Poudel, M. Sanghadasa, S. Priya, Ultra-high performance wearable thermoelectric coolers with less materials, Nature communications 10 (2019) 1–13.

[217] Y. Cheng, Y. Yu, Y. Zhang, G. Zhao, Y. Zhao, Cold-responsive nanocapsules enable the sole-cryoprotectant-trehalose cryopreservation of β cell–laden hydrogels for diabetes treatment, Small 15 (2019) 1904290.

[218] Y. Chen, Two sets of simple formulae to estimating fractal dimension of irregular boundaries, Mathematical Problems in Engineering 2020 (2020).

[219] G. D. Smith, S. Takayama, Cryopreservation and microfluidics: a focus on the oocyte, Reproduction, Fertility and Development 31 (2019) 93–104.

[220] W. Wu, A. DeConinck, J. A. Lewis, Omnidirectional printing of 3d microvascular networks, Advanced materials 23 (2011) H178–H183.

[221] C. B. Highley, C. B. Rodell, J. A. Burdick, Direct 3d printing of shear-thinning hydrogels into self-healing hydrogels, Advanced Materials 27 (2015) 5075–5079.

[222] T. Bhattacharjee, S. M. Zehnder, K. G. Rowe, S. Jain, R. M. Nixon, W. G. Sawyer, T. E. Angelini, Writing in the granular gel medium, Science advances 1 (2015) e1500655.

[223] T. J. Hinton, Q. Jallerat, R. N. Palchesko, J. H. Park, M. S. Grodzicki, H.-J. Shue, M. H. Ramadan, A. R. Hudson, A. W. Feinberg, Three-dimensional printing of complex biological structures by freeform reversible embedding of suspended hydrogels, Science advances 1 (2015) e1500758.

[224] D. L. Wright, A. Eroglu, M. Toner, T. L. Toth, Use of sugars in cryopreserving human oocytes, Reproductive BioMedicine Online 9 (2004) 179–186.

[225] N. Tada, M. Sato, J. Yamanoi, T. Mizorogi, K. Kasai, S. Ogawa, Cryopreservation of mouse spermatozoa in the presence of raffinose and glycerol, Reproduction 89 (1990) 511–516.

[226] Y. H. Yoon, J. M. Pope, J. Wolfe, The effects of solutes on the freezing properties of and hydration forces in lipid lamellar phases, Biophysical journal 74 (1998) 1949–1965.

[227] T. H. Jang, S. C. Park, J. H. Yang, J. Y. Kim, J. H. Seok, U. S. Park, C. W. Choi, S. R. Lee, J. Han, Cryopreservation and its clinical applications, Integrative medicine research 6 (2017) 12–18.

[228] J. G. Baust, D. Gao, J. M. Baust, Cryopreservation: An emerging paradigm change, Organogenesis 5 (2009) 90–96.

[229] G. J. Morris, E. Acton, Controlled ice nucleation in cryopreservation–a review, Cryobiology 66 (2013) 85–92.

[230] R. C. Deller, M. Vatish, D. A. Mitchell, M. I. Gibson, Synthetic polymers enable non-vitreous cellular cryopreservation by reducing ice crystal growth during thawing, Nature communications 5 (2014) 1–7.

[231] P. Kanmani, R. S. Kumar, N. Yuvaraj, K. Paari, V. Pattukumar, V. Arul, Cryopreservation and microencapsulation of a probiotic in alginate-chitosan capsules improves survival in simulated gastrointestinal conditions, Biotechnology and Bioprocess Engineering 16 (2011) 1106–1114.

[232] S. Uman, A. Dhand, J. A. Burdick, Recent advances in shear-thinning and self-healing hydrogels for biomedical applications, Journal of Applied Polymer Science 137 (2020) 48668.

[233] H. Wang, S. C. Heilshorn, Adaptable hydrogel networks with reversible linkages for tissue engineering, Advanced Materials 27 (2015) 3717–3736.

[234] R. Bai, J. Yang, Z. Suo, Fatigue of hydrogels, European Journal of Mechanics-A/Solids 74 (2019) 337–370.

[235] C. De Marco, C. C. Alcântara, S. Kim, F. Briatico, A. Kadioglu, G. de Bernardis, X. Chen, C. Marano, B. J. Nelson, S. Pané, Indirect 3d and 4d printing of soft robotic microstructures, Advanced Materials Technologies 4 (2019) 1900332.

[236] X. Kuang, D. J. Roach, J. Wu, C. M. Hamel, Z. Ding, T. Wang, M. L. Dunn, H. J. Qi, Advances in 4d printing: materials and applications, Advanced Functional Materials 29 (2019) 1805290.

[237] Q. Shi, H. Liu, D. Tang, Y. Li, X. Li, F. Xu, Bioactuators based on stimulus-responsive hydrogels and their emerging biomedical applications, NPG Asia Materials 11 (2019) 1–21.

[238] X. Su, S. Mahalingam, M. Edirisinghe, B. Chen, Highly stretchable and highly resilient polymer–clay nanocomposite hydrogels with low hysteresis, ACS applied materials & interfaces 9 (2017) 22223–22234.

[239] H. Kamata, Y. Akagi, Y. Kayasuga-Kariya, U.-i. Chung, T. Sakai, "nonswellable" hydrogel without mechanical hysteresis, Science 343 (2014) 873–875.

[240] M. A. Skylar-Scott, J. Mueller, C. W. Visser, J. A. Lewis, Voxelated soft matter via multimaterial multinozzle 3d printing, Nature 575 (2019) 330–335.

[241] A. Conev, E. E. Litsa, M. R. Perez, M. Diba, A. G. Mikos, L. E. Kavraki, Machine learning-guided three-dimensional printing of tissue engineering scaffolds, Tissue Engineering Part A (2020).

[242] Z. Zhu, H. S. Park, M. C. McAlpine, 3d printed deformable sensors, Science advances 6 (2020) eaba5575.

[243] Z. Zhu, S.-Z. Guo, T. Hirdler, C. Eide, X. Fan, J. Tolar, M. C. McAlpine, 3d printed functional and biological materials on moving freeform surfaces, Advanced Materials 30 (2018) 1707495.

[244] Y. Wang, R. K. Kankala, K. Zhu, S.-B. Wang, Y. S. Zhang, A.-Z. Chen, Coaxial extrusion of tubular tissue constructs using a gelatin/gelma blend bioink, ACS Biomaterials Science & Engineering 5 (2019) 5514–5524.

[245] N. Ashammakhi, S. Ahadian, F. Zengjie, K. Suthiwanich, F. Lorestani, G. Orive, S. Ostrovidov, A. Khademhosseini, Advances and future perspectives in 4d bioprinting, Biotechnology journal 13 (2018) 1800148.

[246] Y.-C. Li, Y. S. Zhang, A. Akpek, S. R. Shin, A. Khademhosseini, 4d bioprinting: the next-generation technology for biofabrication enabled by stimuli-responsive materials, Biofabrication 9 (2016) 012001.

[247] B. Gao, Q. Yang, X. Zhao, G. Jin, Y. Ma, F. Xu, 4d bioprinting for biomedical applications, Trends in biotechnology 34 (2016) 746–756.

[248] D. J. Roach, C. M. Hamel, C. K. Dunn, M. V. Johnson, X. Kuang, H. J. Qi, The m4 3d printer: A multi-material multi-method additive manufacturing platform for future 3d printed structures, Additive Manufacturing 29 (2019) 100819.

[249] Y. Shanjani, C. Pan, L. Elomaa, Y. Yang, A novel bioprinting method and system for forming hybrid tissue engineering constructs, Biofabrication 7 (2015) 045008.

[250] A. C. Daly, M. D. Davidson, J. A. Burdick, 3d bioprinting of high cell-density heterogeneous tissue models through spheroid fusion within self-healing hydrogels, Nature communications 12 (2021) 1–13.

[251] B. Ayan, D. N. Heo, Z. Zhang, M. Dey, A. Povilianskas, C. Drapaca, I. T. Ozbolat, Aspiration-assisted bioprinting for precise positioning of biologics, Science advances 6 (2020) eaaw5111.